

**Measurement of the Deeply Virtual Neutral Pion  
Electroproduction Cross Section at the Thomas  
Jefferson National Accelerator Facility at 10.6  
GeV**

by

Robert Johnston

Submitted to the Department of Physics  
in partial fulfillment of the requirements for the degree of

Interdisciplinary PhD in Physics and Statistics

at the

MASSACHUSETTS INSTITUTE OF TECHNOLOGY

August 2023

© Massachusetts Institute of Technology 2023. All rights reserved.

Author .....  
.....

Department of Physics  
August, 2023

Certified by .....  
.....

Richard Milner  
Professor of Physics  
Thesis Supervisor

Accepted by .....  
.....

Lindley Winslow  
Associate Department Head of Physics



**Measurement of the Deeply Virtual Neutral Pion  
Electroproduction Cross Section at the Thomas Jefferson  
National Accelerator Facility at 10.6 GeV**

by

Robert Johnston

Submitted to the Department of Physics  
on August, 2023, in partial fulfillment of the  
requirements for the degree of  
Interdisciplinary PhD in Physics and Statistics

**Abstract**

Deeply virtual exclusive reactions provide unique channels to study both transverse and longitudinal properties of the nucleon simultaneously, allowing for a 3D image of nucleon substructure. This presentation will discuss work towards extracting an absolute cross section for one such exclusive process, deeply virtual neutral pion production, using 10.6 GeV electron scattering data off a proton target from the CLAS12 experiment in Jefferson Lab Hall B . This measurement is important as exclusive meson production has unique access to the chiral odd GPDs, and is also a background for other exclusive processes such as DVCS, making the determination of this cross section crucial for other exclusive analyses.

Thesis Supervisor: Richard Milner  
Title: Professor of Physics

## Acknowledgments

To Be Completed.

# Contents

<b>List of Figures</b>	<b>9</b>
<b>List of Tables</b>	<b>12</b>
<b>List of Equations</b>	<b>13</b>
<b>List of To Do Items</b>	<b>14</b>
<b>1 Introduction</b>	<b>15</b>
1.1 Exploring Structure through Scattering . . . . .	17
1.1.1 Scattering at Different Resolution Scales . . . . .	17
1.1.2 Elastic Scattering and Form Factors . . . . .	19
1.1.3 Inelastic Scattering and Parton Distribution Functions . . . . .	23
1.2 Process Background . . . . .	31
1.2.1 Wigner Functions, Generalized Parton Distributions . . . . .	31
1.2.2 Deeply Virtual Exclusive Processes . . . . .	35
1.2.3 Status of DV $\pi^0$ P Measurements . . . . .	39
<b>2 Experiment and Data Processing</b>	<b>45</b>
2.1 Accelerator and Beamline . . . . .	45
2.1.1 Accelerator Facility . . . . .	46

2.1.2	Hall B Beamline . . . . .	49
2.2	CLAS12 Detectors and Run Conditions . . . . .	51
2.2.1	CLAS12 Detector System . . . . .	51
2.2.2	Experiment Run Conditions . . . . .	55
2.3	Reconstruction and Particle Identification . . . . .	55
2.3.1	Decoding and Track Reconstruction . . . . .	59
2.3.2	Particle Identification . . . . .	59
2.3.3	Data Storage and Formatting . . . . .	60
<b>3</b>	<b>Simulations</b>	<b>63</b>
3.1	Computing and Simulation Infrastructure . . . . .	63
3.1.1	MIT Tier 2 and Supercomputing Clusters . . . . .	63
3.1.2	Overview of Simulation Runs . . . . .	63
3.2	Event Generation . . . . .	64
3.2.1	Nonradiative Generator . . . . .	66
3.2.2	Radiative Generator . . . . .	66
3.3	Simulation Pipeline . . . . .	66
3.3.1	Simulation Processing and JLab Computing . . . . .	66
3.3.2	Geant4, GEMC, and CLAS Submissions . . . . .	66
3.4	Simulation Enhancements with Normalizing Flows . . . . .	67
3.4.1	Inverse Transforms and Autoregressive Flows . . . . .	67
3.4.2	Exploration of Simulation Speedup with UNMAF . . . . .	67
<b>4</b>	<b>Cross Section Measurement</b>	<b>69</b>
4.1	General Analysis Overview . . . . .	70
4.1.1	Part 1 . . . . .	70

4.1.2	part 2	70
4.2	Data Pre-Processing	72
4.2.1	Experimental Data Pre-Processing	72
4.2.2	Simulation Data Pre-Processing	72
4.3	Event Selection	73
4.3.1	Exclusivity Cuts	73
4.3.2	Kinematic Fitting	80
4.4	Luminosity	80
4.5	Binning	83
4.6	Correction Factors	83
4.6.1	Acceptance Correction	83
4.6.2	Radiative Corrections	83
4.6.3	Bin Volume Corrections	83
4.6.4	Bin Migration Corrections	84
4.6.5	Overall Normalization Corrections	84
4.7	Uncertainty Estimation	84
4.8	Iterative Bayesian Unfolding	84
<b>5</b>	<b>Results and Further Analysis</b>	<b>85</b>
5.1	Cross Section Results	85
5.2	Structure Function Extraction	88
5.3	Rosenbluth Separation Between Beam Energies	88
5.4	Cross Section with CLAS6 Normalization	88
5.5	Comparison to Theoretical Model	88
5.6	T Dependence and Impact Parameter Extraction	94
5.7	Conclusion	95

A Full Cross Section Data	117
B BSA Cross Check	119
C Derivation of phi math convention	121
D Notes on Kinematic Relationships	123

# List of Figures

1-1	J.J. Thomson's Plum Pudding Model . . . . .	16
1-2	Elastic scattering diagram. . . . .	20
1-3	Tree-level elastic scattering Feynman diagram. . . . .	21
1-4	Fourier Transforms of Charge Distributions . . . . .	23
1-5	Feynman Diagram for Inelastic Scattering. . . . .	24
1-6	Scattering Cross Section vs. Energy Transfer . . . . .	25
1-7	Proton Structure Function $F_2^p$ . . . . .	28
1-8	Parton Distribution Functions . . . . .	29
1-9	Scattering Measurements at Different Scales . . . . .	30
1-10	Distribution Relationship Cube . . . . .	34
1-11	DVCS and DVMP Feynman Diagrams . . . . .	35
1-12	Proton Pressure Distribution, Experiment . . . . .	36
1-13	Proton Pressure Distribution, Theory . . . . .	36
1-14	DVPiP Feynman Diagram . . . . .	37
1-15	Diagram of Lepton-Hadron Plane Angle $\phi$ . . . . .	38
1-16	Kinematic Reach Comparison . . . . .	41
1-17	Analysis Flowchart . . . . .	44
2-1	Aerial View of JLab . . . . .	46
2-2	JLab Accelerator Schematic . . . . .	47

2-3	CEBAF Beamline . . . . .	48
2-4	Hall B Beamline . . . . .	50
2-5	CLAS12 Layout . . . . .	52
2-6	Forward Detector Packages . . . . .	53
2-7	Central Detector Packages . . . . .	54
2-8	Your caption goes here . . . . .	58
2-9	Caption from (Battaglieri, 2021) . . . . .	59
2-10	The distribution for mass of two photons $M_{\gamma\gamma}$ . . . . .	61
2-11	The distribution for mass of two photons after exclusivity cuts . . . . .	61
4-1	High-level data processing flow . . . . .	71
4-2	Comparison of experiment (blue) and simulation (red) missing mass, energy, momentum, and invariant gamma-gamma mass distributions, before any smearing factors were added to the simulation data. . . . .	72
4-3	Comparison of experiment (blue) and simulation (red) missing mass, energy, momentum, and invariant gamma-gamma mass distributions, with smearing factors added to the simulation data proton and photon momenta. . . . .	73
4-4	$MM^2$ (epX) vs $\theta_X\pi$ 2D distribution. . . . .	74
4-5	Exclusive distributions for events with at least one electron, proton and two photons. . . . .	74
4-6	Exclusive distributions for events with at least one electron, proton and two photons. . . . .	75
4-7	Exclusive distributions for events with at least one electron, proton and two photons. . . . .	75

4-8	Exclusive distributions after tight $M_{\gamma\gamma}$ mass and transverse missing momenta cuts . . . . .	76
4-9	$MM^2(epX)$ distributions for multiple $\theta_{X\pi}$ cut values. . . . .	77
4-10	The numbers of signal (red markers) and background (black markers) events as functions of $\theta_{X\pi}$ cut value for multiple $Q^2$ bins. . . . .	78
4-11	The numbers of signal (red markers) and background (black markers) events as functions of $\theta_{X\pi}$ cut value for multiple $x_B$ bins. . . . .	78
4-12	Exclusive distributions after all exclusivity cuts . . . . .	79
5-1	Comparison of CLAS12 (blue) and CLAS6 (red) reduced cross sections, using Fall 2018 outbending dataset. Error bars are statistical only. . . . .	87
5-2	CLAS12 and CLAS6 t dependence of cross sections. The fits are exponential functions $Ae^{-bt}$ , where the slope parameter b are in close agreement for the bins considered. The overall normalization A is not yet determined for the CLAS12 dataset, so a small overall offset from the CLAS6 data is expected. Errors are only statistical. . . . .	95
5-3	Kinematic regions of Deep Inelastic Scattering and the comparative reach of EIC and CEBAF, from (Arrington et al., 2022) . . . . .	96
B-1	BSA Cross Check Results . . . . .	120
D-1	Caption . . . . .	124

# List of Tables

1.1	GPDs Across Nucleon and Quark Polarizations . . . . .	33
2.1	Beam properties . . . . .	49
2.2	Data rates of various physics experiments . . . . .	51
4.1	Terms of Luminosity Equation . . . . .	82

# List of Equations

1.1	Diffraction Limit . . . . .	18
1.2	de Broglie Relationship . . . . .	18
1.3	Rutherford Scattering Differential Cross Section . . . . .	20
1.4	Mott Scattering Differential Cross Section . . . . .	21
1.5	Elastic Scattering Differential Cross Section . . . . .	22
1.8	Rosenbluth Scattering Cross Section . . . . .	23
1.9	Outgoing Hadronic System Invariant Mass $W$ . . . . .	24
1.10	Bjorken $X$ . . . . .	25
1.11	Inelasticity $y$ . . . . .	26
1.12	Energy Transfer $\nu$ . . . . .	26
1.13	Lorentz-invariant Rosenbluth Scattering Cross Section . . . . .	26
1.14	Scattering Cross Section in Terms of $F_1(x_B, Q^2)$ and $F_2(x_B, Q^2)$ . . . . .	26
1.15	$F_2$ structure function in terms of PDFs . . . . .	27
1.16	Wigner Quasi-probability Distributions . . . . .	32
1.17	Wigner Operator . . . . .	32
1.18	Reduced Wigner Distribution . . . . .	32
1.21	$DV\pi^0P$ Cross Section Decomposition . . . . .	37
1.22	Virtual Photon Flux . . . . .	38
1.30	$DV\pi P$ Experimental Cross Section . . . . .	43

# List of To Do Items

1.2	FROM RICHARD: DEFINE CROSS SECTION AND ELASTIC SCATTERING A BIT MORE HERE . . . . .	19
1.14	input standard model, pion information . . . . .	26
1.15	include references to all the experiments at different energy scales plot	29
1.15	include note about HofstaderM. Gockeler et al., Phys.Rev.Lett. 98, 222001 (2007). . . . .	29
1.15	Great rutherford scattering diagram - Simon Fraser University Introduction to Nuclear Science Rutherford Scattering NUCS 342 March 16 2011	29
1.18	possibly work in TPEX by discussion of OPE formalism . . . . .	32
1.18	if possible work in Operator Product and Twist expansion . . . . .	32
1.27	statement introducing idea of posing this as an inverse problem, introduce the experimental interpretation of the cross section . . . . .	42
2.0	GET FT CITATION . . . . .	54
2.0	FIGURE OUT FMT vs BMT vs MVT . . . . .	55

# Chapter 1

## Introduction

Humans have tried to understand the nature of the world around us for millennia, with discerning the structure of matter being a central effort in this quest. Famously, the Greek philosophers Leucippus and Democritus (~5th century BCE) are credited with the concept of “atomism” - the belief that matter is composed of tiny indivisible particles called atoms (from the Greek *ατομοσ*, roughly translating to “uncuttable” ([C.C.W. Taylor, 1999](#)). Even further back, there are Indian records from as early as the 8th century BCE conceptualizing the world as being built from tiny fundamental particles ([Thomas McEvilley, 2002](#)).

Scientific progress on this front stalled until the early 1800s, when chemists explored how different elements combined in to form compounds in specific, repeatable, small integer ratios. John Dalton formulated this idea as the Law of Multiple Proportions, which paved the way for early scientific atomic theory ([Britannica, 2010](#)). In 1897, J.J. Thomson discovered the first subatomic particle, the electron, by studying cathode rays ([J. Thomson, 1901](#)). Accordingly, he devised a model of the atom which had electrons embedded in a ball of positively charged material, called the

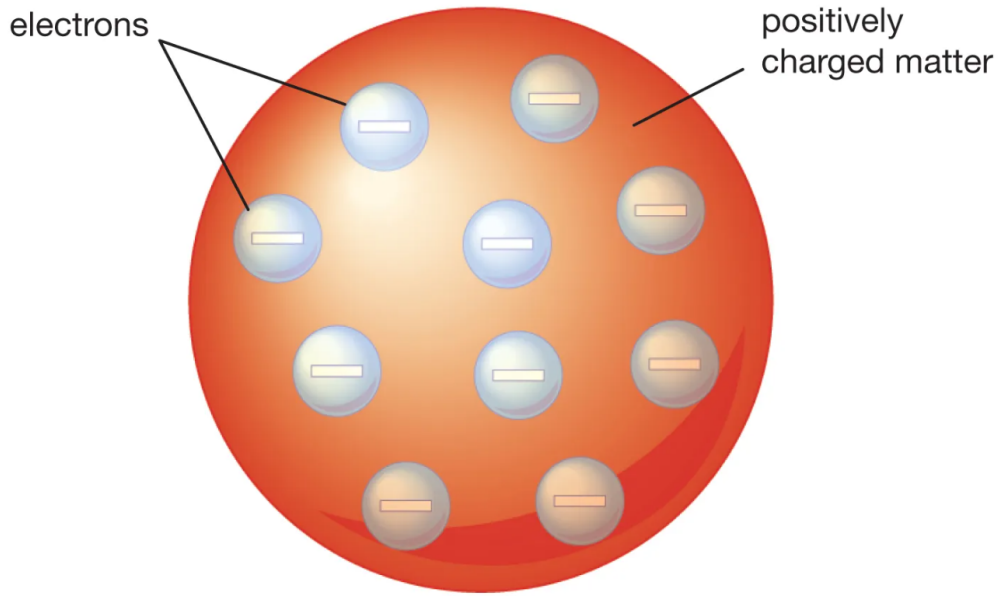


Figure 1-1: J.J. Thomson's Plum Pudding Model of the atom ([Britannica, 2023](#))

Thomson, or Plum Pudding, Model([Jaume Navarro, 1995](#)).

With the idea that the atom was a composite object, scientists began experimentation to study its exact structure. This was the start of what has been the 120 years of particle scattering studies to probe first atomic, then nuclear structure.

The rest of this chapter details the findings of previous scattering experiments and provides a background on Generalized Parton Distributions and Deeply Virtual Exclusive Processes, the topic of this work. Chapter 2 describes the experimental configuration of the CLAS12 detector and data taking conditions. Chapter 3 discusses data analysis procedures to reconstruct particles and classify events from detector level information. Simulations and computational pipelines for this work are presented in chapter 4. The analysis procedure for combining experimental and simulated data into a differential cross section with correction factors is discussed

in chapter 5. Chapter 6 displays and discusses results and uncertainties. Chapter 7 summarizes this work and lays a path for finalizing the measurement. The appendices include numerous technical details and supplemental plots.

## 1.1 Exploring Structure through Scattering

The typical length scales for atoms and nucleons are 0.1 nm which is far smaller than the wavelength of human-visible light ( $\sim 500$  nm). As such, atomic and nuclear structure must be explored by forcing some interaction and then inferring the structure from the observed results. Thomson's atomic model was famously tested in the early 1900s by Ernest Rutherford's research group, wherein  $\alpha$  particles were fired at thin metal targets, and the scattering behaviour was observed ([Geiger and Marsden, 1909](#)) ([Rutherford, 1911](#)).

The results were not consistent with Thomson's model, but instead indicated that there was a very small, dense, positively charged nucleus at the center of every atom. Further experiments by Rutherford would lead to the discovery of the proton around 1920 ([Rutherford, 1919](#)). Puzzles about the nucleus remained, including a consistent description of isotopes, until 12 years later when James Chadwick suggested the existence of the neutron ([Chadwick, 1932](#)). With electrons and the two nucleons discovered, it seemed as though the indivisible constituents of the atom were finally realized, but future experiments showed a much more complex, sub-nuclear structure.

### 1.1.1 Scattering at Different Resolution Scales

The diffraction limit for microscopic (compared to telescopic) systems can be approximated by equation 1.1, where  $n$  is the index of refraction,  $\theta$  is a measure of the

device aperture,  $\lambda$  is the wavelength of the probe, and  $d$  is the minimum resolvable length scale. Thus, the wavelength of a probe sets a fundamental lower limit on the achievable resolution of a microscopic imaging system - roughly, at small enough distances, the probe's waves interfere, prohibiting resolution at or below that scale.

$$d = \frac{\lambda}{2n \sin \theta}. \quad (1.1)$$

For visible light microscope systems,  $\lambda \sim 500$  nm, and so the minimum resolvable feature size is approximately  $d \sim 250$  nm. Techniques exist to extend the resolution size by approximately an order of magnitude, e.g. expansion microscopy ([Chen, Tillberg, and Boyden, 2015](#)) or Near-Field Scanning Optical Microscopy ([Ma et al., 2021](#)), but non-visible-light probes are needed for scales below  $\sim 10$  nm.

In particular, the de Broglie relationship [1.2](#) ([Broglie, 1924](#)) states that the wavelength  $\lambda$  of a particle is inversely proportional to its momentum  $p$ , with  $h$  being Planck's constant.

$$\lambda = \frac{h}{p}. \quad (1.2)$$

With this relationship, we can see that by increasing a particle's momentum, its effective wavelength is reduced. This is the fundamental principle which allows electron microscopes to image matter at a resolution of  $\sim 10\text{-}0.1$  nm ([Franken et al., 2020](#)), corresponding to electron momenta of  $\sim 1\text{-}100$  keV. At this scale, viruses, cells, molecular structures, and even atoms can be imaged ([Williams and Carter, 2009](#)), with striking results commonly published online. Other probes could be used to circumvent the diffraction limit, such as high energy (low-wavelength) photons or

high momentum (low de Broglie wavelength) protons or neutrons, but electrons are an ideal candidate in this regime as they are easy to produce, steer, interact with the target, and detect.

To move beyond imaging at the atomic scale ( $\sim 1 \text{ \AA}$ ) to the nuclear scale ( $\sim 1 \text{ fm}$ ) requires probes that are 100,000 times more powerful. Electrons are still an ideal probe due to their (apparent) lack of internal structure, but rather than a room sized microscope, an entire accelerator facility is needed to achieve high enough energies and luminosities for sub-nuclear scale resolution.

### 1.1.2 Elastic Scattering and Form Factors

At these scales, it becomes useful to introduce the notion of cross sections. [FROM RICHARD: DEFINE CROSS SECTION AND ELASTIC SCATTERING A BIT MORE HERE](#)

. Cross section definition, from britannica: cross section, in nuclear or subatomic particle physics, is the probability that a given atomic nucleus or subatomic particle will exhibit a specific reaction (for example, absorption, scattering, or fission) in relation to a particular species of incident particle. Cross section is expressed in terms of area, and its numerical value is chosen so that, if the bombarding particle hits a circular area of this size perpendicular to its path and centered at the target nucleus or particle, the given reaction occurs, and, if it misses the area, the reaction does not occur. The reaction cross section is usually not the same as the geometric cross-sectional area of the target nucleus or particle. The unit of reaction cross section is the barn, equal to  $10^{-24} \text{ square cm}$ .

Imaging with electrons (or other non-visible-light probes) at any energy scale is commonly understood in terms of scattering cross sections,  $\sigma$ , with dimensions of

area and interpreted as the probability for a certain interaction to occur. Typical elastic scattering cross sections for transitions metals with 100 keV incident electrons as in electron microscopy are  $\sim 10^{-22} m^2$  (Williams and Carter, 2009). In contrast, the cross sections to be discussed in this thesis are on the order of tens of nanobarn ( $10^{-36} m^2$ ), or 14 orders of magnitude smaller.

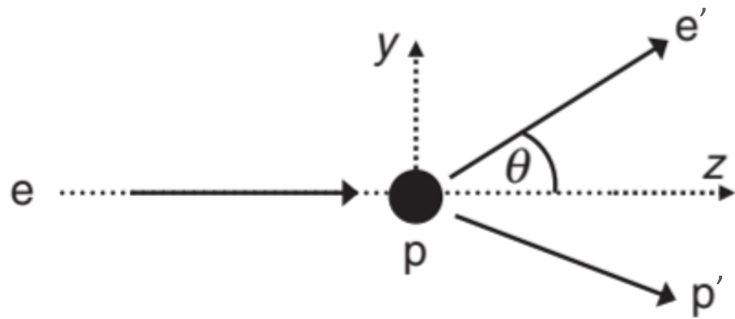


Figure 1-2: Elastic scattering diagram.

The scattering cross section for a probe (such as an electron) incident on a target, can be calculated at lowest order by considering a fixed (no recoil), point-like (no structure), radially symmetric Coulomb potential (e.g., a proton) with a non-relativistic incident charged particle. The resulting equation was used by Rutherford's group in the discovery of the nucleus, and for an electron beam of energy  $E_{beam}$  is given by (1.3), where  $\alpha$  is the fine structure constant.

$$\frac{\theta}{2} \left( \frac{d\sigma}{d\Omega} \right)_{Ruth} = \frac{\alpha^2}{16E_{beam}^2 \sin^4(\theta/2)}. \quad (1.3)$$

To probe smaller resolution scales, it is necessary to increase the energy of the beam, and eventually the probe must be treated relativistically. This correction term is provided by the Mott scattering cross section, given by (1.4), which still assumes

a fixed, point-like target, with only Coulomb interactions.

$$\left(\frac{d\sigma}{d\Omega}\right)_{Mott} = \frac{\alpha^2}{4E^2 \sin^4(\theta/2)} \cos^2 \frac{\theta}{2} = \left(\frac{\alpha}{2E \sin^2(\theta/2)} \cos \frac{\theta}{2}\right)^2 = 4 \cos^2 \frac{\theta}{2} \left(\frac{d\sigma}{d\Omega}\right)_{Ruth}. \quad (1.4)$$

At higher incident electron energies (and thus finer spatial resolutions), the proton's finite size must be accounted for, as well as the momentum transferred to it. The tree-level Feynman diagram for elastic electron-proton scattering is shown in Fig. 1-3. The incoming electron  $e$  exchanges a virtual photon with the proton  $p$ , resulting in a momentum transfer of  $q = p_{e'} - p_e$ .

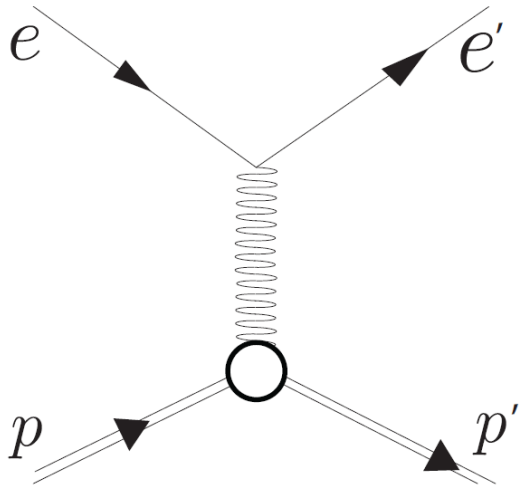


Figure 1-3: Tree-level elastic scattering Feynman diagram.

The momentum transfer  $q$  sets the resolution scale for these processes, but it is convenient to work with the negative square of this value, defined as  $Q^2 = -q^2$ . With this term, we can express the relativistic differential cross section for the scattering

of electrons off a resting, point-like proton as in (1.5), where  $m_p$  is the mass of the proton.

$$\frac{d\sigma}{d\Omega} = \frac{\alpha^2}{4E_{beam}^2 \sin^4(\theta/2)} \frac{E_{e'}}{E_{beam}} \left( \cos^2 \frac{\theta}{2} + \frac{Q^2}{2m_p^2} \sin^2 \frac{\theta}{2} \right). \quad (1.5)$$

Compared with Mott Scattering, there are two differences in this formula: The  $\frac{E_{e'}}{E_{beam}}$  term in the scattering cross section comes from the electron losing energy to the proton's final state kinetic energy (no longer fixed), and the term proportional to  $\sin^2(\theta/2)$  is due to a purely magnetic spin-spin interaction.

If the proton were a point, then (1.5) would agree with experiment for all electron scattering energies. Instead, deviations are observed as we increase the beam energy. To account for this structure, we need to include two form factors,  $G_E(Q^2)$  - related to the distribution of charge, and  $G_M(Q^2)$ , related to the distribution of magnetism inside the proton. In the low- $Q^2$  limit, these form factors are the Fourier transforms of the charge and magnetic moment distributions as in (1.6) and 1.7, reducing to the charge and the magnetic moment of the proton in the  $Q^2 = 0$  limit.

$$G_E(Q^2) \approx G_E(q^2) = \int e^{iq \cdot r} \rho(r) d^3r; \quad G_E(0) = \int \rho(r) d^3r = 1. \quad (1.6)$$

$$G_M(Q^2) \approx G_E(q^2) = \int e^{iq \cdot r} \mu(r) d^3r; \quad G_M(0) = \int \mu(r) d^3r = 2.79. \quad (1.7)$$

Including these form factors in our cross section gives us the full elastic scattering cross section, as shown in (1.8).

$$\frac{d\sigma}{d\Omega} = \frac{\alpha^2}{4E_1^2 \sin^4(\theta/2)} E_1 \left( \frac{G_E^2 + \tau G_M^2}{1 + \tau} \cos^2 \frac{\theta}{2} + 2\tau G_M^2 \frac{Q^2}{2m_p^2} \sin^2(\frac{\theta}{2}) \right), \quad (1.8)$$

where  $\tau = \frac{Q^2}{4m_p^2}$ .

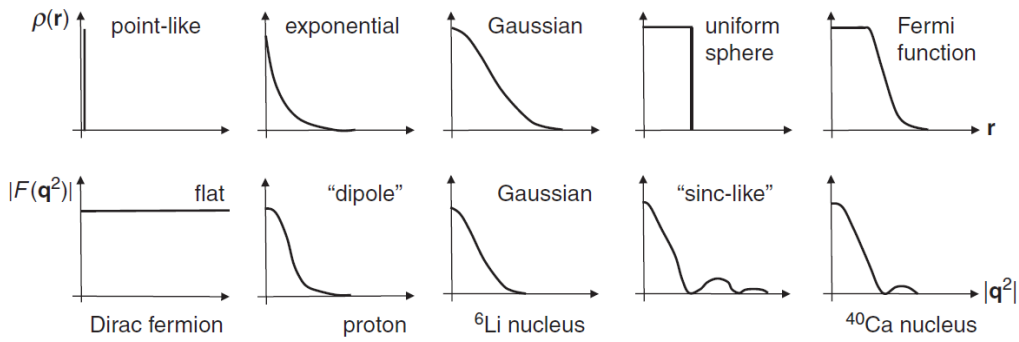


Figure 1-4: Samples of charge distributions and their corresponding form factors  $F(\mathbf{q}^2)$ , from ([M. Thomson, 2013](#)).

By the 1960s, elastic scattering had been studied sufficiently well as to measure the proton form factors up to several  $\text{GeV}^2/\text{c}^2$  in  $Q^2$ . The observed results were consistent with a proton having a ‘dipole’ form factor, as shown in Fig. 1-4. Investigating proton structure at finer spatial resolutions requires increasing the beam energy, but eventually the the elastic scattering cross section becomes negligible and instead the interactions are sufficiently energetic so as to create additional particles.

### 1.1.3 Inelastic Scattering and Parton Distribution Functions

Elastic scattering can be defined as interactions where the target stays intact; specifically, the variable  $W$  is the invariant mass of the outgoing struck target (1.9), where

elastic scattering satisfies the condition  $W^2 = m_p^2$ . If  $W^2 > m_p^2$ , we instead have inelastic scattering, written as  $e p \rightarrow e' X$ , where  $X$  stands for some outgoing hadronic system, as shown in the Feynman diagram in Fig. 1-5.

$$W^2 \equiv (p_p + q)^2 = (p_p + (p_e - p_{e'}))^2. \quad (1.9)$$

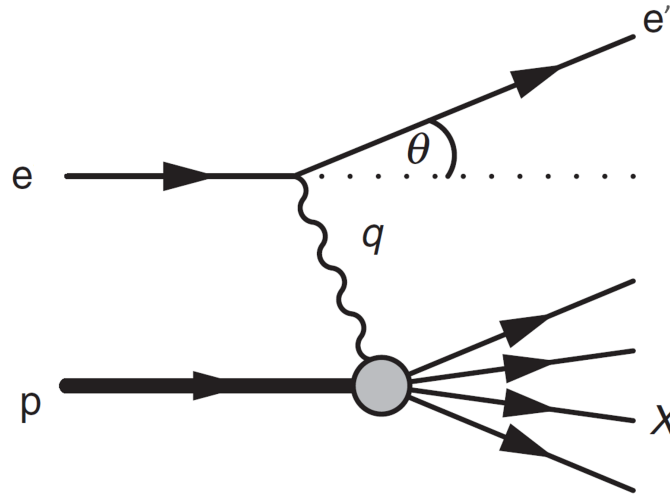


Figure 1-5: Feynman Diagram for Inelastic Scattering.

The cross section for inelastic scattering has several peaks at various proton resonances, as indicated in the upper sketch of Fig. 1-6. Continuing to higher energy transfers we reach the ‘Deep Inelastic Scattering’ (DIS) regime, defined by kinematics as  $Q^2 > 1 \text{ GeV}^2$  and  $W^2 > 4 \text{ GeV}^2$ . Note that in the DIS process, the proton is smashed apart, yielding many subparticles. Other high-energy inelastic processes where the proton is left intact will be discussed in section 1.2.1.

Since we remove the constraint that the mass of the final state is the proton mass, we now have one extra degree of freedom, i.e., we need at least 2 variables to describe

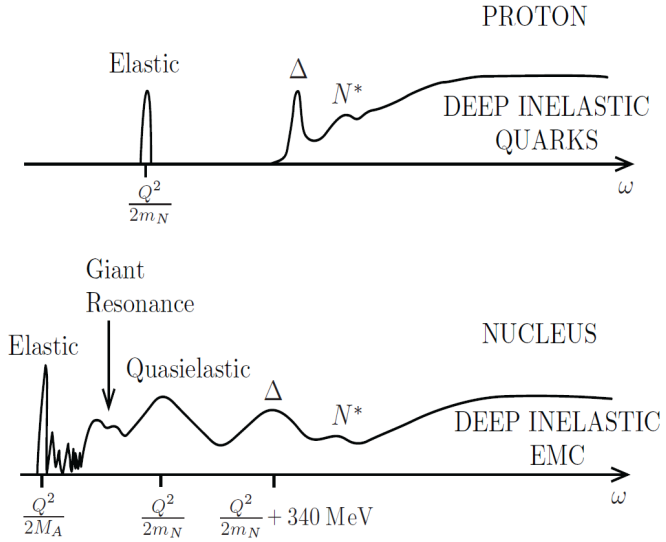


Figure 1-6: Schematic plot of cross section as a function of electron energy transfer for inclusive electron scattering off a proton (top) and a nucleus (bottom), from ([T. W. Donnelly et al., 2017](#)).

scattering here. Convenient choices and the squared four-momentum transfer of the virtual photon  $Q^2$  and Bjorken X  $x_B$ , defined in (1.10).  $x_B$  is a measure of elasticity:  $x_B = 1$  for elastic scattering. It is useful in that it can also be interpreted as the fraction of proton momentum carried by the struck quark in the infinite momentum frame.

$$x_B \equiv \frac{Q^2}{2p_p \cdot q} = \frac{Q^2}{Q^2 + W^2 - m_p^2}. \quad (1.10)$$

Another useful quantity is  $y$ , which is a measure of the inelasticity of the scattering. It is the fractional energy lost by the electron in the scattering process, where  $y=0$  is for perfectly elastic collisions, and is given by (1.11)

$$y \equiv \frac{p_p \cdot q}{p_p \cdot p_e} = \frac{\nu}{E_{beam}} = 1 - \frac{E_{e'}}{E_{beam}}, \quad (1.11)$$

where  $\nu$  is the energy transferred in the collision (1.12).

$$\nu = \frac{Q^2}{2 * x_B * m_p}. \quad (1.12)$$

With these definitions, we can write the differential cross section for inelastic scattering. Note that the general formula for the differential cross section for elastic scattering, (1.8) can be re-written in explicitly Lorentz-invariant form as in (1.13).

$$\frac{d\sigma}{d\Omega} = \frac{4\pi\alpha^2}{Q^4} \left[ \left(1 - y - \frac{m_p^2 y^2}{Q^2}\right) \frac{G_E^2 + \tau G_M^2}{1 + \tau} + y^2 \frac{G_M^2}{2} \right]. \quad (1.13)$$

This equation can be generalized to include inelastic scattering by replacing the terms corresponding to the combinations of form factors  $G_E$  and  $G_M$  with structure functions  $F_1(x_B, Q^2)$  and  $F_2(x_B, Q^2)$ , which describe proton structure as a function of both independent variables. This results in the differential cross section given by (1.14) .

$$\frac{d\sigma}{d\Omega} = \frac{4\pi\alpha^2}{Q^4} \left[ \left(1 - y - \frac{m_p^2 y^2}{Q^2}\right) \frac{F_2(x_B, Q^2)}{x_B} + y^2 F_1(x_B, Q^2) \right]. \quad (1.14)$$

### input standard model, pion information

Experiments in the 1960s on DIS indicated that the structure functions  $F_1(x_B, Q^2)$  and  $F_2(x_B, Q^2)$  were nearly independent of  $Q^2$ , a feature known as Bjorken scaling

(Bjorken and Paschos, 1969). This indicated scattering was occurring off of point-like constituents - current experiment results provide a constraint on the maximum radius of these constituent to be at most  $10^{-18}$  m (M. Thomson, 2013).

Secondly, DIS results indicated that the two structure functions could be expressed as  $F_2(x_B) = 2 * x_B * F_1(x_B)$ , named the Callan-Gross relation. This relationship can be explained if the electron is scattering off of spin-half point-like particles inside the proton, which combined with Bjorken scaling provides strong evidence for the existence of quarks inside the proton, and motivated the development of the parton model (Feynman, 1969).

The parton model connects the experimentally measurable structure functions to Parton Distribution Functions (PDFs) which describe the distribution of proton longitudinal momentum amongst its constituents. Specifically, a PDF  $q_i(x_B)$  describes the probability density of finding a parton carrying a longitudinal momentum fraction in the interval  $(x_B, x_B + dx_B)$ . The relationship between PDFs and structure functions is given by (1.15), where  $Q_i$  is the charge of each quark.

$$F_2^p(x_B) = x_B \sum_i Q_i^2 q_i(x_B). \quad (1.15)$$

Structure functions have been studied in great detail over a very large kinematic range across  $Q^2$  and  $x_B$ , the results of which are shown in Fig. 1-7.

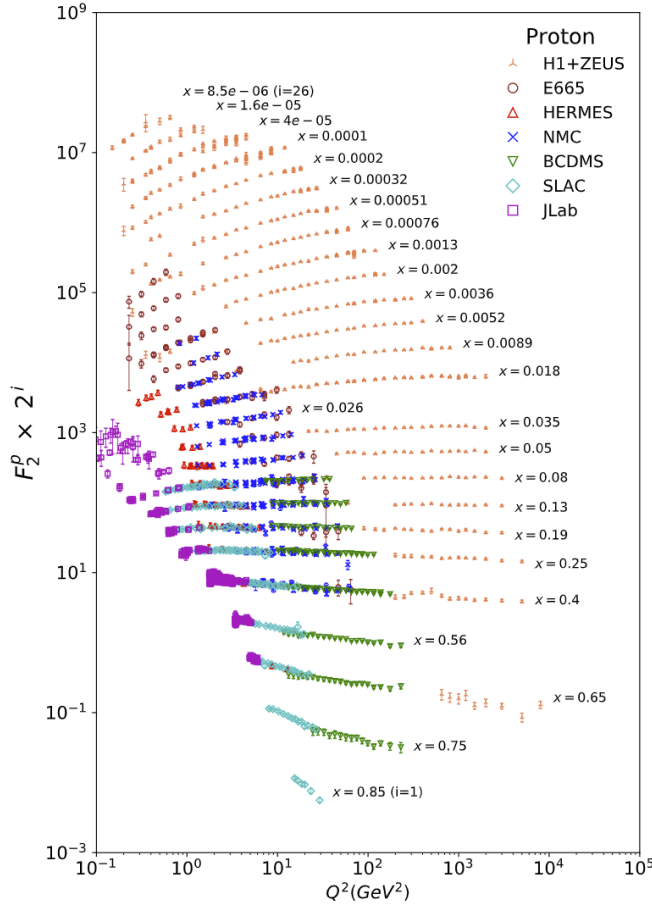


Figure 1-7: The proton structure function  $F_2^p$ , measured at various experiments as listed, all with  $W^2 > 3.5\text{GeV}^2$ .  $F_2^p$  values have been multiplied by  $2^{ix}$  for visual purposes, from ([Zyla et al., 2020](#)).

The global experimental results can be combined with theoretical QCD frameworks such as the DGLAP evolution equations ([Altarelli and Parisi, 1977](#)). to plot PDFs for various constituents of the proton, as shown in Fig. 1-8.

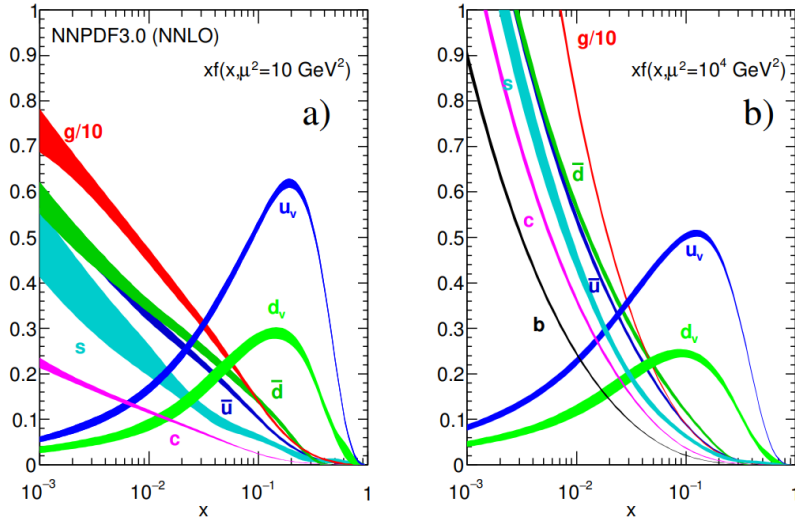


Figure 1-8: Quark and gluon distribution functions from NNLO NNPDF3.0 global analysis at  $\mu^2 = 10 \text{ GeV}^2$  (left) and  $\mu^2 = 10^4 \text{ GeV}^2$  (right), from (Zyla et al., 2020).

All of these major scattering scales explored through the 20<sup>th</sup> century are summarized in Fig. 1-9, spanning roughly four orders of magnitude in length scale. While steady increases in resolving power have been made, the focus of this work (red triangle in figure) is not to image even finer scale parton dynamics, but rather to understand the multidimensional structure of the nucleon. In particular, while PDFs allow for a 1 dimensional mapping of the inner workings of a proton, even more information can be gleaned from more complex scattering reactions. Efforts are now directed towards so called *proton tomography* - 3D imaging of nucleon structure - which is the focus of this analysis.

include references to all the experiments at different energy scales plot

include note about HofstaderM. Gockeler et al., Phys.Rev.Lett. 98, 222001

(2007).

Great rutherford scattering diagram - Simon Fraser University Introduction to Nuclear Science Rutherford Scattering NUCS 342 March 16 2011

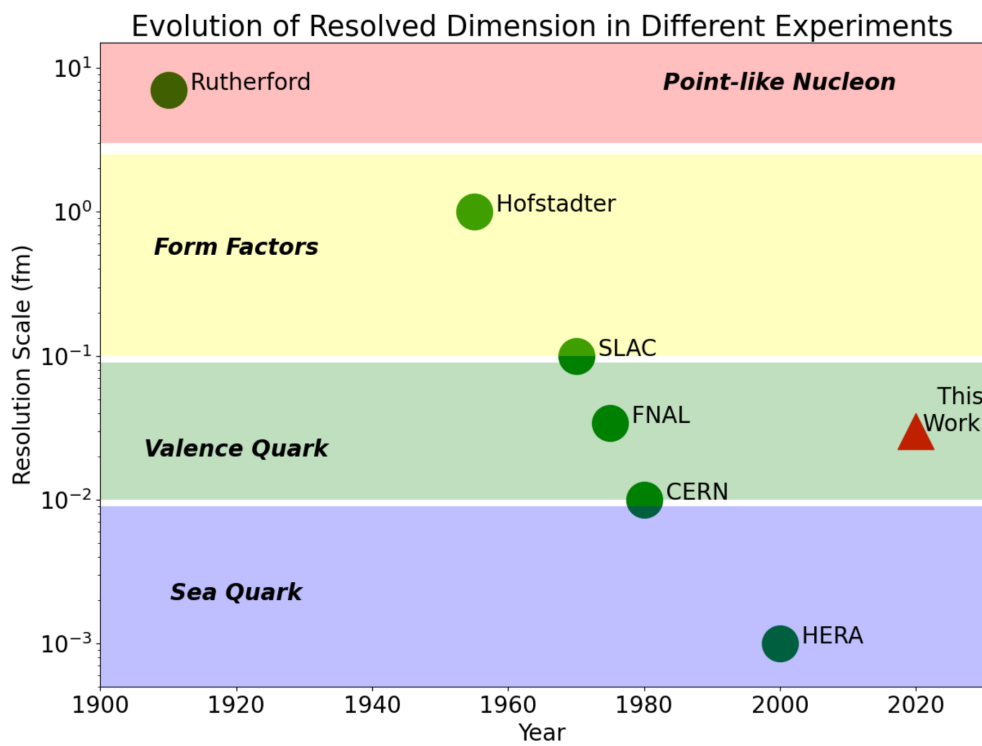


Figure 1-9: Scattering experiments performed at different energy scales reveal different information about proton structure. This work (red triangle) focuses on multi-dimensional structure mapping in the valence quark regime. Figure modified from ([Klein, 2005](#)).

## 1.2 Process Background

The term *tomography* is derived from the Greek word *tomos*, which translates to *slice* or *section*. In the medical field, CT scans (computed tomography) combine many 2-D images from X-ray scans to generate a three-dimensional reconstruction of bodily organs. Building on this, proton tomography harnesses many nuclear reactions to reconstruct multi-dimensional mappings of partons' spatial and momentum distributions inside nucleons.

### 1.2.1 Wigner Functions, Generalized Parton Distributions

In classical mechanics, a particle can be completely described by its position in its six-dimensional phase space (three spatial and three momentum coordinates). An ensemble of such particles can be most completely understood through its phase space distribution function, which contains the probability of finding a particle in a particular region in phase space. In quantum systems, a pure phase space distribution is not well defined because of Heisenberg's uncertainty principle. However, in 1932 Eugene Wigner introduced a formalism that addressed this ([Wigner, 1932](#)), yielding functions that provide the most comprehensive representation achievable for quantum systems.

#### Wigner Quasi-probability Distributions

Wigner Quasi-probability Distributions, commonly referred to as simply Wigner functions or Wigner distributions, are defined as in [\(1.16\)](#). This can be integrated over  $x$  ( $p$ ) to yield momentum (space) density, but for arbitrary  $(x,p)$  the distribution can take negative values, and so violates probability axioms and thus is a quasi-probability distribution rather than a full probability distribution. Wigner

distributions are useful outside of particle physics, notably in signal processing, with more details available in (Hillery et al., 1984).

$$W(x, p) = \frac{1}{\pi\hbar} \int_{-\infty}^{\infty} \psi^*(x + \eta)\psi(x - \eta)e^{2ip\eta/\hbar} d\eta. \quad (1.16)$$

The corresponding generalization to relativistic quark and gluon phase space distributions is covered in (Ji, 2004) to yield a Wigner Operator (1.17) which can be used to obtain the reduced quantum phase-space quark distributions in the nucleon (1.18).

$$\hat{W}_{\Gamma}(\vec{r}, k) = \int_{-\infty}^{\infty} e^{ik\cdot\eta} \bar{\Psi}(\vec{r} - \eta/2) \Gamma \Psi(\vec{r} - \eta/2) d^4\eta \quad (1.17)$$

$$W_{\Gamma}(\vec{r}, \vec{k}) = \int \frac{dk^-}{4\pi^2} \frac{1}{2} \int \frac{d^3\vec{q}}{8\pi^3} e^{-i\vec{q}\cdot\vec{r}} \langle \vec{q}/2 | \hat{W}_{\Gamma}(\vec{r}, k) | -\vec{q}/2 \rangle. \quad (1.18)$$

Here we have integrated over  $k^- = (k^0 - k^z)/\sqrt{2}$ , the light-cone energy, since it is difficult to measure in high-energy processes.

## Generalized Parton Distributions

possibly work in TPEX by discussion of OPE formalism

if possible work in Operator Product and Twist expansion

No known experiments currently exist that are able to directly measure this distribution (nor is it known if it is possible). Fortunately, in recent decades theorists have been able to link experimental observables to further reduced forms of (1.18).

Specifically, integration can be performed over spatial coordinates to yield Transverse Momentum Distributions (TMDs) which are outside the scope of this work. Alternatively, integration can be performed over momentum coordinates to yield Generalized Parton Distributions (GPDs), which encode transverse spatial as well as longitudinal momentum distributions of partons inside the nucleon. As shown in ([Ji, 2004](#)), at leading-twist (twist-2), iterating through all choices of the Dirac matrix for quark distributions  $\Gamma$  yields 8 distinct GPDs. They are generally expressed in terms of parton momentum fraction  $x$ , skewness  $\xi = \frac{-q^2}{q \cdot P} \sim \frac{x_B}{2-x_B}$ , and momentum transfer  $t$ .

4 correspond to helicity conserving (chiral even) processes and 4 correspond to helicity flipping (chiral odd) processes:  $H$ ,  $E$ ,  $\tilde{H}$ , and  $\tilde{E}$  for chiral even, and  $H_T$ ,  $E_T$ ,  $\tilde{H}_T$ , and  $\tilde{E}_T$  ( $\tilde{E}_T = 2^* \tilde{H}_T + E_T$  is commonly used). Table 1.1 summarizes the GPDs with respect to polarization states.

Nucleon		Quark Polarization		
Polarization		U	L	T
U	$H$	*	$\tilde{E}_T = 2^* \tilde{H}_T + E_T$	
L	*	$\tilde{H}$		$\tilde{E}_T$
T	$E$	$\tilde{E}$		$H_T, \tilde{H}_T$

Table 1.1: GPDs Across Nucleon and Quark Polarizations. \* forbidden by parity.

GPDs can be understood by considering further integrations and forward limits - in the same way that the nucleon charge must be recovered when integrating over PDFs or Form Factors, these functions themselves are recovered when appropriately integrating over GPDs, as in Fig. 1-10. Specifically, first moments of the GPDs  $H$  and  $E$  are related to the Dirac and Pauli form factors  $F_1$  and  $F_2$  respectively:

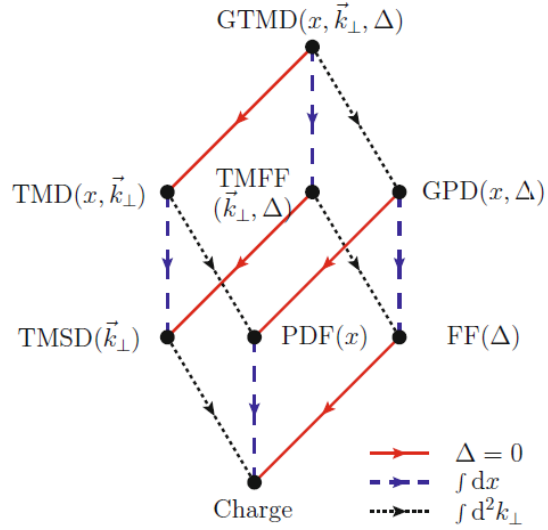


Figure 1-10: Relation cube, from ([M. Burkardt and Pasquini, 2016](#)).

$$\int dx H(x, \xi, t) = F_1(t) \quad (1.19)$$

$$\int dx E(x, \xi, t) = F_2(t). \quad (1.20)$$

GPDs have been shown ([Ji, 1997](#)) to encode spin distributions and also can be interpreted as describing the transverse spatial distribution of quarks ([Matthias Burkardt, 2007](#)). Further, GPDs relation to energy-momentum tensor form factors (EMTs) allows access to EMT densities, which describe the distribution of energy, momentum, and pressure inside the nucleon. It was originally not known how to measure GPDs, but later were found to be experimentally accessible through deeply virtual exclusive processes (DVEP) relying on factorization theorems ([Collins and Freund, 1999](#)), ([Bauer et al., 2002](#)).

### 1.2.2 Deeply Virtual Exclusive Processes

Deeply virtual exclusive processes are interactions occurring with high photon virtuality ( $Q^2 \gg m_p^2$ ) in the DIS regime ( $W^2 \gg m_p^2$ ), with thresholds normally set to require  $Q^2 > 1 \text{ GeV}^2$  and  $W > 2 \text{ GeV}$ . The processes involve the scattering of a virtual photon off a nucleon target, yielding either a real photon or mesons, along with an intact final state nucleon and incident particle (e.g. from an electron or muon beam). These processes are in stark contrast to DIS, where the nucleon target is shattered into many pieces, and can instead be thought of as a hard yet precise non-invasive process. Different reactions have been shown to have different GPD dependencies, and thus provide different windows into sub-nucleon mechanics.

#### Deeply Virtual Compton Scattering and Meson Production

Fig. 1-11 illustrates diagrams for Deeply Virtual Compton Scattering (DVCS) and Deeply Virtual Meson Production (DVMP).

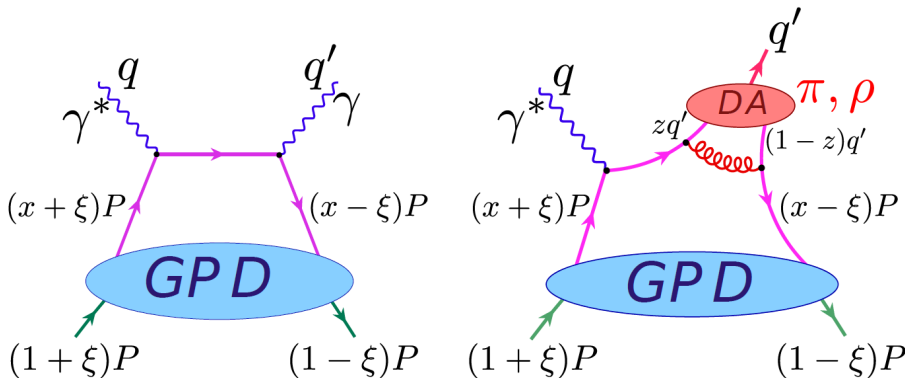


Figure 1-11: Feynman diagrams for DVCS (left) and DVMP (right), from (Kubarovsky, 2011). DA refers to the appropriate meson distribution amplitude.

DVCS is widely regarded as the “cleanest” channel and has already been lever-

aged to provide great insights into the structure of the nucleon. For example, Fig. 1-12 shows the pressure distribution inside a proton from DVCS data (V. D. Burkert, Elouadrhiri, and Girod, 2018), which has since been further investigated by theorists to generate similar mappings through LQCD as in Fig. 1-13

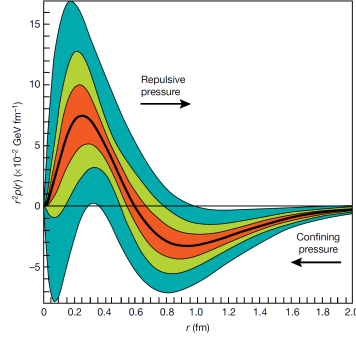


Figure 1-12: Proton Pressure Distribution from DVCS data, from (V. D. Burkert, Elouadrhiri, and Girod, 2018).

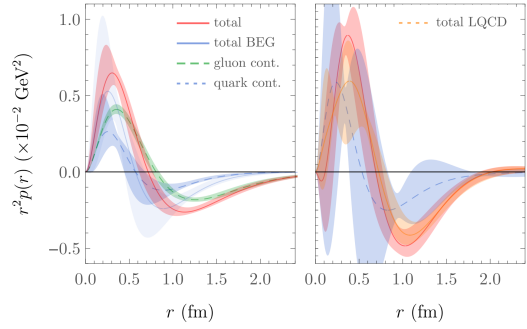


Figure 1-13: Proton Pressure Distribution from Lattice QCD, from (Shanahan and Detmold, 2019).

DVCS is primarily sensitive to non-quark spin flip GPDs (e.g.  $H$ ,  $E$ ), as are DVMP for vector mesons, such as the  $\rho$ . On the other hand, pseudoscalar meson production, such as pions, are sensitive to the transversity, or chiral-odd, GPDs. Additionally, some meson processes, such as  $\phi$  due to its strange quark content, are particularly sensitive to gluon GPDs. This work focuses on DVMP with the production of a neutral pion,  $\pi^0$ , which in addition to accessing chiral-odd GPDs, is an important background for other processes such as DVCS due to sample contamination from  $\pi^0$  decay (Lee, 2022).

## Deeply Virtual Neutral Pion Production

The Feynman diagram for Deeply Virtual Neutral Pion Production (DV $\pi^0$ P or DV $\pi^0$ P) is shown in Fig. 1-14.

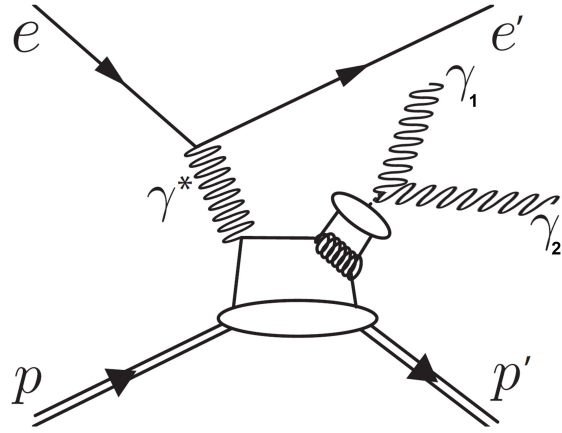


Figure 1-14: DV $\pi^0$ P Feynman Diagram.

The unpolarized cross section for DV $\pi^0$ P can be decomposed into longitudinal and transverse structure functions as in (1.21), the formalism for which is covered in (Donnachie and Shaw, 1978), (Dreschsel and Tiator, 1992), and (T. Donnelly, Jeschonnek, and Van Orden, 2023).

$$\frac{d^4\sigma_{ep \rightarrow ep'\pi^0}}{dQ^2 dx_B dt d\phi_\pi} = \Gamma(Q^2, x_B, E) \frac{1}{2\pi} \left\{ \left( \frac{d\sigma_T}{dt} + \epsilon \frac{d\sigma_L}{dt} \right) + \epsilon \cos(2\phi) \frac{d\sigma_{TT}}{dt} + \sqrt{2\epsilon(1+\epsilon)} \cos(\phi) \frac{d\sigma_{LT}}{dt} \right\}. \quad (1.21)$$

Here  $\Gamma$  is the virtual photon flux as in (1.22) and represents the number of virtual photons per scattered electron (Amaldi, Fubini, and Furlan, 1979),  $\epsilon$  is the ratio of transverse to longitudinally polarized photons (1.23),  $\phi$  is the angle between the lepton and hadron planes, as illustrated in Fig. 1-15, and the structure functions can be expressed as convolutions of GPDs as shown in (1.24)-(1.27) as discussed in (Bedlinskiy et al., 2014).

$$\Gamma(Q^2, x_B, E) = \frac{\alpha}{8\pi} \frac{Q^2}{m_p^2 E^2} \frac{1 - x_B}{x_B^3} \frac{1}{1 - \epsilon} \quad (1.22)$$

$$\epsilon = \frac{1 - y - \frac{Q^2}{4E^2}}{1 - y + \frac{y^2}{2} + \frac{Q^2}{4E^2}} \quad (1.23)$$

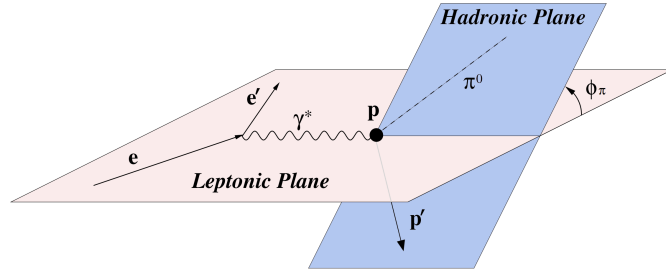


Figure 1-15: Diagram of Lepton-Hadron Plane Angle  $\phi$ .

$$\frac{d\sigma_L}{dt} = \frac{4\pi\alpha}{kQ^2} \left\{ (1 - \xi^2) |\langle \tilde{H} \rangle|^2 - 2\xi^2 \Re \left[ \langle \tilde{H} \rangle^* \langle \tilde{E} \rangle \right] - \frac{t'}{4m^2} \xi^2 |\langle \tilde{E} \rangle|^2 \right\} \quad (1.24)$$

$$\frac{d\sigma_T}{dt} = \frac{2\pi\alpha\mu_\pi^2}{kQ^4} \left\{ (1 - \xi^2) |\langle H_T \rangle|^2 - \frac{t'}{8m^2} |\langle \bar{E}_T \rangle|^2 \right\} \quad (1.25)$$

$$\frac{d\sigma_{LT}}{dt} = \frac{4\pi\alpha\mu_\pi}{\sqrt{2kQ^3}} \xi \sqrt{1-\xi^2} \frac{\sqrt{-t'}}{2m} \Re \left\{ \langle \textcolor{red}{H}_{\textcolor{red}{T}} \rangle^* \langle \textcolor{blue}{E} \rangle \right\} \quad (1.26)$$

$$\frac{d\sigma_{TT}}{dt} = \frac{4\pi\alpha\mu_\pi^2}{kQ^4} \frac{-t'}{16m^2} \langle \bar{E}_{\textcolor{violet}{T}} \rangle^2 \quad (1.27)$$

The terms involved in these expressions are:

- $t' = t - t_0$  where  $t_0 = \frac{-4m^2\xi^2}{1-\xi^2}$
- Skewness  $\xi = \frac{x_B}{2-x_B}$
- The bracket  $\langle \tilde{F} \rangle$  is the convolution of a GPD and an appropriate subprocess amplitude:  $\langle \tilde{F} \rangle = \sum_\lambda \int_{-1}^1 d\bar{x} H_{0\lambda,0\lambda}(\bar{x}, \xi, Q^2, t=0) \tilde{F}(\bar{x}, \xi, Q^2, t)$ 
  - $\lambda$  is the unobserved helicities of the partons participating in the subprocess
- Phase space factor  $k = 16\pi \left( W^2 - m^2 \right) \sqrt{\Lambda(W^2, -Q^2, m^2)}$ 
  - $\Lambda(W^2, -Q^2, m^2)$  is the Källén function:  $W^4 + Q^4 + m^4 + 2W^2Q^2 + 2Q^2m^2 - 2W^2m^2$
- Reduced pion mass  $\mu_{\pi^0} = \frac{m_{\pi^0}^2}{m_u + m_d}$ 
  - $m_u$  and  $m_d$  are respective masses of up and down quarks

### 1.2.3 Status of DV $\pi^0$ P Measurements

With theoretical advancements occurring in the mid 1990s to early 2000s, the first analyses of experimental measurements of DV $\pi^0$ P have only been released in the past decade.

## Summary of Existing Measurements

The earliest of such measurements were taken at the Thomas Jefferson National Accelerator Facility (JLab) with a  $\sim 6$  GeV electron beam. Two of the four experimental halls - Hall A ([Fuchey et al., 2011](#)) and Hall B ([Bedlinskiy et al., 2014](#)) produced cross section results. Hall A houses a small acceptance precision spectrometer and recorded data in several kinematic bins. Hall B housed a large acceptance spectrometer, yielding cross section measurements over a large kinematic regime.

Recent upgrades at JLab have nearly doubled the beam energy to 10.6 GeV, and both detector halls have accumulated data allowing for the measurement of this process. Both halls repeated data taking at this higher energy, with Hall A recently releasing updated cross section values across three fixed  $x_B$  bins (0.36, 0.48 and 0.6) and over a range of  $Q^2$  values from 3 to 9 GeV $^2$  ([Dlamini et al., 2021](#)).

This work expands on these results by covering a much larger kinematic regime, as well as having much higher statistics compared to the 6 GeV Hall B result. A kinematic overlap plot in  $Q^2$ ,  $x_B$  is shown in Fig. [1-16](#) summarizes these differences. It is also noted that the CERN COMPASS collaboration ([Alexeev et al., 2020](#)) has measured this process using a 160 GeV muon beam, obtaining results over a much lower  $x_B$  range.

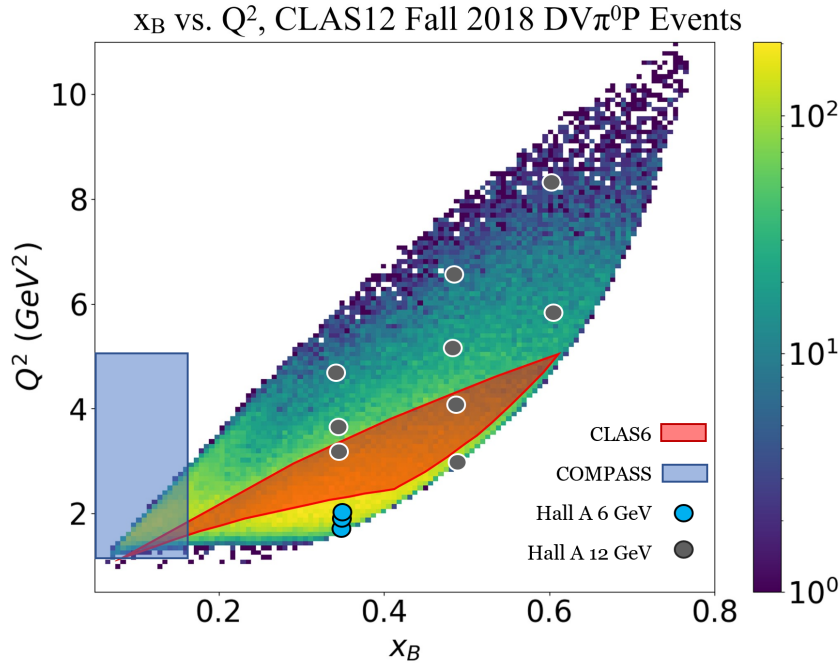


Figure 1-16: Kinematic reach plot between this work and other results: CLAS6 ([Bedlinskiy et al., 2014](#)), COMPASS ([Alexeev et al., 2020](#)), Hall A 6 GeV ([Fuchey et al., 2011](#)), and Hall A 12 GeV ([Dlamini et al., 2021](#)). The reach shown for Hall A are approximate areas around their reported bin centers.

## Overview of This Analysis

This work details the analysis of data taken at the JLab CLAS12 experiment to measure the deeply virtual neutral pion electroproduction cross section.

Chapter 2 describes the experimental setup. Chapter 3 discusses the computational and simulational infrastructure built and used as an integral part in estimating correction factors and performing an accurate measurement. Chapter 4 explains the specific analysis procedures and estimation methods used to arrive at cross section values. Chapter 5 presents further physics analysis, made possible with the extracted cross section values. Fig. 1-17 broadly summarizes the analysis flow; electronic read-

ers can conveniently click on boxes for hyperlinks to relevant sections.

statement introducing idea of posing this as an inverse problem, introduce the experimental interpretation of the cross section

Cross sections are theoretically interpreted as the probability for a specific interaction to occur. They can be experimentally estimated by measuring the occurrence frequency relative to the total possible interaction opportunities. In general, the cross section  $\sigma$  can be expressed as (1.28) the number of measured events of interest  $N_{meas}$  divided by the number of total interaction opportunities  $\mathcal{L}$ .  $\mathcal{L}$  is known as luminosity and is a product of only experimental parameters, such as the number of particles present and the experiment duration.

$$\sigma = \frac{N_{exp}}{\mathcal{L}} \quad (1.28)$$

Measuring the complete cross section at once is not feasible, so instead estimates are made of the differential cross section (1.29), which instead evaluates the probability for a specific interaction to occur in a differential region of phase space,  $\frac{d\sigma}{d\Omega}$ . Infinitesimal measurements are not possible, so events are counted over some small discretized generalized volume  $\Delta\Omega$ .

$$\frac{d\sigma}{d\Omega} = \frac{N_{exp}}{\mathcal{L}\Delta\Omega} \quad (1.29)$$

In practice, a number of correction terms need to be included to account for differences between experiment and theory. These correction terms, combined with the specifics of this analysis, yield the full experimental expression of the cross section (1.30).

$$\frac{d^4\sigma_{ep \rightarrow ep'\pi^0}}{dQ^2 dx_B dt d\phi_\pi} = \frac{N(Q^2, x_B, t, \phi_\pi)}{\mathcal{L}_{int} \Delta Q^2 \Delta x_B \Delta t \Delta \phi_\pi} \frac{1}{\epsilon_{acc} \delta_{RC} \delta_{Norm} Br(\pi^0 \rightarrow \gamma\gamma)} \quad (1.30)$$

The terms on the right-hand side of this equation are:

- $N(Q^2, x_B, t, \phi_\pi)$  - Number of events recorded in a given  $Q^2, x_B, t, \phi_\pi$  bin.
- $\mathcal{L}_{int}$  - Integrated luminosity
- $\Delta Q^2 \Delta x_B \Delta t \Delta \phi_\pi$  - These are the bin sizes or intervals for the variables  $Q^2, x_B, t$ , and  $\phi_\pi$ .
- $\epsilon_{acc}$  - Acceptance correction, which is a combination of detector efficiency and geometrical acceptance, determined through simulations.
- $\delta_{RC}$  - Radiative correction factor
- $\delta_{Norm}$  - Overall normalization factor
- $Br(\pi^0 \rightarrow \gamma\gamma)$  - Branching ratio of the decay of a neutral pion ( $\pi^0$ ) into two photons ( $\gamma\gamma$ ), which is most recently measured at 98.8131% [Husek, Goudzovski, and Kampf, 2019](#)

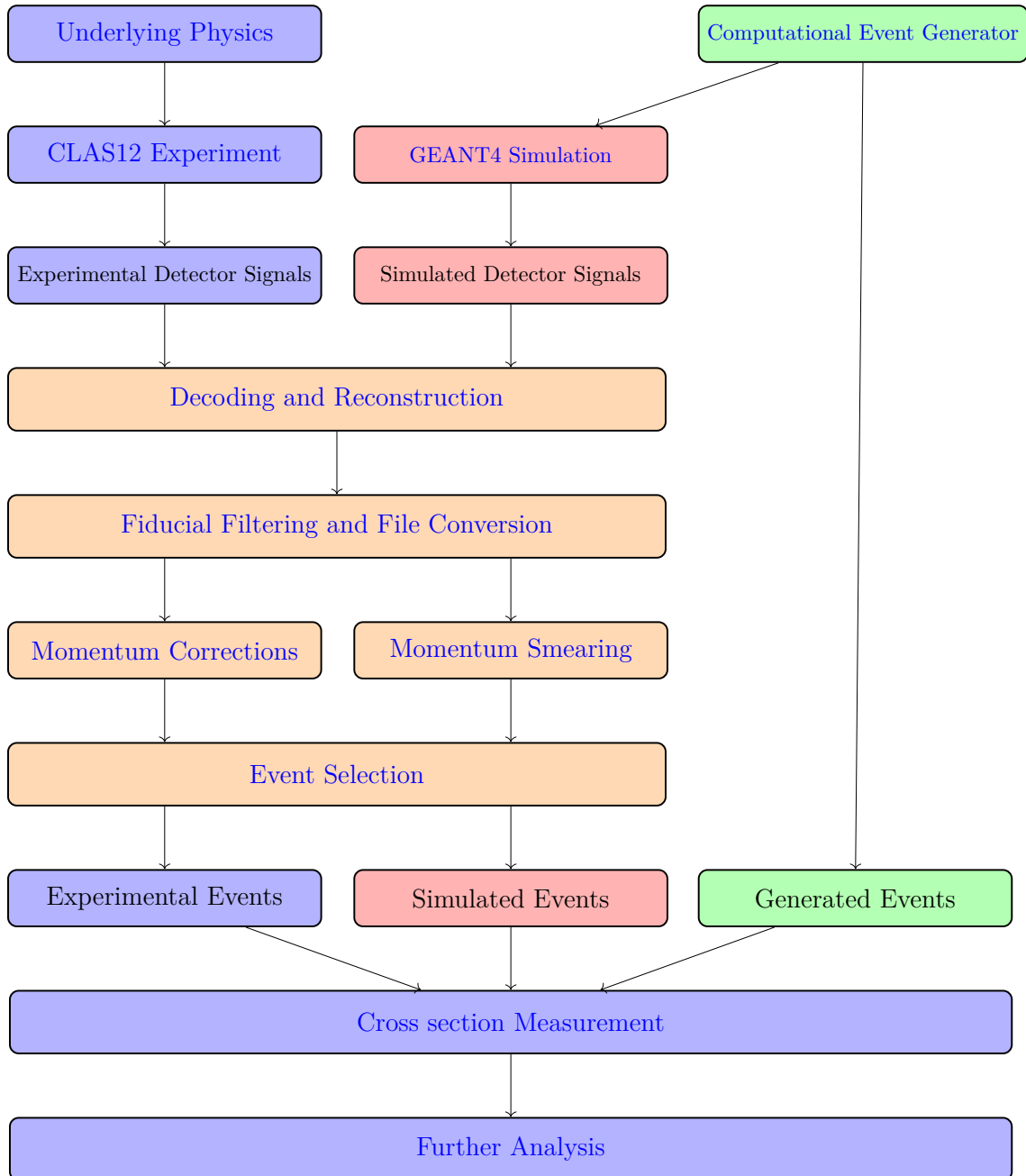


Figure 1-17: Analysis Overview Flowchart.

# Chapter 2

## Experiment and Data Processing

This experiment was conducted at the Thomas Jefferson National Accelerator Facility (TJNAF), located in Newport News, Virginia. The experimental apparatus was installed in Jefferson Lab Hall-B, and began taking data in Fall 2018.

### 2.1 Accelerator and Beamline

The Thomas Jefferson National Accelerator Facility, also called Jefferson Lab (JLab), is one of the 17 National Laboratories in the United States ([Department of Energy, 2023](#)), and functions mainly to deliver high energy, continuous wave (CW) electron beams to fixed-target nuclear and particle physics experiments. The facility was established in 1984 - initially named the Continuous Electron Beam Accelerator Facility (CEBAF) - and first delivered a 4 GeV electron beam on July 1 1994 to one of its three original detector halls. In 2006 efforts began to upgrade the facility to produce an electron beam up to 12 GeV in energy, which was first successfully delivered in 2015, as well as to construct a fourth detector hall for additional physics

experiments([Jefferson Lab, 2023](#)). JLab is also home to a free-electron laser, capable of 10+ kW CW operation ([Benson et al., 2007](#)).

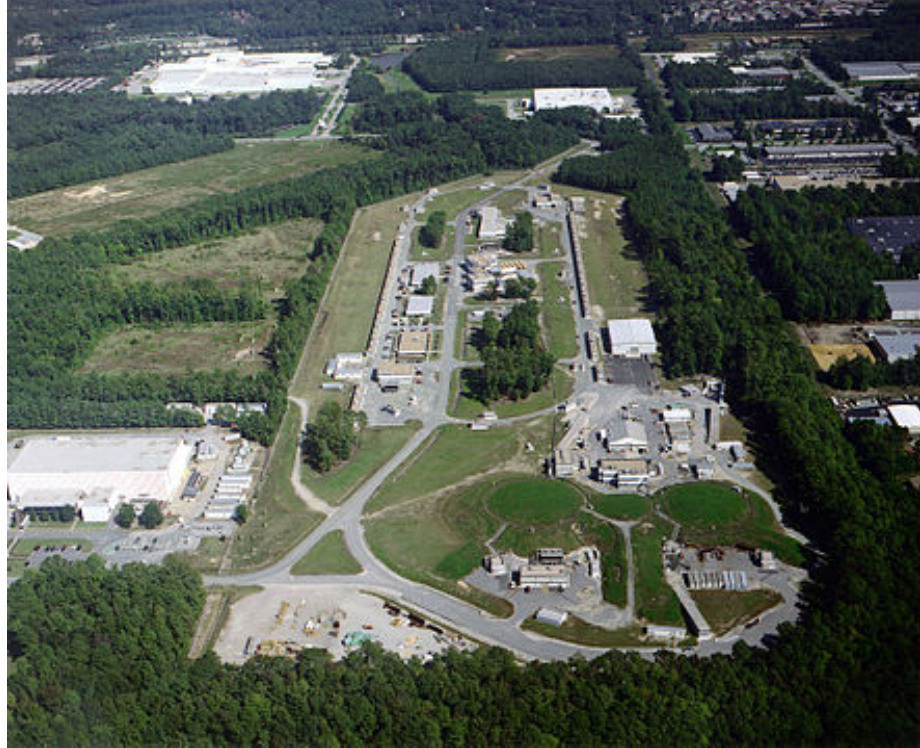


Figure 2-1: An aerial view of the Thomas Jefferson National Accelerator Facility ([Wang, 2010](#)). Note that this picture was taken before the addition of the fourth detector hall (Hall D).

### 2.1.1 Accelerator Facility

Fig. 2-2 shows the overarching scheme of the entire accelerator facility relevant for this experiment. Electrons are produced via the photoelectric effect from a 499 MHz pulsed laser impinges on a Gallium Arsenide photocathode Fig. 2-3a. The CEBAF guns operate at 100 kV and accelerate the electrons through a beam chopper Fig. 2-3b to create the desired beam structure Fig. 2-3c and into the main accelerator

circuit, where 1497 MHz superconducting resonator (SRF) cavities provide further acceleration Fig. 2-3d. CEBAF's two  $\sim$  1.1 GV linacs accelerate electrons by consist of 50 cryomodules total, with each cryomodule housing 8 7-cell SRF cavities and the liquid helium necessary to cool them, made possible by JLab's 2K liquid helium refrigerator, the largest in the world as of 2023. The electrons are steered around the curved parts of the track by dipole magnets Fig. 2-3e, making five complete circulations before delivery to the three western experimental halls, and an additional half circulation to achieve a full 12 GeV beam to Hall D.

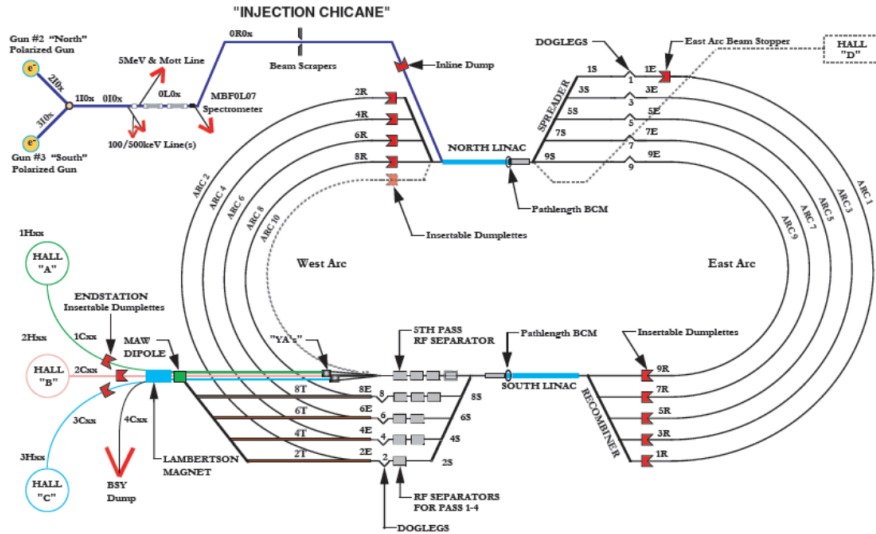


Figure 2-2: Schematic layout of the CEBAF accelerator at JLab. The racetrack configuration has two linear accelerator portions  $\sim$  1/4 mile long, and is  $\sim$  7/8 mile around (Wang, 2010).

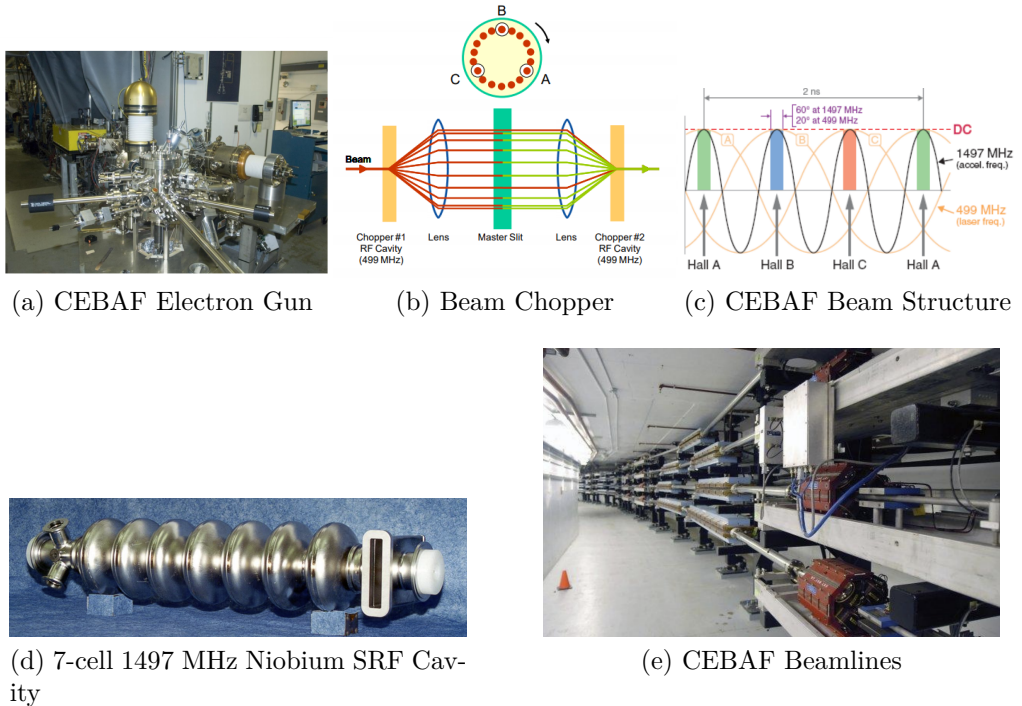


Figure 2-3: Electrons originate from the CEBAF guns (a) and pass through a beam chopper (b) to obtain the desired interlaced beam structure (c). The electrons are accelerated by superconducting RF cavities (d) and steered by dipole magnets (e) to reach an energy of 10.6 GeV before entering detector hall B. Images from ([Wang, 2010](#))

### 2.1.2 Hall B Beamline

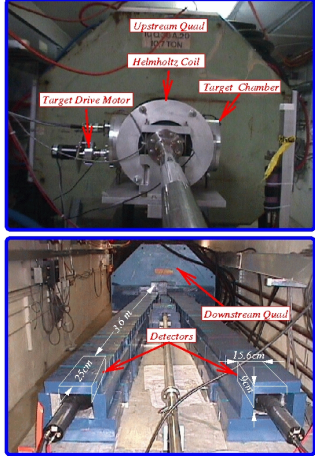
Quantity	Beam Property
Beam current	Up to 50 nA
Beam energy spread	$10^{-4}$
Beam size	Less than 0.4 mm
Beam stability	Less than 0.1 mm
Beam halo	$10^{-4}$
Beam polarization	Up to 85%

Table 2.1: Beam properties

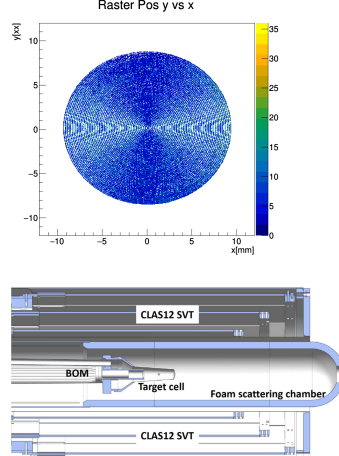
The beam enters Hall B with the nominal parameters as specified in Table 2.1. Upstream of the target, Hall B uses coincidence double arm Möller polarimeters Fig. 2-4a to measure beam polarization within a few percent accuracy. This analysis does not utilize the polarized beam for physics extraction, but it is useful for BSA measurements as well as other physics goals.

The beam is rasterized onto the target cell Fig. 2-4b is a 5 cm long Kapton cone with 23.66 and 15.08 upstream and downstream diameters respectively, with 30  $\mu\text{m}$  thick aluminum entrance and exit windows. The target used for this analysis consisted of unpolarized pure liquid hydrogen (LH<sub>2</sub>) and is located from -5.5 cm (upsteam) to -0.5 cm along the z-axis of the CLAS12 coordinate system (Baltzell et al., 2020).

The target is surrounded nearly in  $4\pi$  with detectors as discussed in the next section. The beamline ends in a beam dump and Faraday cup Fig. 2-4c, which measures the beam current to allow for absolute cross section determinations. The Faraday cup from the original CLAS experiment and is only rated for 175 Watts (16.5 nA at 10.6 GeV) so a beam blocker is utilized for full-beam runs. More details can be found in found in (Mecking et al., 2003)



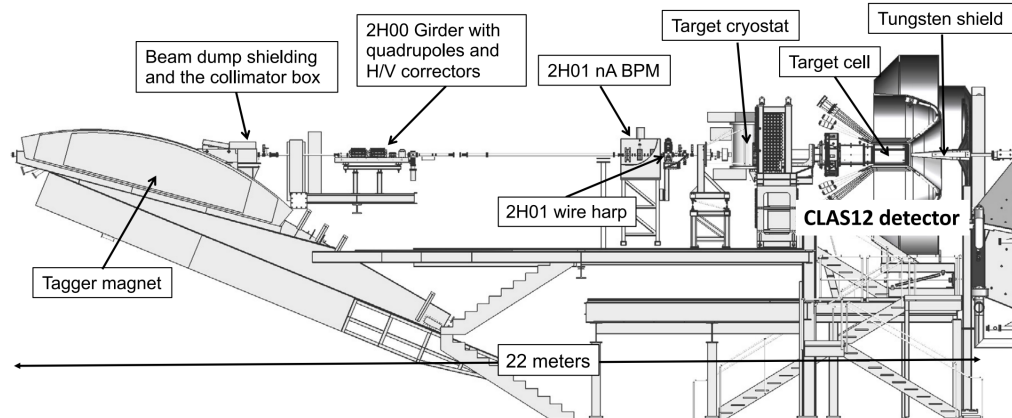
(a) Upstream (top) and downstream (bottom) view of Möller polarimeters ([Joo, 2002](#)).



(b) Rasterization pattern (top) on CLAS12 target (bottom) ([Achenbach, 2022](#)).



(c) Faraday cup, shown removed from operating position ([Achenbach, 2022](#)).



(d) Hall B beamline, from ([Baltzell et al., 2020](#)).

Figure 2-4: Overview of Hall B beamline. After Möller polarimeters (a), the electron beam is rasterized on CLAS12 target (b) with interactions recorded by the CLAS12 detector while the rest of the beam ends at the beam dump and Faraday cup (c). (d) shows the scaled detector hall layout, with the Möller polarimeters being located to the left of the Tagger magnet and the Faraday cup to the right of the CLAS12 detector package.

## 2.2 CLAS12 Detectors and Run Conditions

The CEBAF Large Acceptance Spectrometer, 12 GeV (CLAS12) detector occupies experimental Hall B at Jefferson Lab. It is an upgrade from its predecessor, the CLAS detector ([Mecking et al., 2003](#)), which operated in the 2000s during the 6 GeV era of JLab and laid the groundwork for the present detector system, which was commissioned in 2018. It covers nearly  $4\pi$  around the target cell, with comprehensive packages of detectors for particle position and energy tracking. It operates with data rates of comparable size to other large-scale, international physics experiments, as shown in Table 2.2. Data taking began in 2018 and has an experimental program approved into at least the early 2030s ([Battaglieri, 2021](#)).

Facility	Experiment	Event Size (kB)	L1 Trigger Rate (kHz)	Bandwidth to Storage (MB/s)
JLab	GlueX	15	200	300
JLab	<b>CLAS12</b>	<b>20</b>	<b>10</b>	<b>100</b>
LHC	ALICE	2,500	200	200
LHC	ATLAS	1,500	75	300
LHC	CMS	1,000	100	100
LHC	LHCb	40	1,000	100
BNL	STAR	1,000	0.6	450
BNL	PHENIX	60	15	450

Table 2.2: Assorted physics experiments and their typical data rates. Note that exact figures vary by source and run conditions. Adapted from ([David Lawrence, 2012](#)).

### 2.2.1 CLAS12 Detector System

The CLAS12 detector Fig. 2-5 has two major subsystems: the Forward Detector and the Central Detector, as well as a forward tagger (nested inside the forward detector package) and backward angle neutron detector (BAND).

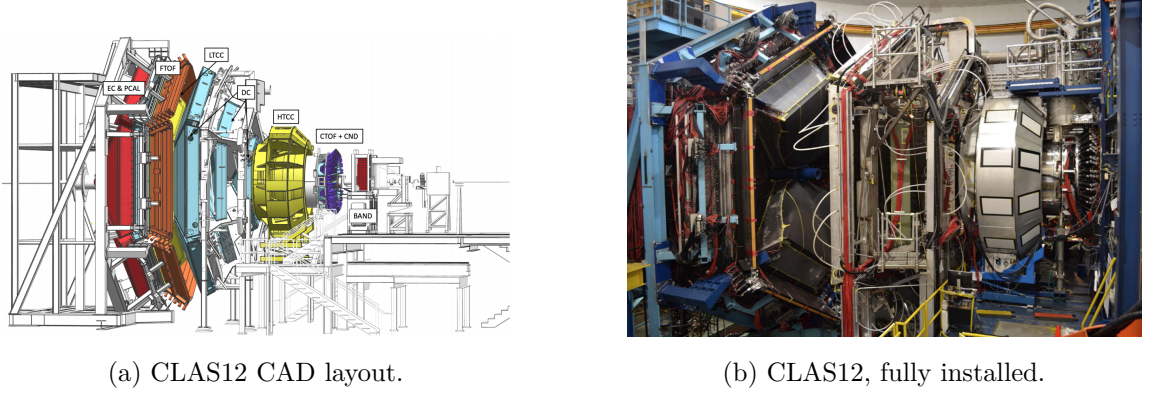


Figure 2-5: CLAS12 layout schematic and photograph, from ([V. Burkert et al., 2020](#)).

## Forward Detector

The Forward Detector (FD) is a 6-fold azimuthally symmetric segmented system containing several detector packages and a toroidal magnet. The sections follow a counterclockwise numbering convention where S1 corresponds to  $[-30^\circ, 30^\circ]$ , as in Fig. [2-6a](#). Working from the target downstream, the FD consists of a High Threshold Cherenkov Counter (HTCC) ([Sharabian et al., 2020](#)), Low Threshold Cherenkov Counter (LTCC) ([Ungaro et al., 2020](#)), the Ring Imaging Cherenkov detector (RICH) ([Contalbrigo et al., 2020](#)), Forward Time-of-Flight (FTOF) ([Carman et al., 2020](#)), Drift Chambers (DC) ([Mestayer et al., 2020](#)) embedded in a 3.5 Tesla torodial magnetic field ([Fair et al., 2020](#)), and Electromagnetic Calorimeter (ECal) complex ([Asryan et al., 2020](#)).

The ECal consists of three layers, two of which are from the previous CLAS experiment ([Amarian et al., 2001](#)). Those two layers were only sufficient to contain showers with energies below 5 GeV, so a third layer (Pre-shower Calorimeter, PCal) was added to address this issue, as well as introduce the finer grained segmenta-

tion necessary to resolve the angle between the two photons of a neutral pion decay, which is of special importance for this process measurement. The FD system covers approximately  $5^\circ$  to  $35^\circ$  in polar angle, with one layer of the FTOF (FTOF-2) extending coverage to  $45^\circ$ .

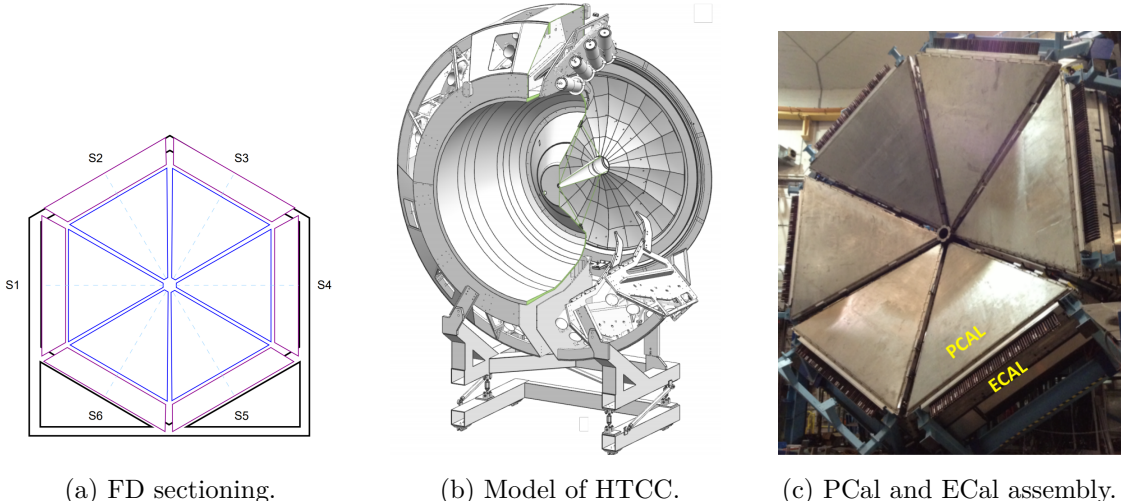


Figure 2-6: The FD is broken into six sections (a), with the exception of the first component after the target, the HTCC (b). The PCal was added to the ECal from the CLAS experiment to achieve the necessary particle resolution. From ([V. Burkert et al., 2020](#))

## Central Detector

The Central Detector (CD) also provides nearly  $2\pi$  azimuthal coverage, and spans from  $\sim 35^\circ$  to  $125^\circ$  in polar angle. The CD is an approximately 1 meter long cylinder inside a 5 Tesla solenoidal magnet ([Fair et al., 2020](#)) with four sub-detector packages. From the target working out, the packages are a Central Vertex Tracker Fig. 2-7b, made of a Barrel Micromegas Tracker (BMT) ([Acker et al., 2020](#)) and Silicon Vertex Tracker (SVT) ([Antonioli et al., 2020](#)), a Central Time-of-Flight (CTOF) 2-7a, and

a Central Neutron Detector (CND) (Chatagnon et al., 2020), which was installed but not used in this measurement.

Low momentum transfer  $t$  events correspond to large proton polar angles, meaning the majority of low- $t$  events occur with a proton detected in the CD. These events are important as the GPD interpretation of deeply virtual processes is only valid in the regime where  $\frac{-t}{Q^2}$  is small, and as such the CD is invaluable to acquiring data to gain insight on these distributions.

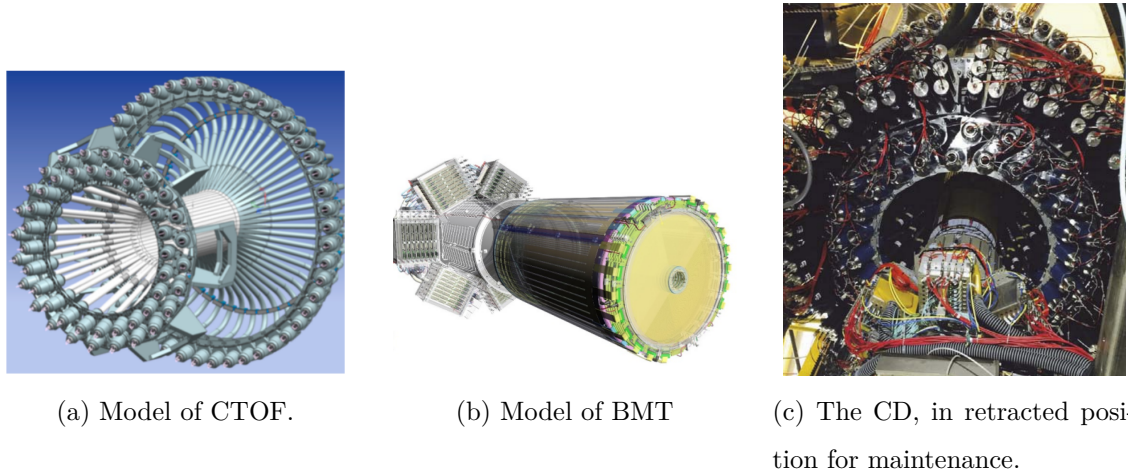


Figure 2-7: Models of the CTOF (a) and MVT (b) and their physical realizations (c). Images from (V. Burkert et al., 2020).

## Other System Components

At very low beam angles ( $2.5^\circ$ - $4.5^\circ$ ) there is the Forward Tagger (FT) [GET FT CITATION](#)

which contains a tracker, homogeneous calorimeter, and hodoscope. At the other end of the beamline ( $155^\circ$ - $175^\circ$ ) there is the Backward Angle Neutron Detector (BAND) (Segarra et al., 2020), which is not relevant for this analysis. Further-

more, the BAND and the Forward Micromegas Tracker (FMT) ([Acker et al., 2020](#))

#### **FIGURE OUT FMT vs BMT vs MVT**

were not installed at the time the data for this analysis was taken, although they have since been commissioned.

### **2.2.2 Experiment Run Conditions**

This work analyzes data obtained in the Fall 2018 run under the officially approved JLab project E12-06-108, which had a stated goal of measuring the electroproduction cross sections for pseudoscalar mesons ( $\pi^0$  and  $\eta$ ) ([Avakian et al., 2011](#)). The experiment ran at its design luminosity of  $10^{35} \text{ cm}^{-2} \text{ s}^{-1}$  and data was taken with the torodial magnetic field at both possible polarities - “outbending” or “+1” corresponding to bending the scattered electron away from the beamline, and “inbending” or “-1” corresponding to bending it towards the beamline. Data was taken at a beam energy of 10.6 GeV with a beam current of approximately 50 nA and a beam polarization of 86.9%. The data taking runs exceeded the original design DAQ requirements of a 10kHz event rate with 100 MB/s data rate to 12 kHz event rate with 550 MB/s data rate.

## **2.3 Reconstruction and Particle Identification**

During RG-A data taking, the event was triggered in parallel by three physics trigger systems: (1) the electron trigger, (2) photoproduction trigger and (3) opposite sector trigger. This analysis focuses on the (inclusive) electron trigger that is designed to record events with FD electron candidates with minimum  $n_{phe}$ ,  $E_{dep.}$ ,  $E_{dep.}PCAL$  conditions and the geometrical matching between detector subsystems. The electron

trigger search was adjusted and performed in parallel for each sector. The electron trigger system is highly efficient with 99.5% trigger efficiency and 95% DAQ livetime for trigger electrons of momentum above 2 GeV/c. The desired event rate for the RG-A experiment is about 20 kHz, which was estimated using the simulation. This can be easily achieved by the CLAS12 trigger logic with the effective performance level up to 200 kHz ([Raydo et al., 2020](#)). The events triggered by the electron trigger has trigger bits “1” (True) in any of bits 0 to 6, where the bits 1–6 stan for each sector and 0 is their OR. The trigger bits can be accessed offline. Processing all saved inclusive events is not efficient in many aspects. There are a lot more inclusive events than the exclusive channels of interest, namely DVCS and DV $\pi^0$ P. The RG-A has a few skimming modes, trains and wagons, to be commonly used for some specific channels. A train is a coarse skimming, such as the inclusive skim, which requires an electron-proton pair in one event. A wagon is a relatively finer skimming, such as the DVCS wagon, which requires one electron-proton-photon set with some level of DVCS exclusivity. The series of skimming processes is called data cooking. In this analysis, for the base data set we take the DVCS wagon that selects the DVCS candidates with loose exclusivity cuts, and require at least one  $e'p'\gamma$  set in the event [158](#) (see Section 3.3 for the cut conditions). The raw data is stored in the HIPO format [151](#) for the entire CLAS collaboration. The HIPO format has the advantages of fast Input/Output (I/O) speed, and compatibility with the Event I/O (EVIO) format that is commonly used for the Jefferson Lab event storage ([Wolin et al., 2007](#)). For this analysis, the python program with pandas library was taken as the main analysis tool in that python is supported by modern statistical packages [160,161](#) that are well maintained. This motivates operation of a custom pipeline to convert the data format to pickle, which is the python standard data format [162](#). We use the CLAS12ROOT [163](#), a software package to read the HIPO format in C++ and

store the related information in ROOT format [164](#). The ROOT formatted data is once again converted to pickle format, using the uproot library [165](#). By doing so, the data are reduced into  $M \times N$  dimensionality, where  $M$  is the number of events, and  $N$  is the number of physical quantities and other information that are related (Fig. 2-16). Different data formats have advantages in different stages of data processing. We filter the base data with the PID cuts introduced at Section 2.4 and save in another HIPO format, because the base data contains all detector responses. The filtered HIPO files are converted into ROOT format. Finally, we execute the python script to select DVCS and DV $\pi^0$ P events with tighter Event Selection criteria that will be described at 3.3 and save them in the pickle format.

Cooked hipo - PID cuts - filtered hipo - converting - converted root - dvep cuts  
- exclusive pickle

An electron candidate  $e'$  is defined as an associated signal of these FD signals: (1) a track in DC, (2) photoelectrons in HTCC, (3) hits in FTOF, (4) energy deposited over 60 MeV, and (5) the Sampling Fraction (SF) of Minimum Ionizing Particle's (MIPs). Here, the event start time is determined from the track information, and corrected by the RF signal and the vertex location. The momentum of a charged particle such as  $e'$  and the proton  $p'$  is reconstructed using the equation of motion in a magnetic field. The polar angle difference during the trajectory  $\Delta\theta$  is related to the momentum  $p$  and the charge  $q$  of the particle, and the line-integrated magnetic field along the trajectory curve, ( $\int B dl$ ) as

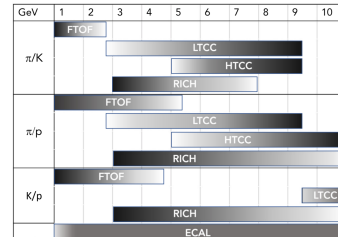
$$\frac{q}{p} = \frac{\Delta\theta}{c \int B dl} \quad (2.1)$$

During one event,  $p'$  is identified when there is a positively charged track in the DC or the CVT, associated with FTOF or CTOF hits for the timing. The flight time

$\Delta t_{p'}$  of  $p'$  is determined as the difference of TOF hits and event start time. Along with the path length  $l_{p'}$  and the momentum  $p_{p'}$  determined from the trajectory, the following relationship holds [151];

$$\beta p' \equiv \frac{vp'}{c} = \frac{lp'}{ctp'} = \frac{p'}{\sqrt{p'^2 + M^2 p}}$$

We take the common relativity notation for  $\beta = \frac{v}{c}$  where  $v$  is the velocity of the particle and  $c$  is the speed of light. Here,  $\chi \equiv \frac{\Delta t}{\sigma_{TOF}}$  with  $\Delta t \equiv \Delta t_{p',\text{expected}}(p') - \Delta t_{p',\text{measured}}$  is assigned to the particle as the signed distance function from the theoretical value. The photon  $\gamma$  can be reconstructed in the ECAL in FD, and the FT-Calorimeter in the FT. A photon will not produce charged tracks in the DC and the FT-Hodo associated with the existing calorimeter hits. More efficiently, the neutral hits are defined as the remaining calorimeter hits after all charged particles are assigned. The energy deposition in ECAL is converted to the actual photon energy using the SF. The homogeneous calorimeter FT-Cal takes the energy deposition as the photon energy.



(a)

Figure 2-8: Your caption goes here

The Data Acquisition (DAQ) ([Boyarinov et al., 2020](#))

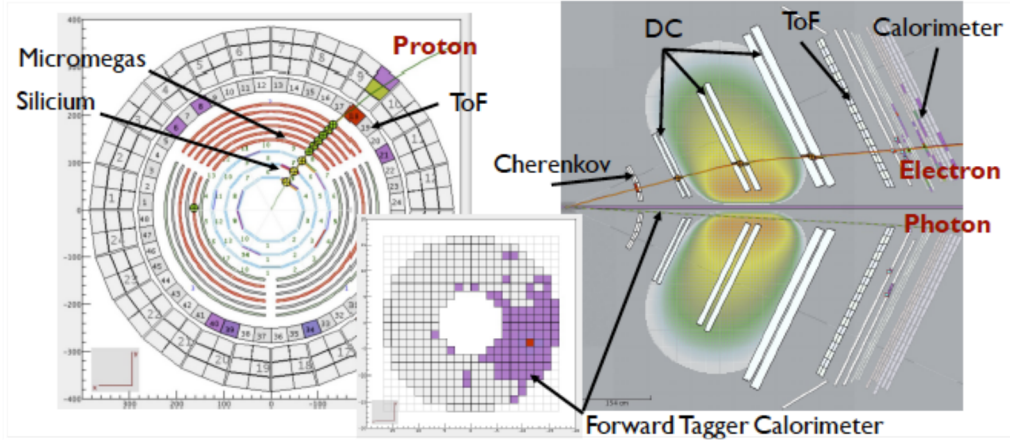


Figure 2-9: Caption from ([Battaglieri, 2021](#))

here we talk about CLAS PID  
cross section that requires the coincidence detection of electron, proton, and photon.

### 2.3.1 Decoding and Track Reconstruction

### 2.3.2 Particle Identification

\*\*photon cuts: pid 22, status > 2000 (in FD or CD, not ftagger) momentum greater than 400 MeV each

\*\*proton cuts: pid 2212

\*\*electron cuts: pid==1 and status < 0(negative particle

sangbaek lee thesis ([Lee, 2022](#))

For this analysis all final state particles should be detected. After  $\pi^0$  decay we are going to have 4 particles: electron, proton and two photons. The particle identification methods are applied to select the exclusive event with at least one electron, proton and two photons.

### **2.3.2.1 Electron**

### **2.3.2.2 Proton**

### **2.3.2.3 Photon**

### **2.3.2.4 Pion**

Basic event builder cuts are utilized, then additional cuts are made that are common with the RGA Analysis note ([overleaf link](#) and developed by Sangbaek Lee (sangbaek@mit.edu - [github code here](#)). For this analysis, both the central detector and forward detector are utilized for proton tracking. The forward tagger is also utilized for photon identification.

In addition to individual particle PID procedures the cut on the mass of two photons is applied:

- $0.07 < M_{\gamma\gamma} < 0.2 \text{ GeV}$

The pion is more thoroughly constrained by the exclusivity cuts, described in the next section.

## **2.3.3 Data Storage and Formatting**

### **2.3.3.1 Data Location and Availability**

### **2.3.3.2 File Formatting and Conversion**

Mention that same transformations are used for rec events and filtering

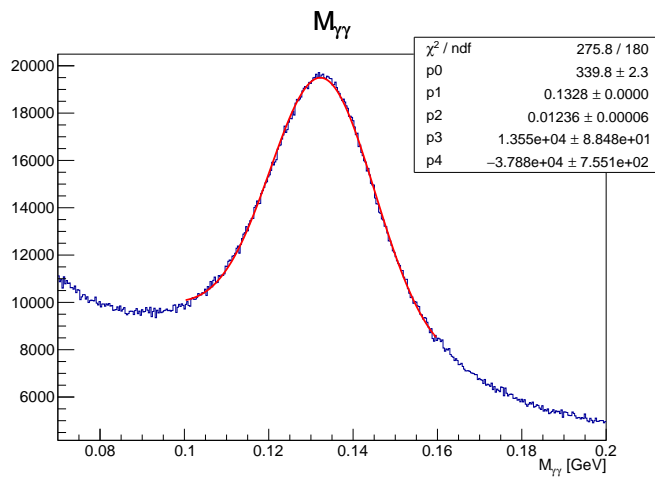


Figure 2-10: The distribution for mass of two photons  $M_{\gamma\gamma}$

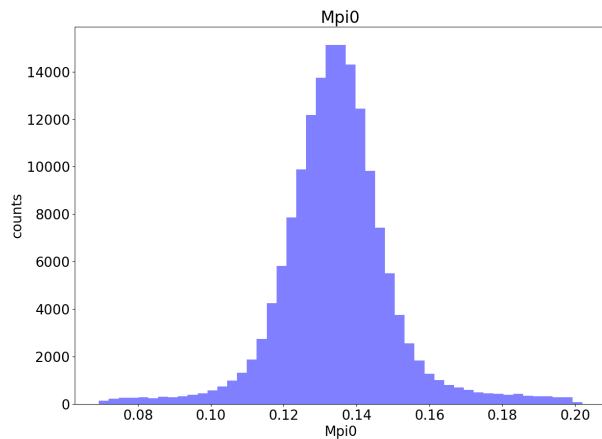


Figure 2-11: The distribution for mass of two photons after exclusivity cuts



# Chapter 3

## Simulations

### 3.1 Computing and Simulation Infrastructure

Motivation for massive simulations, inverse problem scope Discuss scale of data - how many simulations needed, how much data is produced, how long it takes to run simulations, cost and energy involved. overview: event generation - physics simulation - reconstruction - other

#### 3.1.1 MIT Tier 2 and Supercomputing Clusters

OSG MIT Tier 2 etc

#### 3.1.2 Overview of Simulation Runs

osg ([OSG, 2006](#)) ([Sfiligoi et al., 2009](#)) ([Pordes et al., 2007](#))

Data Reconstruction: 342 of the accumulated statistics ready for physics analyses (cooked data) 60G triggers, 1.2 PB raw data → 160TB DST → 100TB DST (16M core/hours processing time, 62.5M jobs processed)

Simulation hours: As for your question, if there is constant pressure then yes, MIT baseline would be constant.

However: need much more than 20K jobs / day to be at constant pressure. The dedicated resources + high priority can go up to 20K cores at once and if a job last 4 hours that's  $24/4 = 6 \times 20K = 120K$  jobs / day to be at constant pressure! Please do not submit that many jobs ;-)

You can check the monitoring page for more details. In particular you can select 1 month timeframe, and log scale. You will see holes in queue. And if you select just 'MIT' on the dedicated graph, you'll see the attached picture, where the 'holes' in the pressure are well shown and the number of MIT cores under pressure is about 3K.

Simulations are necessary in order to extract correction factors.

GEMC was used to process generated events through the CLAS12 fall 2018 RG-A configuration. Specifically, a generator based off the GK model and CLAS6 data - aao\_norad<sup>1</sup>.

## 3.2 Event Generation

Maid model discussion Xiaqing said that the following: [Dreschsel and Tiator, 1992](#) contains the formalism for the MAID model

You don't need much details about generator, it is based on GK model with Valery's fit to CLAS6 data.

NON RADIATED, INBENDING // Pi0 leptoproduction in Goloskokov-Kroll (GK) model. The code is currently being tested and implemented in PARTONS framework with additional features. If you plan to use this work in a publication,

---

<sup>1</sup>[https://github.com/drewkenjo/ao\\_norad](https://github.com/drewkenjo/ao_norad)

please use and reference the most recent version of PARTONS in <http://partons.cea.fr>

Andrey Kim and Nick Markov have the pi0 generator. It has my parametrization for  $W > 2$  GeV and MAID for  $W < 1.7$  GeV.

My model will for sure work for 12 GeV. It actually very close even for the COMPASS pi0 data (180 GeV muon beam).

There is reasonable coincidence between my model and MAID in the point  $W = 1.7$  GeV, not ideal but good enough for the MC.

I think actually that my parametrization has to work in the region  $W < 2$  GeV but I am not sure that MAID is doing good job due to the absence the experimental data at  $W = 1.7$  GeV.

Hi Bobby, Please take a look at README: [norad](#) It has instructions how to compile, run and configure the program. Please don't hesitate to ask questions!

For event generator we have aao\_rad can generate radiatied pi0 events in resonance region use 2007 model Put parameterization from valerly's paper, can cover up to whatever Q2 range covered in the paper, beyond that we put some general Q2 behaviour For Exclurad we have similar model, in end may have to iterate a few times to improve the model Exlclurad specifically for resonance region, theoretically should be correct, input probably needs to be updated, can put Valery's new parameterization to cover higher range. Should not be a real issue to implement it because same thing was done for AAORad. High q2 cannot be covered because parameterization only goes to CLAS6 range FX: the cruicail thing is to fold in the radiative corrections with acceptance and efficiens. Best mothod is to use fast monte carlo

aao\_rad and aao\_norad are event generators for exclusive pi0 and pi+ channels with/without radiative effects. They are written in Fortran. The program was initially developed by Volker Burkert long time ago for the resonance region, then has been evolved for many years and recently extended to DIS region even though

lots of things need to be done. Try this to see whether it works.

**A**mplitudes **A**nd **O**bservables (AAO)

### **3.2.1 Nonradiative Generator**

Include generator plots, specifics of layout

### **3.2.2 Radiative Generator**

Include generator plots, specifics of layout, plots showing W cut offs, etc

## **3.3 Simulation Pipeline**

### **3.3.1 Simulation Processing and JLab Computing**

volatile work To cancel all jobs: scancel -u robertej

To view all jobs: squeue -u robertej

### **3.3.2 Geant4, GEMC, and CLAS Submissions**

talk about own work on portals returns to vol, filtering and converting as covered in chapter 2

## 3.4 Simulation Enhancements with Normalizing Flows

### 3.4.1 Inverse Transforms and Autoregressive Flows

Introduce theory of MAFs

### 3.4.2 Exploration of Simulation Speedup with UNMAF

Discuss actual work performed



# Chapter 4

## Cross Section Measurement

Official Repo: <https://github.com/robertej19/clas12DVPiP>

For each kinematic bin the differential cross section can be written as:

$$\sigma = \frac{N_{meas}}{L\epsilon} \frac{1}{\delta} \quad (4.1)$$

Where  $\frac{N_{meas}}{L}$  is the number of events from experiment normalized by the integrated luminosity before acceptance and radiative corrections.  $\epsilon = \frac{N_{rec}^{RAD}}{N_{gen}^{RAD}}$  is the acceptance correction and  $\delta$  is the radiative correction.

$\delta$  can be obtained by using the following:

$$\delta = \frac{N_{gen}^{RAD}}{N_{gen}^{NORAD}} \quad (4.2)$$

$\delta$  and  $\epsilon$  need to be properly calculated, but for a first pass we will ignore them so we have just

## 4.1 General Analysis Overview

### 4.1.1 Part 1

### 4.1.2 part 2

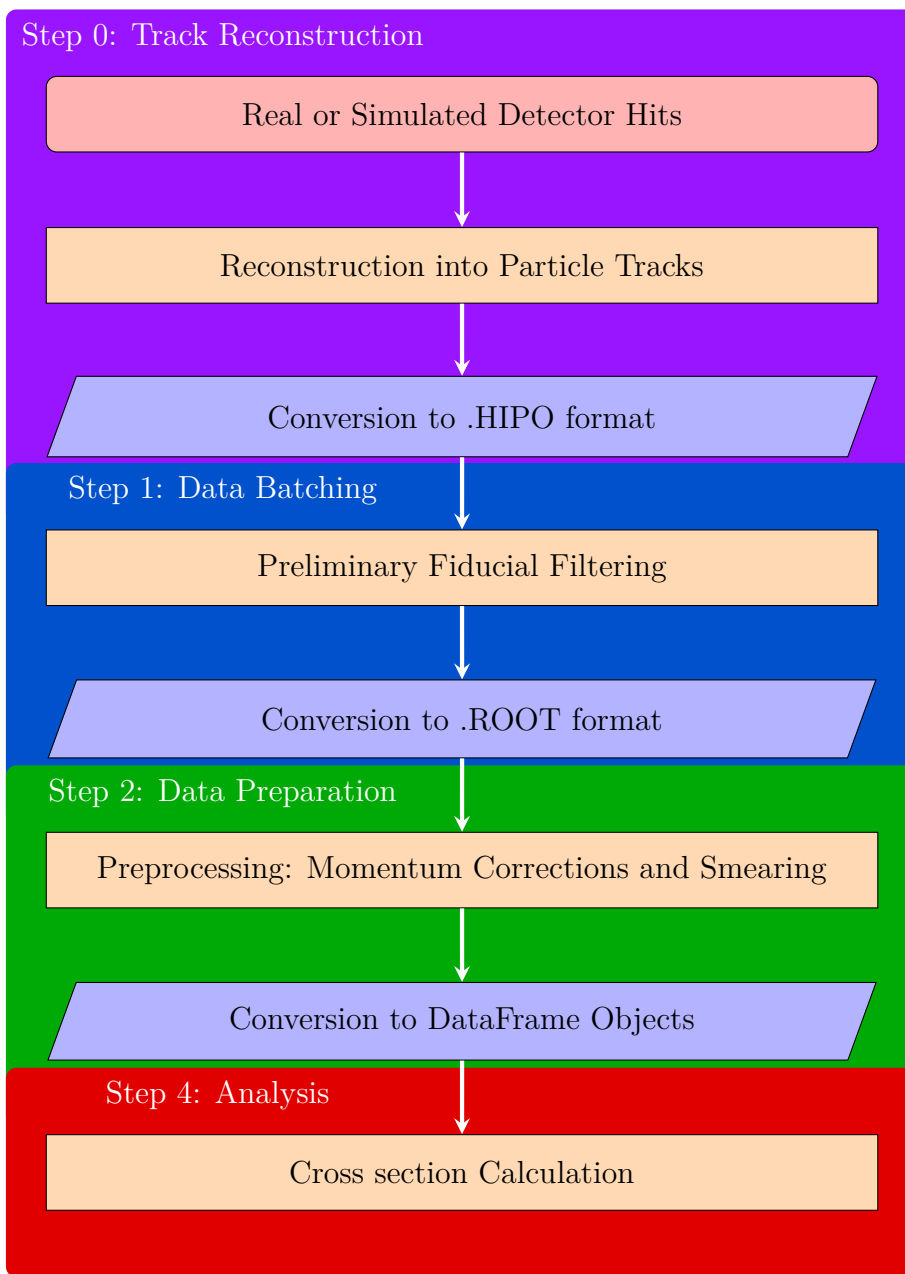


Figure 4-1: High-level data processing flow

## 4.2 Data Pre-Processing

### 4.2.1 Experimental Data Pre-Processing

#### 4.2.1.1 Momentum Corrections

Mom Corr

#### 4.2.1.2 Energy Loss Corrections

### 4.2.2 Simulation Data Pre-Processing

#### 4.2.2.1 Simulation:Experiment Resolution Matching

The standard aao simulations result in missing mass distributions that are too optimistic compared to experimental data. Observe the discrepancies between simulated and experimental distributions in figure 4-2.

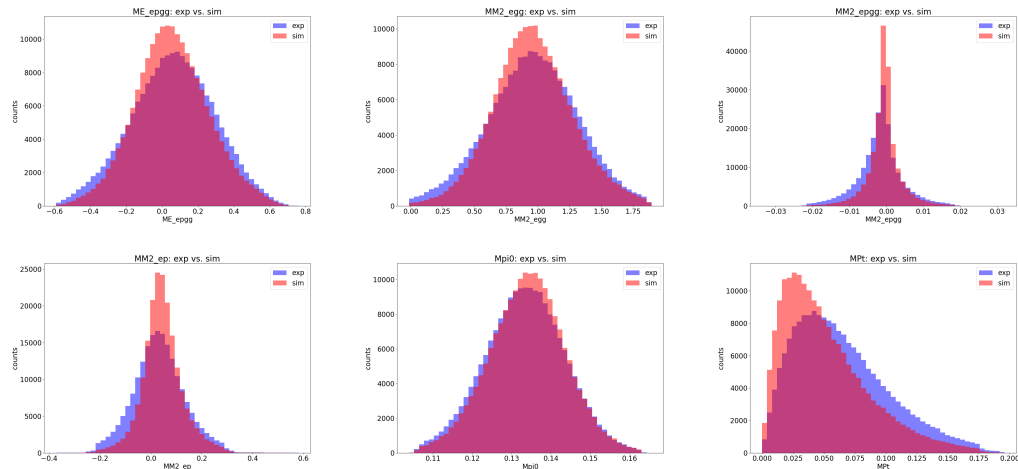


Figure 4-2: Comparison of experiment (blue) and simulation (red) missing mass, energy, momentum, and invariant gamma-gamma mass distributions, before any smearing factors were added to the simulation data.

To improve the matching between simulation and experiment, gaussian smearing factors were added after reconstruction to the simulated dataset. These factors were tuned by Sangbaek Lee to have optimal matching across all missing mass spectra combinations (figure 4-3). Once these factors were determined, the simulations were used to extract an acceptance correction.

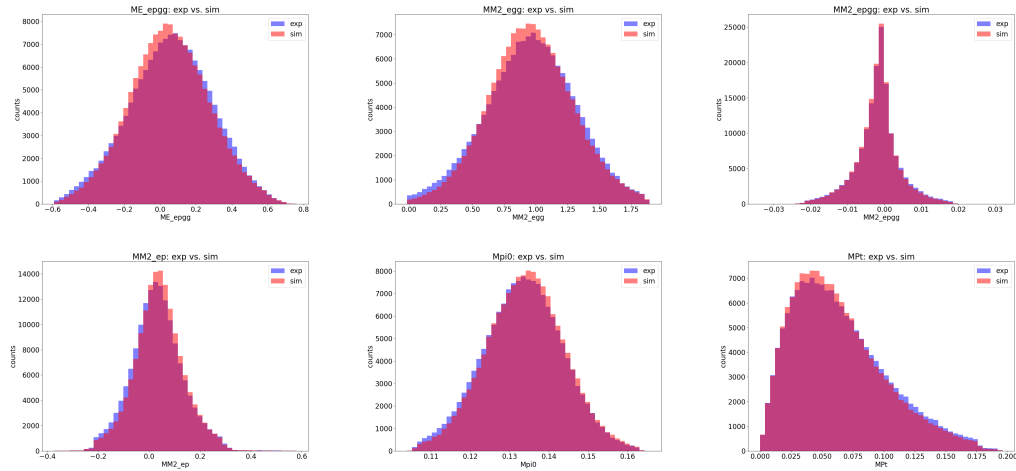


Figure 4-3: Comparison of experiment (blue) and simulation (red) missing mass, energy, momentum, and invariant gamma-gamma mass distributions, with smearing factors added to the simulation data proton and photon momenta.

## 4.3 Event Selection

Overview words about event selection

### 4.3.1 Exclusivity Cuts

After the selection of events with at least one electron, proton and two photons, it is time to take a look at the exclusive distributions. The Fig. 4-4 shows 2D distribution of  $MM^2$  (epX) vs  $\theta_{X\pi}$ , where  $MM^2$  (epX) is a missing mass squared of (epX) system and should have a peak near  $0.0182 \text{ GeV}^2$ , and  $\theta_{X\pi}$  is an angle

between expected and reconstructed pion. The bright spot on the figure corresponds to the exclusive  $ep \rightarrow ep\pi^0$  events. In order to reduce the background exclusivity cuts need to be developed based on the conservation of energy and momentum. The relevant 1D exclusive distributions are shown on the Fig. 4-5 and 4-6.

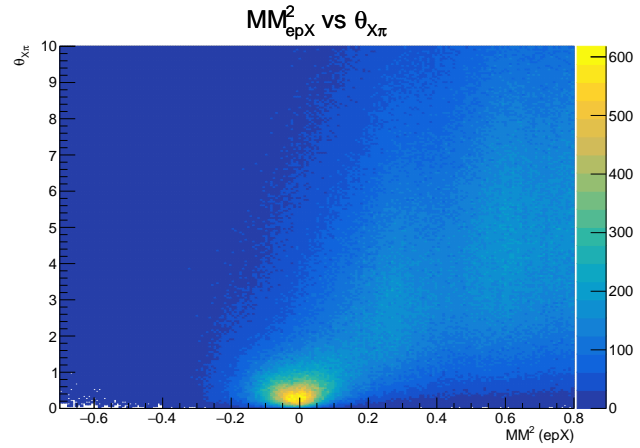


Figure 4-4:  $MM^2$  (epX) vs  $\theta_{X\pi}$  2D distribution.

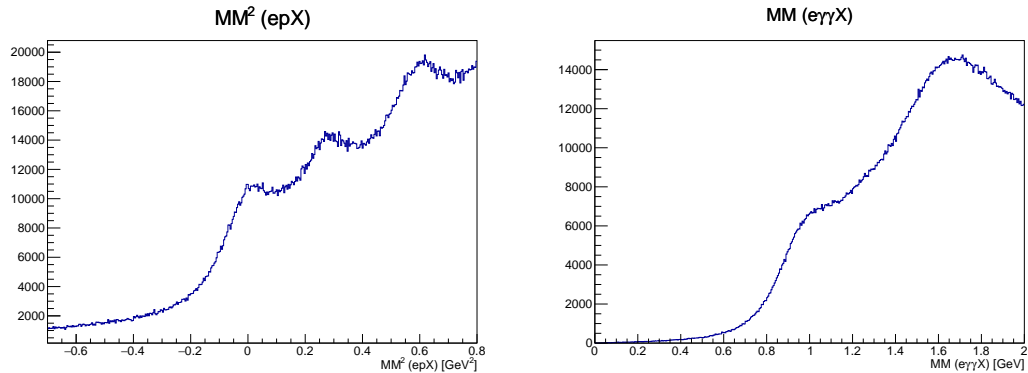


Figure 4-5: Exclusive distributions for events with at least one electron, proton and two photons.

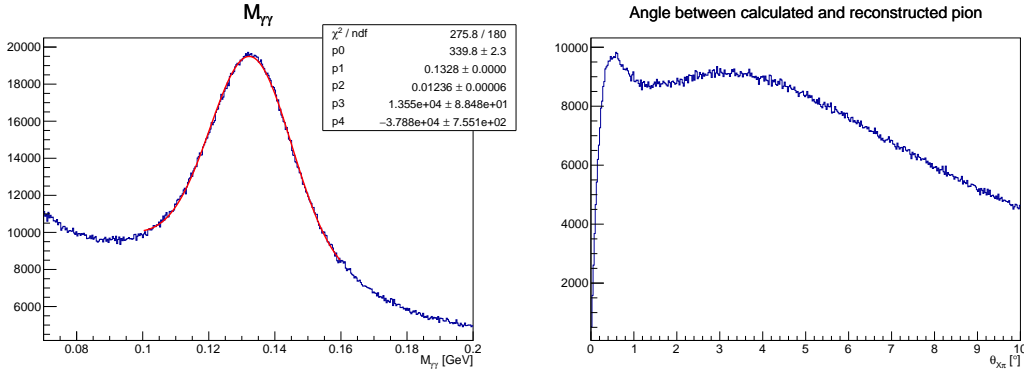


Figure 4-6: Exclusive distributions for events with at least one electron, proton and two photons.

#### 4.3.1.1 Tight $M_{\gamma\gamma}$ ass and transverse missing momenta cuts

The first step is to use tighter  $\gamma\gamma$  mass cut:  $0.096 < M_{\gamma\gamma} < 0.168$  GeV, and take a look at the missing transverse momentum distributions (see Fig. 4-7). From momentum conservation law we expect transverse momentum to be zero, so we can apply cuts on  $\Delta p_x$  and  $\Delta p_y$  to further improve exclusive channel selection. The cuts  $|\Delta p_x| < 0.2$  and  $|\Delta p_y| < 0.2$  correspond roughly to 4-5  $\sigma$ .

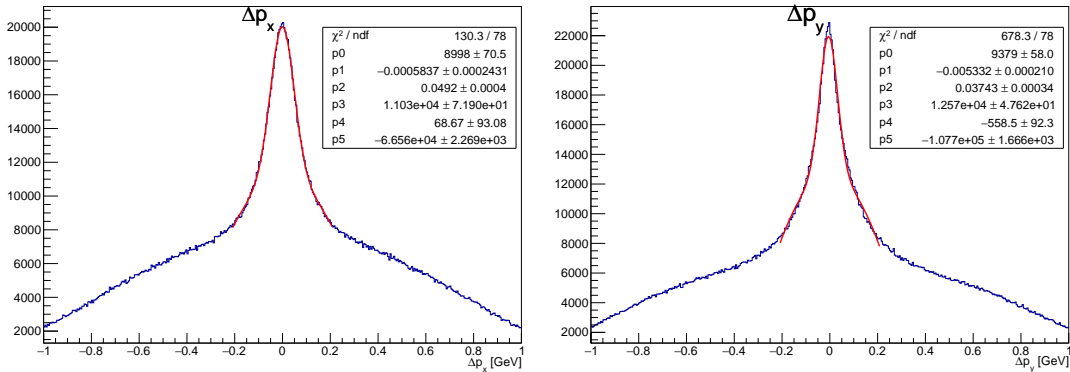


Figure 4-7: Exclusive distributions for events with at least one electron, proton and two photons.

The exclusive distributions after tight  $M_{\gamma\gamma}$  mass and transverse missing momenta

cuts are shown on Fig. 4-8 and display much stronger signal peaks on top of reduced background.

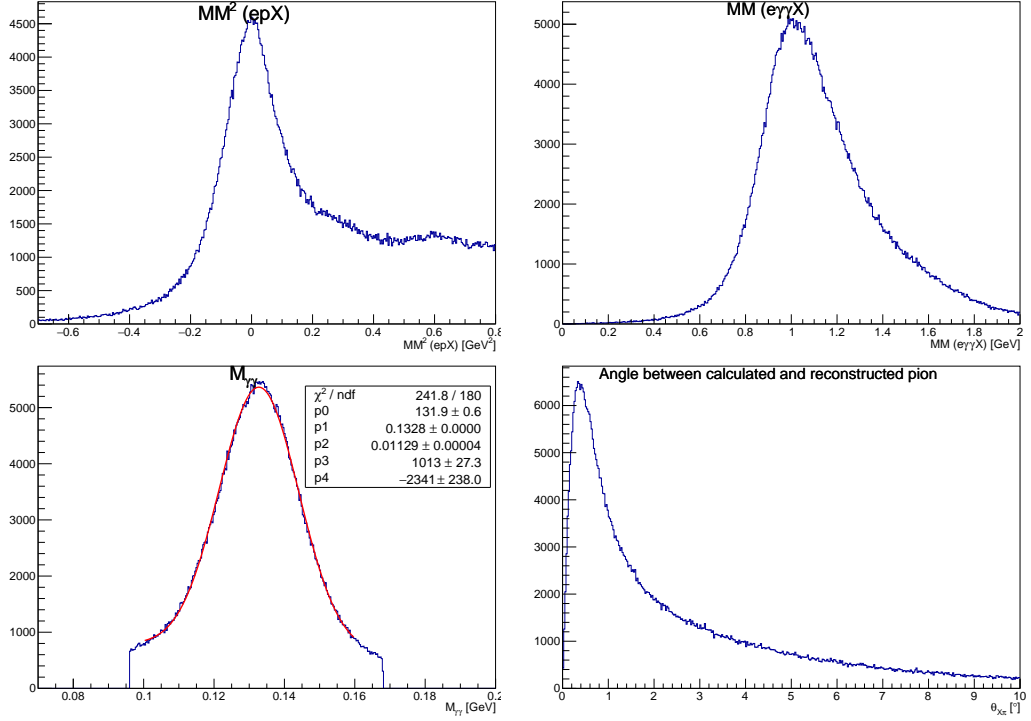


Figure 4-8: Exclusive distributions after tight  $M_{\gamma\gamma}$  mass and transverse missing momenta cuts .

#### 4.3.1.2 $\theta_{X\pi}$ ut determination

The cut on angle between expected and reconstructed pion is used in order to further reduce background. To choose the value of the  $\theta_{X\pi}$  cut the  $MM^2(epX)$  distribution is analyzed at multiple  $\theta_{X\pi}$  cut values and fit using gaussian+polynomial function as shown on Fig. 4-9. From the fit we can estimate the number of good exclusive events (gaussian) and the number of background events (polynomial) and their dependence on  $\theta_{X\pi}$  cut. Fig. 4-10 and 4-11 show the numbers of signal and background events

as functions of  $\theta_{X\pi}$  cut value for multiple bins in  $Q^2$  and  $x_B$ . These plots show that the cut  $\theta_{X\pi} < 2^\circ$  allows to select the most number of good events with the least background, and relaxing it beyond  $2^\circ$  does not gain us any good exclusive events but increases background.

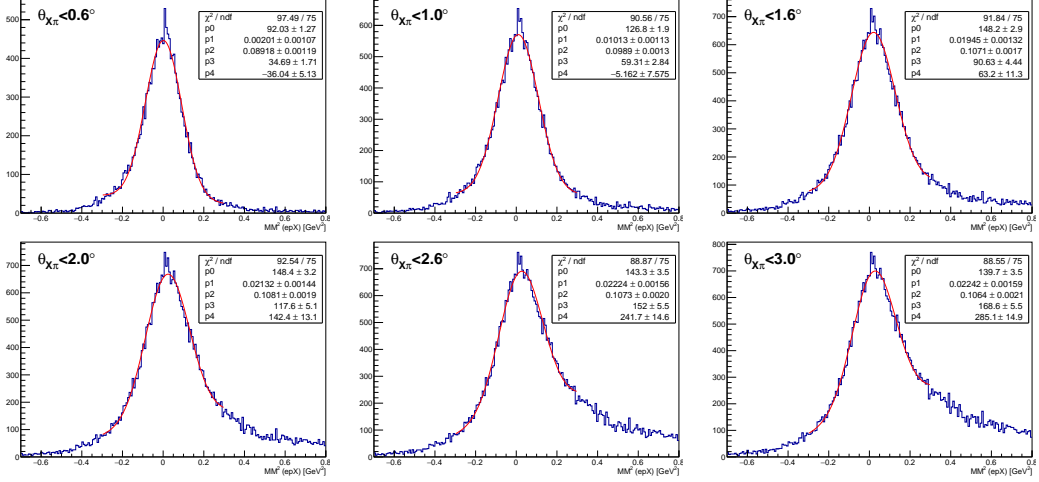


Figure 4-9:  $MM^2(epX)$  distributions for multiple  $\theta_{X\pi}$  cut values.

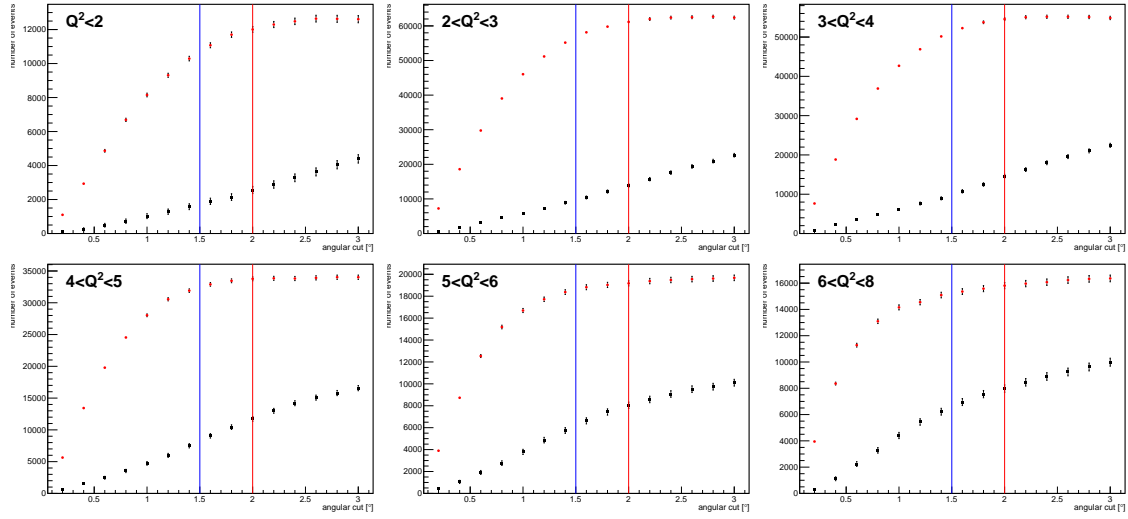


Figure 4-10: The numbers of signal (red markers) and background (black markers) events as functions of  $\theta_{X\pi}$  cut value for multiple  $Q^2$  bins.

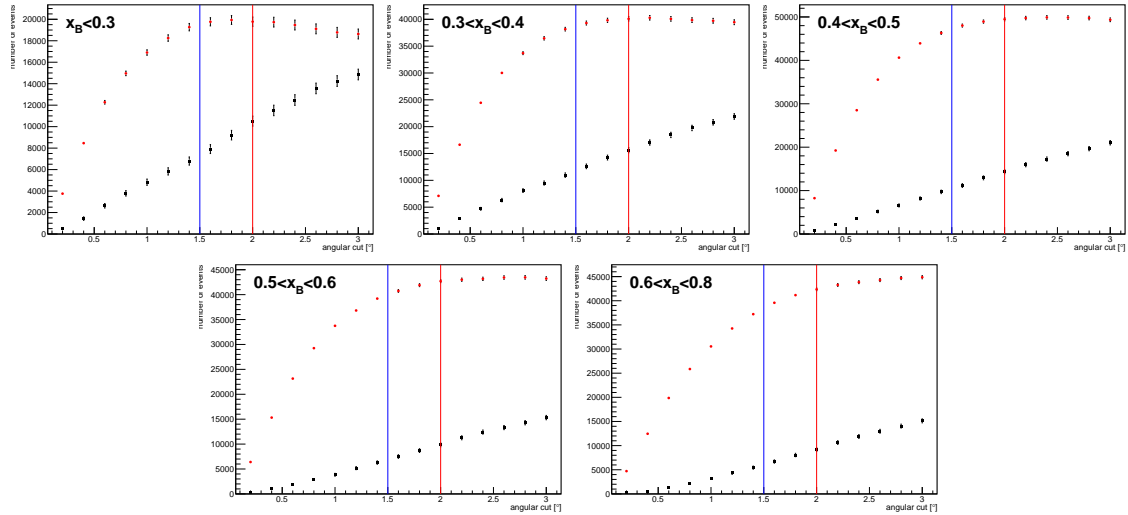


Figure 4-11: The numbers of signal (red markers) and background (black markers) events as functions of  $\theta_{X\pi}$  cut value for multiple  $x_B$  bins.

### 4.3.1.3 Final exclusivity cuts

The list of final exclusive cuts is following:

- $\Delta p_x < 0.2 \text{ GeV}$
- $\Delta p_y < 0.2 \text{ GeV}$
- $\theta_{X\pi} < 2^\circ$
- $0.096 < M_{\gamma\gamma} < 0.168 \text{ GeV}$
- $MM^2(epX) < 0.5 \text{ GeV}^2$

Exclusive distributions after all exclusivity cut except  $MM^2(epX) < 0.5 \text{ GeV}$  are shown on Fig. 4-12

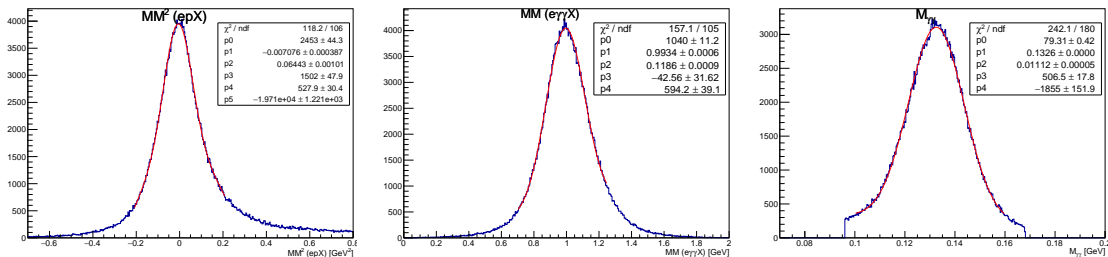


Figure 4-12: Exclusive distributions after all exclusivity cuts .

To arrive at a DVEP candidate event, we do the following

Code flow:

Consider a directory with n hipo files. For each hipo file, do the following.

Read each file event by event, and do the following

Check that the event has the proper databanks, and if not, go to teh next event.

Get a list of all the electrons\*, protons\*, and photons\* in the event

\*= links to most up to date PID methods

for every electron in the event (always only one, at least in the skims, but not held to be one) do the following  
For every proton in the event, do the following

Calculate some basic quantities and fill histograms

for every permutation of pairs of photons in the event, do the following

calculate various kinematic quantities, and pass to see if creates a viable pion\*  
and a viable DVEP event\*

if so, fill relevant histograms and count as a DVEP event, otherwise skip to next  
event

viable pion: pion mass between 100 and 180 MeV pion momentum greater than  
1.5 GeV angle (theta) between each photon and the electron to be greater than 8  
degrees

viable DVEP event: Q2 greater than 1 W greater than 2 difference between  
theta of missing 4-momentum and reconstructed pion less than 2 degrees difference  
between missing X px and py 300 MeV each or less Difference in missing mass squared  
between pion and X less than 1 GeV \*\* make sure this is right difference in missing  
energy and X less than 1 GeV \*\*make sure this is right

### 4.3.2 Kinematic Fitting

Instead of rigid cuts, we can use maximum likelihood estimators - include notes from  
Janet's class

## 4.4 Luminosity

The strategy to calculate the luminosity is as follows:

- For each run, retrieve a measure of how much beam passed through the target, I believe in the case of CLAS12 using the Faraday cup to measure beam charge - sum the beam charge over all runs being considered and include any relevant corrections factors - multiply this by target length, density, etc. to get the integrated luminosity
- use this value to calculate cross sections.

Compare integrated luminosity of CLAS6 to CLAS12 (in 2011 analysis note)

Implementation: The bank `REC::Event` has an object `beamCharge`, in nanoCoulombs, which is described in the `DST` as “beam charge integrated from the beginning of the run to the most recent reading of the gated Faraday Cup scaler in `RAW::scaler`, with slope/offset conversion to charge from CCDB. Note, this value will be zero in each file until the first scaler reading in that file.”. This is the (un?)gated beam charge.

This can be accessed via:

```
def banknames = [ 'REC::Event' , 'REC::Particle' , 'REC::Cherenkov' , 'REC::'

if (banknames . every{event . hasBank( it )}) {
    def (evb , partb , cc , ec , traj , trck , scib) = banknames . collect {even
def fcupBeamCharge = evb . getFloat ( 'beamCharge' , 0)
```

According to [this](#) we might need to use `tag=1 RAW::scaler::fcupgated` instead of `REC::Event::beamCharge`

The beam charge needs to be converted to integrated luminosity, which can be done as follows:

Luminosity: Events are not necessarily time ordered, need to take largest value minus smallest value

Luminosity is calculated according to equation 4.3

$$\mathcal{L} = \frac{N_A l \rho Q_{FCUP}}{e} \quad (4.3)$$

The terms in equation 4.3 are as tabulated in table 4.4. The accumulated charge on the Faraday cup is calculated by taking difference between the maximum and minimum values of beamQ for each run, and then summing these values. The luminosity determined for the fall 2018 inbending run was 5.5E+40 cm<sup>-2</sup> and the fall 2018 outbending run was 4.65E+40 cm<sup>-2</sup>

Quantity	CLAS12 Value	
Avogadro's Number	$N_A$	$6 \times 10^{23}$
Electron Charge	$e$	$1.6 \times 10^{-19}$
Target Length	$l$	5 cm
Target Density	$\rho$	0.07 g/cm <sup>3</sup> (LH2)
Charge on Faraday Cup	$Q_{FCUP}$	In data

Table 4.1: Terms of Luminosity Equation

We can calculate the luminosity L through the following equation

$$L = \frac{N_A l \rho Q_{FCUP}}{e} \quad (4.4)$$

Where  $N_A$  is Avogadro's constant,  $l$  is the length of the target,  $\rho$  is the density of the target (liquid hydrogen),  $Q_{FCUP}$  is the charge collected on the Faraday cup, and  $e$  is the charge of the electron. The values of these quantities are (ignoring uncertainties on experimental quantities for the time being):

$$N_A = 6.02214 \times 10^{23}$$

$$l = 5 \text{ cm}$$

$$\rho = 0.07 \text{ g/cm}^3$$

$$e = 1.602 \times 10^{-19} \text{ Coulombs}$$

$Q_{FCUP}$  - this must be measured and obtained from analysis. Typical runs at CLAS12 have an accumulated beam charge of tens to hundreds of thousands of nanoCoulombs.

## 4.5 Binning

Words about binning

## 4.6 Correction Factors

### 4.6.1 Acceptance Correction

### 4.6.2 Radiative Corrections

### 4.6.3 Bin Volume Corrections

The bin volume is not always kinematically full, for example the a large number of bins are kinmeatically restricted, no number of events could ever be found. SO, the bin shape is changed / adjusted for particularly empty bins.

#### **4.6.4 Bin Migration Corrections**

#### **4.6.5 Overall Normalization Corrections**

### **4.7 Uncertainty Estimation**

### **4.8 Iterative Bayesian Unfolding**

Here we talk about Iterative Bayesian unfolding to not have bin migration issues

Notes on Omnidfold from Anselm Vossen: I find this reference paper - [arxiv](#).

Yes, that is the reference. You saw that I also posted a reference to the Hera analysis. I don't think many others have used omnifold yet, since it is quite computationally intensive etc. My understanding is that Ben Nachman developed this and there has been follow up work by his group (if you just put his name into inspire you'll see). E.g. I saw presentations on how to present the data. Here is a talk by Ben at a Jet workshop in 2021: [this paper](#) Miguel Arratia, who is also in CLAS collaborated on the H1 results. You could ask him for practical advice,

# Chapter 5

## Results and Further Analysis

### 5.1 Cross Section Results

The experimental cross section is given by equation 5.1

$$\frac{d^4\sigma_{\gamma^* p \rightarrow p' \pi^0}}{dQ^2 dx_B dt d\phi_\pi} = \frac{N(Q^2, x_B, t, \phi_\pi)}{\mathcal{L}_{int} \Delta Q^2 \Delta x_B \Delta t \Delta \phi} \frac{1}{\epsilon_{ACC} \delta_{RC} \delta_{Norm} Br(\pi^0 \rightarrow \gamma\gamma)} \quad (5.1)$$

$N(Q^2, x_B, t, \phi_\pi)$  is the raw number of events in a specific kinematic bin and is calculated as described in chapter 4.  $\mathcal{L}_{int}$  is the integrated luminosity over the run of the experiment under analysis and is calculated as described in chapter 4.4.  $\Delta Q^2 \Delta x_B \Delta t \Delta \phi$  are the bin widths for the 4 kinematic binning variables.  $\epsilon_{ACC}$  is the acceptance correction, and is calculated as described in chapter 4.  $\delta_{RC} \delta_{Norm} Br(\pi^0 \rightarrow \gamma\gamma)$  are the radiative, overall, and branching ratio correction factors, and are not yet included in this cross section calculation.

Initial investigations show that radiative corrections will be on the order of 5%, the branching ratio is a 1.2% correction, and the overall normalization is not yet

determined but was 10% for the CLAS6 experiment; we expect the CLAS12 experiment overall normalization will be similar or less in magnitude. Thus, all of these corrections are much smaller than the acceptance correction, and will be included in future work but are not critical for preliminary analysis work.

The accepted results from the CLAS6 experiment [Bedlinskiy et al., 2014](#) can be used as a cross check for this work. Published values for the reduced cross sections from the CLAS6 experiment for the DV $\pi^0$ P channel are available [here](#). To calculate the reduced cross sections, we divide the cross section as described in equation 5.1 by the virtual photon flux factor  $\Gamma$  for each kinematic bin, where  $\Gamma$  is calculated as described in chapter 4.4. The reduced cross section is then given by equation 1.28.

$$\frac{d^2\sigma_{\gamma^* p \rightarrow p' \pi^0}(Q^2, x_B, t, \phi_\pi, E)}{dt d\phi} = \frac{1}{\Gamma_V(Q^2, x_B, E)} \frac{d^4\sigma_{\gamma^* p \rightarrow p' \pi^0}}{dQ^2 dx_B dt d\phi_\pi} \quad (5.2)$$

$$\frac{d^2\sigma_{\gamma^* p \rightarrow p' \pi^0}}{dt d\phi} = \frac{1}{\Gamma_V(Q^2, x_B, E)} \frac{N(Q^2, x_B, t, \phi_\pi)}{\mathcal{L}_{int} \Delta Q^2 \Delta x_B \Delta t \Delta \phi} \frac{1}{\epsilon_{ACC} \delta_{RC} \delta_{Norm} Br(\pi^0 \rightarrow \gamma\gamma)} \quad (5.3)$$

Some plots of reduced cross section for CLAS12 outbending Fall 2018 dataset are shown in figure 5-1. The cross sections show good agreement with the published CLAS6 results. The outbending dataset is contains mostly lower  $Q^2$  events and the inbending dataset is not yet properly analyzed, so higher  $Q^2$  comparisons are not available for this analysis note.

To compare these results, we can examine the form of the differential cross section, under the single photon exchange assumption we can write the differential cross section as in equation 1.29

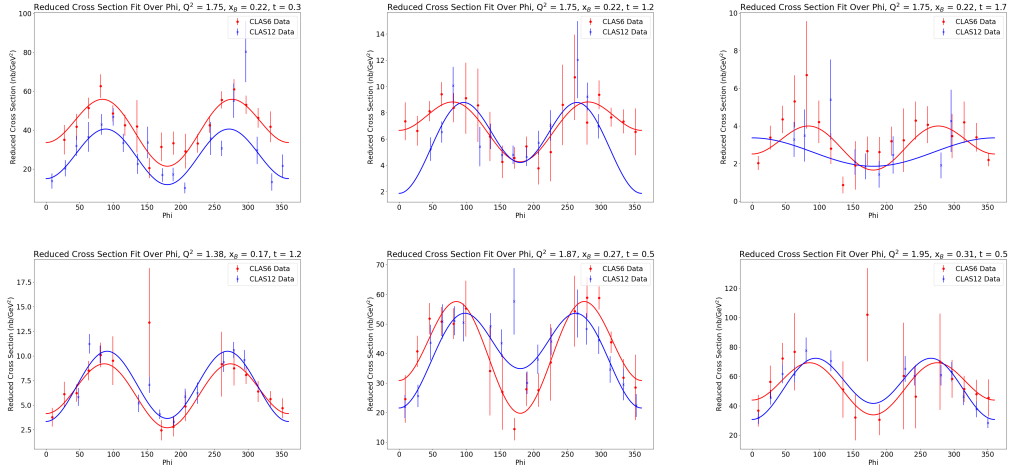


Figure 5-1: Comparison of CLAS12 (blue) and CLAS6 (red) reduced cross sections, using Fall 2018 outbending dataset. Error bars are statistical only.

$$\frac{d^4\sigma_{\gamma^* p \rightarrow p' \pi^0}}{dQ^2 dx_B dt d\phi_\pi} = \Gamma(Q^2, x_B, E) \frac{1}{2\pi} \left( \left( \frac{d\sigma_T}{dt} + \epsilon \frac{d\sigma_L}{dt} \right) + \epsilon \cos(2\phi) \frac{d\sigma_{TT}}{dt} + \sqrt{2\epsilon(1+\epsilon)} \cos(\phi) \frac{d\sigma_{LT}}{dt} \right) \quad (5.4)$$

Where  $\Gamma(Q^2, x_B, E)$  is the virtual photon flux, give in equation 5.5

$$\Gamma(Q^2, x_B, E) = \frac{\alpha}{8\pi} \frac{Q^2}{m_p^2 E^2} \frac{1-x_B}{x_B^3} \frac{1}{1-\epsilon} \quad (5.5)$$

The reduced cross section terms then are just functions of the structure functions and epsilon. At these kinematics, epsilon is approximately 0.5 for the CLAS6 data and 0.9 for the CLAS12 datasets, but given that the  $(\frac{d\sigma_T}{dt} + \epsilon \frac{d\sigma_L}{dt})$  dominates the cross section, these differences are minor. Therefore, close (but not exact) agreement between the two datasets for given kinematic bins are expected for the reduced cross sections. More quantitative statements will be made in coming months, but not at this point.

## 5.2 Structure Function Extraction

## 5.3 Rosenbluth Separation Between Beam Energies

## 5.4 Cross Section with CLAS6 Normalization

## 5.5 Comparison to Theoretical Model

We compare the preliminary cross section to the model developed by S.V. Goloskokov and P. Kroll [Goloskokov and Kroll, 2010](#). This model uses the handbag model to produce theoretical curves for specified sets of kinematic points. This model was implemented in the PARTONS framework [Berthou et al., 2018](#) and was also used in the published CLAS6 result to compare with their experimental cross section, reproduced below in figure [5.5 Bedlinskiy et al., 2014](#)

As discussed, the cross section for this process can be expressed in terms of structure functions as

$$\frac{d^4\sigma_{ep \rightarrow ep'\pi^0}}{dQ^2 dx_B dt d\phi_\pi} = \Gamma(Q^2, x_B, E) \frac{1}{2\pi} \left\{ \left( \frac{d\sigma_T}{dt} + \epsilon \frac{d\sigma_L}{dt} \right) + \epsilon \cos(2\phi) \frac{d\sigma_{TT}}{dt} + \sqrt{2\epsilon(1+\epsilon)} \cos(\phi) \frac{d\sigma_{LT}}{dt} \right\} \quad (1.21)$$

### Notes on GK model from Kemal:

Thank you very much for your response. I include two short responses, below, as well as a third response/question that I hope you can read and respond to:

- Thank you for the reference about the Mandelstam function. I was afterwards able to also find reference to it here, where it was named Kallen Function. I haven't heard of either names before. Thanks! [Källén Function on Wikipedia](#)
- Yes, I am using the code for  $\pi^0$ , so I do not believe any changes need to be made. I am just working from the single C++ file, since it is easier than getting set up with a full partons framework which looked like it had some overhead to setup and install.

**Important question:** I now understand that you took the most updated parameters from P Kroll that would best describe the JLab kinematics from the 2020 paper, and that these are different from the parameters available in 2013. My question to you is - are the parameters that are currently implemented in the GK model the best parameters for me to use (for calculating  $\pi^0$  cross section at JLab CLAS12 10.6 GeV experiment)? Do you take into account any other experiments (such as work in hall A or C) for finding the parameters? To say it differently, how are optimal parameters chosen for this model?

I would refrain myself speaking on behalf of the authors on that question. They might give you better insights into their model. But I can tell you my viewpoint. I think the GPDs should not be optimized for your data. What I mean is the following: since GPDs are universal functions, ideally there should not be multiple parameters for different experiments (so that we have the flexibility to choose among different parameter sets). Rather, the more data we get, the better parameters need to be determined and those parameters need to be unique for all experiments. In this regard, I would just use the latest parameters that the authors offer (assuming that they did a global analysis to tune those parameters). You could alternatively try to change the parameters to fit them to your data and suggest how your data will

impact the extraction of the parameters.

I hope it makes sense, otherwise, we could discuss it further.

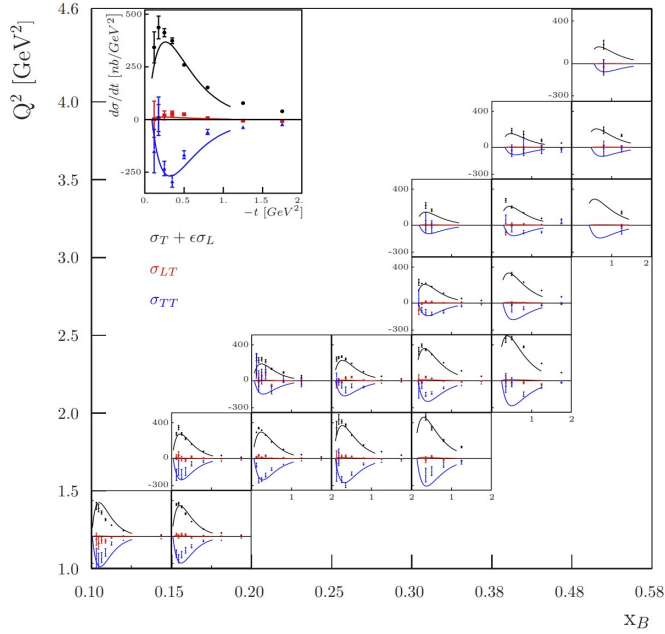
Sorry for the late reply. During the last few weeks, I had some other tasks to complete. I'll be happy to share my thoughts with you.

1. I think the difference is just the different parameters used in separate works.

The parameters of GPDs and their t-slope are not completely the same. At the time I wrote the code, I took the most updated parameters from P. Kroll (or parameters that he thought would best describe the JLab kinematics in Fig. 3 of [this paper](#)). So, I would not expect the same curves just because the GPDs in those works have different parameters.

2. The function  $\Lambda$  is called the Mandelstam variable and somehow I could not find the generic expression online. But, I expressed the definition in my thesis (see Eq. 4.50 on page 129); [this link](#) therein (Chapter 4) you can also see a more detailed implementation of the model. The value of 0.3894 comes from the conversion from  $\text{GeV}^{-2}$  to mb.
3. Yes, the final code works for both  $\pi^+$  and  $\pi^0$  (I am not sure which one you use; if you use the one that you shared above, then it would work only for  $\pi^0$ .  $\pi^+$  implementation can be found in the PARTONS v3. or I have the code for  $\pi^+$  similar to the  $\pi^0$  that you shared above). Their formulation is quite similar albeit with important differences. First of all, the  $\pi^0$  production does not include the so-called pion-pole contribution (see Eq. 4.39 - 4.42 in my thesis). Moreover, their handbag contributions are slightly different. Their differences at the handbag level are discussed in Eq. 4.37 and 4.38 in my thesis.

Just let me know if you need any further clarification; I'll be happy to address it.



To validate the model, we ran the implementation to generate curves and compared to the published CLAS6 result. We observed that the sigma T and sigma L terms were comparable, but not exactly the same, as the 2014 published results, while the sigma TT term was significantly different. It is believed that these differences are due to improvements in the model made in the past 8 years. Figure 5.5 shows one example bin of this comparison, where the color of the curves is matched to the corresponding color of the structure functions.

The parameters for the GK model were taken from

*Their formulation is quite similar albeit with important differences. First of all, the pion 0 production does not include a pole contribution (see Eq. 4.39–4.42 in my thesis). Moreover, their handbag contributions are slightly different.*

The parameters of GPDs and their t-slope are not completely the same. At the time I wrote the code, I took the most updated parameters from P. Kroll (or parameters that he thought would best describe the JLab kinematics in Fig. 3 of S.).

[Diehl et al., 2020](#)). So, I would not expect the same curves just because the GPDs in those works have different parameters.

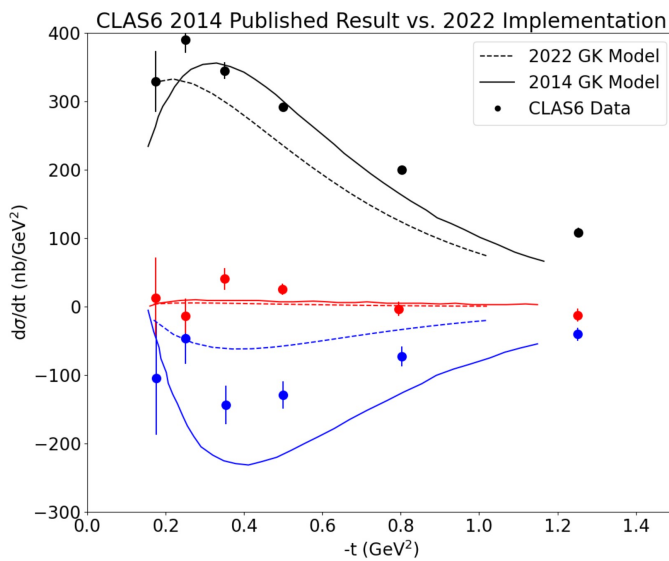
Lambda is defined as:

Description of GK by Kemal Thesis:

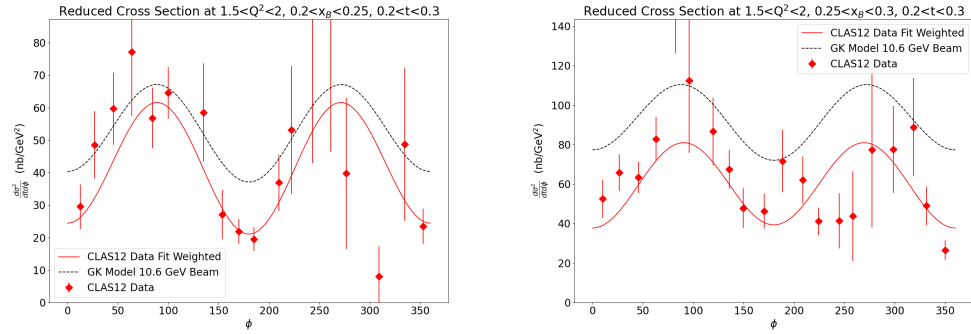
The Goloskokov-Kroll model has been phenomenologically successful (inlcude links showing this). The description is based on QCD factorization theorems. In factorizable processes, the amplitudes can be written as a convolution of a hard scattering which is computable in pQCD, and a soft non perturbative part parameterized by GPDs. Chiral-even GPDs are accessible through DVCS where factorization was proven (CITE). Chiral-odd GPDs can be accessed at subleading twist through Deeply Virtual Meson Production if one assumes an effective handbag mechanism, as desctried by the GK model. QCD factorization theorem for DVMP process has only been proven for longitudinally polarized photons, and also that the cross section is suppressed by a power of  $1/Q$  for transversley polarized photons. The GK model computes contributions from transversely polarized photons in the handbag mechanism as a twist-3 effect in which teh soft part of the process is parameterized in terms of Chiral Odd GPDs. Several GK model parameters implemented in teh PARTONS framework differ from teh parameters used in refrences. The GK model parameters implemented are used in two different publicatoins The GK model, under the assumption of flavor-symmetric sea GPDs, only valence quark GPDs Htilda Etilda Ht and Etildat are needed to describe teh process in the kinematical region of large  $Q^2$  but small zai and t. GPDs in teh GK model are constructed from double distribtuions as follows, which can be integrated analytically, and the GPDs can be expressed in teh following form:

From Easy as Pi: Among the many important consequences is the fact that differently from both inclusive and semi-inclusive processes, GPDs can in principle

provide essential information for determining the missing component to the nucleon longitudinal spin sum rule, which is identified with orbital angular momentum. A complete description of nucleon structure



Finally, we compare the preliminary CLAS12 reduced cross section to the predictions from the GK model. Sample plots are shown below. Agreement is close but not exact. The functional form is as expected. It is unclear if the offset between the CLAS12 fit and the GK model is due to a model discrepancy, or an absolute normalization uncertainty in the CLAS12 calculation. More quantitative statements will be made when uncertainties and correction factors in the CLAS12 work are better understood.



## 5.6 T Dependence and Impact Parameter Extraction

We can calculate the  $t$  dependence of the differential cross section  $d\sigma_U/dt$  by integrating the reduced cross sections over  $\phi$  as in equation 5.6

$$\frac{d\sigma_U}{dt} = \int \frac{d^2\sigma}{dt d\phi} d\phi \quad (5.6)$$

In order to account for regions where the detectors used in CLAS6 and CLAS12 have zero acceptance, it is necessary to include a correction factor  $\eta'$ , defined in equation 5.7 and calculated using Monte Carlo.

$$\eta' = \frac{\int_{\Omega^*} \frac{d^2\sigma}{dt d\phi}}{\int_{\Omega} \frac{d^2\sigma}{dt d\phi}} \quad (5.7)$$

However, at this point this correction factor has not yet been calculated. Instead, we can focus on kinematic bins where the coverage in  $\phi$  is nearly 100%, such that  $\eta'$  would be small. In figure 5-2 we show the  $t$  dependent cross section, calculated only for bins where the coverage in  $\phi$  was greater than 90%, thus the error from not including the  $\eta'$  correction factor is only approximately 10%. We observe a good

agreement in the b slope parameter, which describes the width of the transverse momentum distribution of the proton, between CLAS12 and the published CLAS6 data.

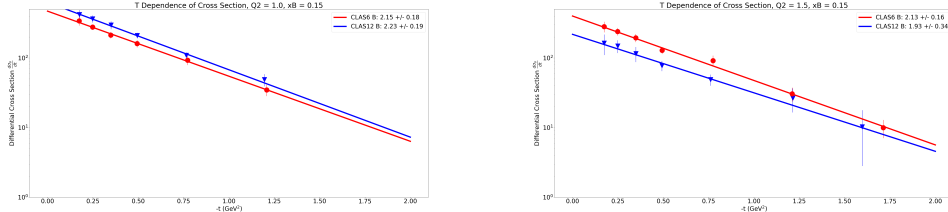


Figure 5-2: CLAS12 and CLAS6 t dependence of cross sections. The fits are exponential functions  $Ae^{-bt}$ , where the slope parameter b are in close agreement for the bins considered. The overall normalization A is not yet determined for the CLAS12 dataset, so a small overall offset from the CLAS6 data is expected. Errors are only statistical.

## 5.7 Conclusion

"Continuous studies based on the current and future measurements will make possible new insights into the QCD structure of hadronic matter."

Pass1 data suffer from CD mis-alignment and other issues solved in the new cooking

Goldstein's straightforward results are elucidated in their 2012 work [Gary R Goldstein, J Osvaldo Gonzalez Hernandez, and Liuti, 2012.](#)

McAllister provides a comprehensive study on elastic particles in his 1956 publication [McAllister and Hofstadter, 1956.](#)

A flexible observables approach by Goldstein was explained in their 2011 research [Gary R. Goldstein, J. Osvaldo Gonzalez Hernandez, and Liuti, 2011.](#)

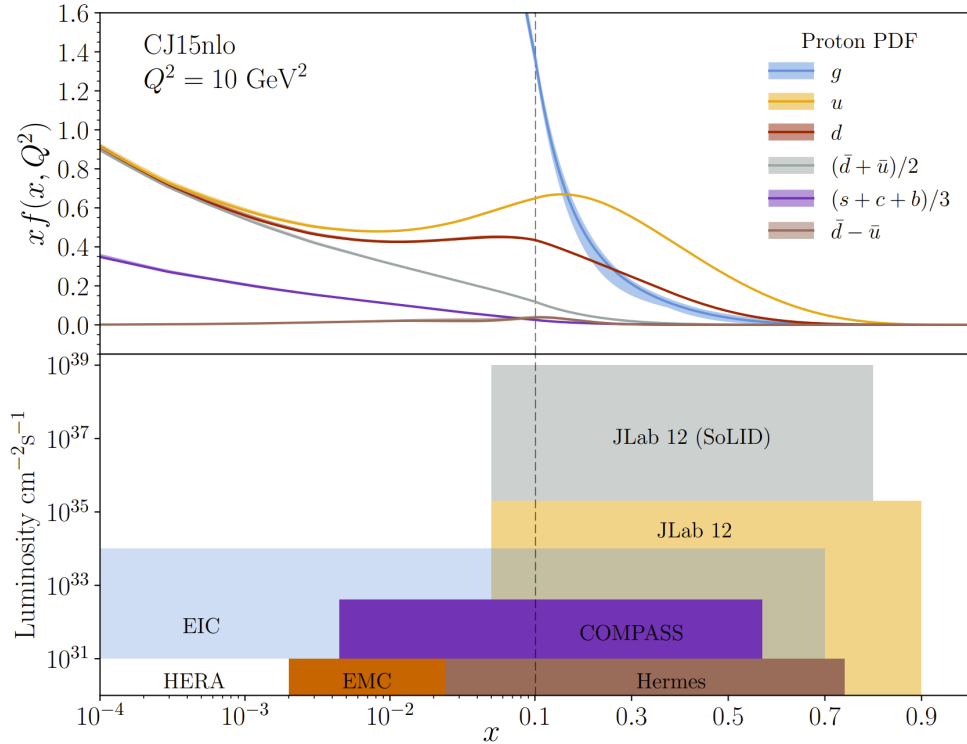


Figure 5-3: Kinematic regions of Deep Inelastic Scattering and the comparative reach of EIC and CEBAF, from ([Arrington et al., 2022](#))

Brodsky addresses light-cone scattering in a 2001 paper [Brodsky, Markus Diehl, and Hwang, 2001](#).

Abt presents their measurement at HERA in a 1993 study [Abt et al., 1993](#).

Derrick's 1995 work discusses measurement data in detail [Derrick et al., 1995](#).

Diehl's 2005 paper provides an in-depth look at protons [M. Diehl and Sapeta, 2005](#).

Patrignani's 2018 paper provides a review of physics [Patrignani and et al. \(Particle Data Group\), 2018](#).

Qiu's 2023 work discusses single distributions [Qiu and Yu, 2023](#).

Zhu's 2015 work explores aspects of microscopy [Zhu and Dürr, 2015](#).

Gockeler's 2007 paper explores transverse simulations [Göckeler et al., 2007](#).



# Bibliography

- [1] I. Abt et al. “Measurement of the proton structure function F2 (x, Q2) in the low-x region at HERA”. In: *Nuclear Physics B* 407.3 (Oct. 1993), pp. 515–535. ISSN: 05503213. DOI: [10.1016/0550-3213\(93\)90090-C](https://doi.org/10.1016/0550-3213(93)90090-C) (cit. on p. 97).
- [2] Patrick Achenbach. *Hall B Status Report*. Tech. rep. 2022. URL: <https://indico.jlab.org/event/597/contributions/10771/attachments/8563/12335/Achenbach-CLAS-Collab-2022.pptx> (cit. on p. 50).
- [3] A. Acker et al. “The CLAS12 Micromegas Vertex Tracker”. In: *Nuclear Instruments and Methods in Physics Research Section A: Accelerators, Spectrometers, Detectors and Associated Equipment* 957 (Mar. 2020), p. 163423. ISSN: 01689002. DOI: [10.1016/j.nima.2020.163423](https://doi.org/10.1016/j.nima.2020.163423). URL: <https://www.sciencedirect.com/science/article/abs/pii/S0168900220300280> (cit. on pp. 53, 55).
- [4] M.G. Alexeev et al. “Measurement of the cross section for hard exclusive  $\pi^0$  muoproduction on the proton”. In: *Physics Letters B* 805 (June 2020), p. 135454. ISSN: 03702693. DOI: [10.1016/j.physletb.2020.135454](https://doi.org/10.1016/j.physletb.2020.135454). URL: <https://www.sciencedirect.com/science/article/abs/pii/S0370269320302586/pdf> (cit. on pp. 40, 41).

- [5] G. Altarelli and G. Parisi. “Asymptotic freedom in parton language”. In: *Nuclear Physics B* 126.2 (Aug. 1977), pp. 298–318. ISSN: 05503213. DOI: [10.1016/0550-3213\(77\)90384-4](https://doi.org/10.1016/0550-3213(77)90384-4). URL: <https://www.sciencedirect.com/science/article/pii/0550321377903844> (cit. on p. 28).
- [6] E. Amaldi, S. Fubini, and G. Furlan. *Pion-electroproduction*. Vol. 83. Berlin, Heidelberg: Springer Berlin Heidelberg, 1979, pp. 1–10. ISBN: 978-3-540-08998-8. DOI: [10.1007/BFb0048208](https://doi.org/10.1007/BFb0048208) (cit. on p. 37).
- [7] M. Amarian et al. “The CLAS forward electromagnetic calorimeter”. In: *Nuclear Instruments and Methods in Physics Research Section A: Accelerators, Spectrometers, Detectors and Associated Equipment* 460.2-3 (Mar. 2001), pp. 239–265. ISSN: 01689002. DOI: [10.1016/S0168-9002\(00\)00996-7](https://doi.org/10.1016/S0168-9002(00)00996-7). URL: <https://www.sciencedirect.com/science/article/abs/pii/S0168900200009967> (cit. on p. 52).
- [8] M.A. Antonioli et al. “The CLAS12 Silicon Vertex Tracker”. In: *Nuclear Instruments and Methods in Physics Research Section A: Accelerators, Spectrometers, Detectors and Associated Equipment* 962 (May 2020), p. 163701. ISSN: 01689002. DOI: [10.1016/j.nima.2020.163701](https://doi.org/10.1016/j.nima.2020.163701). URL: <https://www.sciencedirect.com/science/article/abs/pii/S0168900220302588> (cit. on p. 53).
- [9] J. Arrington et al. “Physics with CEBAF at 12 GeV and future opportunities”. In: *Progress in Particle and Nuclear Physics* 127 (Nov. 2022), p. 103985. ISSN: 01466410. DOI: [10.1016/j.ppnp.2022.103985](https://doi.org/10.1016/j.ppnp.2022.103985). URL: <https://www.sciencedirect.com/science/article/abs/pii/S014664102200045X%20https://arxiv.org/pdf/2112.00060.pdf> (cit. on p. 96).

- [10] G. Asryan et al. “The CLAS12 forward electromagnetic calorimeter”. In: *Nuclear Instruments and Methods in Physics Research Section A: Accelerators, Spectrometers, Detectors and Associated Equipment* 959 (Apr. 2020), p. 163425. ISSN: 01689002. DOI: [10.1016/j.nima.2020.163425](https://doi.org/10.1016/j.nima.2020.163425). URL: <https://www.sciencedirect.com/science/article/abs/pii/S0168900220300309> (cit. on p. 52).
- [11] H Avakian et al. *Hard Exclusive Electroproduction of  $\pi^0$  and  $\eta$  with CLAS12*. Tech. rep. 2011. URL: [https://www.jlab.org/exp\\_prog/PACpage/PAC38/proposals/Previously\\_Approved/E12-06-108%20Update.pdf](https://www.jlab.org/exp_prog/PACpage/PAC38/proposals/Previously_Approved/E12-06-108%20Update.pdf) (cit. on p. 55).
- [12] N. Baltzell et al. “The CLAS12 beamline and its performance”. In: *Nuclear Instruments and Methods in Physics Research Section A: Accelerators, Spectrometers, Detectors and Associated Equipment* 959 (Apr. 2020), p. 163421. ISSN: 01689002. DOI: [10.1016/j.nima.2020.163421](https://doi.org/10.1016/j.nima.2020.163421). URL: <https://www.sciencedirect.com/science/article/abs/pii/S0168900220300267?via%3Dihub> (cit. on pp. 49, 50).
- [13] Marco Battaglieri. *Present and future of JLab CLAS12 physics program*. Tech. rep. 2021. URL: <https://indico.bnl.gov/event/9726/contributions/45661/attachments/33781/54355/battaglieri-DIS21-Apr21.pdf> (cit. on pp. 51, 59).
- [14] Christian W. Bauer et al. “Hard scattering factorization from effective field theory”. In: *Physical Review D* 66.1 (July 2002), p. 014017. ISSN: 0556-2821. DOI: [10.1103/PhysRevD.66.014017](https://doi.org/10.1103/PhysRevD.66.014017). URL: <https://arxiv.org/pdf/hep-ph/0202088.pdf> (cit. on p. 34).

- [15] I. Bedlinskiy et al. “Exclusive Neutral Pion electroproduction at W>2 GeV with CLAS”. In: *Physical Review C - Nuclear Physics* 90.2 (2014). ISSN: 1089490X. DOI: [10.1103/PhysRevC.90.025205](https://doi.org/10.1103/PhysRevC.90.025205). URL: <https://journals.aps.org/prc/abstract/10.1103/PhysRevC.90.025205> <https://arxiv.org/pdf/1405.0988.pdf> (cit. on pp. 37, 40, 41, 86, 88).
- [16] S. Benson et al. “High power operation of the JLab IR FEL driver accelerator”. In: *2007 IEEE Particle Accelerator Conference (PAC)*. IEEE, 2007, pp. 79–81. ISBN: 978-1-4244-0916-7. DOI: [10.1109/PAC.2007.4440128](https://doi.org/10.1109/PAC.2007.4440128). URL: <http://accelconf.web.cern.ch/p07/PAPERS/M00AAB03.PDF> (cit. on p. 46).
- [17] B. Berthou et al. “PARTONS: PARtonic Tomography Of Nucleon Software”. In: *The European Physical Journal C* 78.6 (June 2018), p. 478. ISSN: 1434-6044. DOI: [10.1140/epjc/s10052-018-5948-0](https://doi.org/10.1140/epjc/s10052-018-5948-0) (cit. on p. 88).
- [18] J. D. Bjorken and E. A. Paschos. “Inelastic Electron-Proton and gamma-Proton Scattering and the Structure of the Nucleon”. In: *Physical Review* 185.5 (Sept. 1969), pp. 1975–1982. ISSN: 0031-899X. DOI: [10.1103/PhysRev.185.1975](https://doi.org/10.1103/PhysRev.185.1975). URL: <https://journals.aps.org/pr/abstract/10.1103/PhysRev.185.1975> (cit. on p. 27).
- [19] S. Boyarinov et al. “The CLAS12 Data Acquisition System”. In: *Nuclear Instruments and Methods in Physics Research Section A: Accelerators, Spectrometers, Detectors and Associated Equipment* 966 (June 2020), p. 163698. ISSN: 01689002. DOI: [10.1016/j.nima.2020.163698](https://doi.org/10.1016/j.nima.2020.163698). URL: <https://www.sciencedirect.com/science/article/abs/pii/S0168900220302539> (cit. on p. 58).

- [20] The Editors of Encyclopaedia Britannica. *law of multiple proportions*. 2010. URL: <https://www.britannica.com/science/law-of-multiple-proportions> (cit. on p. 15).
- [21] The Editors of Encyclopaedia Britannica. *Thomson atomic model*. 2023. URL: <https://www.britannica.com/science/Thomson-atomic-model> (cit. on p. 16).
- [22] Stanley J. Brodsky, Markus Diehl, and Dae Sung Hwang. “Light-cone wavefunction representation of deeply virtual Compton scattering”. In: *Nuclear Physics B* 596.1-2 (Feb. 2001), pp. 99–124. ISSN: 05503213. DOI: [10.1016/S0550-3213\(00\)00695-7](https://doi.org/10.1016/S0550-3213(00)00695-7). URL: [https://www.sciencedirect.com/science/article/abs/pii/S0550321300006957%20https://arxiv.org/pdf/hep-ph/0009254.pdf](https://www.sciencedirect.com/science/article/abs/pii/S0550321300006957?20https://arxiv.org/pdf/hep-ph/0009254.pdf) (cit. on p. 97).
- [23] Louis de Broglie. “A tentative theory of light quanta”. In: *The London, Edinburgh, and Dublin Philosophical Magazine and Journal of Science* 47.278 (Feb. 1924), pp. 446–458. ISSN: 1941-5982. DOI: [10.1080/14786442408634378](https://doi.org/10.1080/14786442408634378). URL: <https://www.tandfonline.com/doi/full/10.1080/14786442408634378?scroll=top&needAccess=true&role=tab> (cit. on p. 18).
- [24] M. Burkardt and B. Pasquini. “Modelling the nucleon structure”. In: *The European Physical Journal A* 52.6 (June 2016), p. 161. ISSN: 1434-6001. DOI: [10.1140/epja/i2016-16161-7](https://doi.org/10.1140/epja/i2016-16161-7). URL: <https://arxiv.org/pdf/1510.02567.pdf> (cit. on p. 34).
- [25] Matthias Burkardt. “GPDs with  $\zeta$  Not Equal to 0”. In: *ArXiv* (Nov. 2007). URL: <https://arxiv.org/pdf/0711.1881.pdf> (cit. on p. 34).

- [26] V. D. Burkert, L. Elouadrhiri, and F. X. Girod. “The pressure distribution inside the proton”. In: *Nature* 557.7705 (May 2018), pp. 396–399. ISSN: 0028-0836. DOI: [10.1038/s41586-018-0060-z](https://doi.org/10.1038/s41586-018-0060-z). URL: <https://www.nature.com/articles/s41586-018-0060-z> (cit. on p. 36).
- [27] V.D. Burkert et al. “The CLAS12 Spectrometer at Jefferson Laboratory”. In: *Nuclear Instruments and Methods in Physics Research Section A: Accelerators, Spectrometers, Detectors and Associated Equipment* 959 (Apr. 2020), p. 163419. ISSN: 01689002. DOI: [10.1016/j.nima.2020.163419](https://doi.org/10.1016/j.nima.2020.163419). URL: [https://www.jlab.org/div\\_dept/physics\\_division/dsg/publications2/CLAS12%20NIM%20A959%20\(2020\)%20163419.pdf](https://www.jlab.org/div_dept/physics_division/dsg/publications2/CLAS12%20NIM%20A959%20(2020)%20163419.pdf) <http://eprints.gla.ac.uk/210295/1/210295.pdf> (cit. on pp. 52–54).
- [28] C.C.W. Taylor. *The atomists, Leucippus and Democritus: fragments, a text and translation with a commentary*. University of Toronto Press, 1999, pp. 157–158. ISBN: 0-8020-4390-9 (cit. on p. 15).
- [29] D.S. Carman et al. “The CLAS12 Central Time-of-Flight system”. In: *Nuclear Instruments and Methods in Physics Research Section A: Accelerators, Spectrometers, Detectors and Associated Equipment* 960 (Apr. 2020), p. 163626. ISSN: 01689002. DOI: [10.1016/j.nima.2020.163626](https://doi.org/10.1016/j.nima.2020.163626). URL: <https://www.sciencedirect.com/science/article/abs/pii/S0168900220302060> (cit. on p. 52).
- [30] J. Chadwick. “Possible Existence of a Neutron”. In: *Nature* 129.3252 (Feb. 1932), pp. 312–312. ISSN: 0028-0836. DOI: [10.1038/129312a0](https://doi.org/10.1038/129312a0) (cit. on p. 17).
- [31] P. Chatagnon et al. “The CLAS12 Central Neutron Detector”. In: *Nuclear Instruments and Methods in Physics Research Section A: Accelerators, Spectrometers, Detectors and Associated Equipment* 959 (Apr. 2020), p. 163441.

ISSN: 01689002. DOI: [10.1016/j.nima.2020.163441](https://doi.org/10.1016/j.nima.2020.163441). URL: <https://www.sciencedirect.com/science/article/abs/pii/S0168900220300395> (cit. on p. 54).

- [32] Fei Chen, Paul W. Tillberg, and Edward S. Boyden. “Expansion microscopy”. In: *Science* 347.6221 (Jan. 2015), pp. 543–548. ISSN: 0036-8075. DOI: [10.1126/science.1260088](https://doi.org/10.1126/science.1260088). URL: <https://www.science.org/doi/10.1126/science.1260088> (cit. on p. 18).
- [33] John C. Collins and Andreas Freund. “Proof of factorization for deeply virtual Compton scattering in QCD”. In: *Physical Review D* 59.7 (Feb. 1999), p. 074009. ISSN: 0556-2821. DOI: [10.1103/PhysRevD.59.074009](https://doi.org/10.1103/PhysRevD.59.074009). URL: <https://arxiv.org/pdf/hep-ph/9801262.pdf> (cit. on p. 34).
- [34] M. Contalbrigo et al. “The CLAS12 Ring Imaging Cherenkov detector”. In: *Nuclear Instruments and Methods in Physics Research Section A: Accelerators, Spectrometers, Detectors and Associated Equipment* 964 (June 2020), p. 163791. ISSN: 01689002. DOI: [10.1016/j.nima.2020.163791](https://doi.org/10.1016/j.nima.2020.163791). URL: <https://www.sciencedirect.com/science/article/abs/pii/S0168900220303235> (cit. on p. 52).
- [35] David Lawrence. *The GlueX Experiment and the 12GeV Upgrade at Jefferson Lab*. Tech. rep. Newport News: Jefferson Lab, Apr. 2012, pp. 19–20. URL: [https://halldweb.jlab.org/DocDB/0019/001961/002/20120412\\_AVSLawrence.pdf](https://halldweb.jlab.org/DocDB/0019/001961/002/20120412_AVSLawrence.pdf) (cit. on p. 51).
- [36] Department of Energy. *Department of Energy National Laboratories*. 2023. URL: <https://www.energy.gov/national-laboratories> (cit. on p. 45).

- [37] M. Derrick et al. “Measurement of the proton structure function F2 from the 1993 HERA data”. In: *Zeitschrift für Physik C Particles and Fields* 65.3 (Sept. 1995), pp. 379–398. ISSN: 0170-9739. DOI: [10.1007/BF01556128](https://doi.org/10.1007/BF01556128) (cit. on p. 97).
- [38] M. Diehl and S. Sapeta. “On the analysis of lepton scattering on longitudinally or transversely polarized protons”. In: *The European Physical Journal C* 41.4 (June 2005), pp. 515–533. ISSN: 1434-6044. DOI: [10.1140/epjc/s2005-02242-9](https://doi.org/10.1140/epjc/s2005-02242-9). URL: <https://link.springer.com/article/10.1140/epjc/s2005-02242-9%20https://arxiv.org/pdf/hep-ph/0503023.pdf> (cit. on p. 97).
- [39] S. Diehl et al. “Extraction of Beam-Spin Asymmetries from the Hard Exclusive  $\pi^+$  Channel off Protons in a Wide Range of Kinematics”. In: *Physical Review Letters* 125.18 (Oct. 2020), p. 182001. ISSN: 0031-9007. DOI: [10.1103/PhysRevLett.125.182001](https://doi.org/10.1103/PhysRevLett.125.182001). URL: <https://journals.aps.org/prl/abstract/10.1103/PhysRevLett.125.182001%20https://arxiv.org/pdf/2007.15677.pdf> (cit. on p. 91).
- [40] M. Dlamini et al. “Deep Exclusive Electroproduction of  $\pi^+ \pi^-$  at High  $Q^2$  in the Quark Valence Regime”. In: *Physical Review Letters* 127.15 (Oct. 2021), p. 152301. ISSN: 0031-9007. DOI: [10.1103/PhysRevLett.127.152301](https://doi.org/10.1103/PhysRevLett.127.152301). URL: <https://journals.aps.org/prl/pdf/10.1103/PhysRevLett.127.152301> (cit. on pp. 40, 41).
- [41] A. Donnachie and G. Shaw. “Generalized Vector Dominance”. In: *Electromagnetic Interactions of Hadrons*. Boston, MA: Springer US, 1978, pp. 169–194. DOI: [10.1007/978-1-4757-0713-7\\_3](https://doi.org/10.1007/978-1-4757-0713-7_3) (cit. on p. 37).

- [42] T. William Donnelly et al. *Foundations of Nuclear and Particle Physics*. Cambridge University Press, Feb. 2017. ISBN: 9780521765114. DOI: [10.1017/9781139028264](https://doi.org/10.1017/9781139028264) (cit. on p. 25).
- [43] T.W. Donnelly, Sabine Jeschonnek, and J.W. Van Orden. “General tensor structure for electron scattering in terms of invariant responses”. In: *Annals of Physics* 448 (Jan. 2023), p. 169174. ISSN: 00034916. DOI: [10.1016/j.aop.2022.169174](https://doi.org/10.1016/j.aop.2022.169174) (cit. on p. 37).
- [44] D Dreschsel and L Tiator. “Threshold pion photoproduction on nucleons”. In: *Journal of Physics G: Nuclear and Particle Physics* 18.3 (Mar. 1992), pp. 449–497. ISSN: 0954-3899. DOI: [10.1088/0954-3899/18/3/004](https://doi.org/10.1088/0954-3899/18/3/004). URL: <https://iopscience.iop.org/article/10.1088/0954-3899/18/3/004/pdf> (cit. on pp. 37, 64).
- [45] R. Fair et al. “The CLAS12 superconducting magnets”. In: *Nuclear Instruments and Methods in Physics Research Section A: Accelerators, Spectrometers, Detectors and Associated Equipment* 962 (May 2020), p. 163578. ISSN: 01689002. DOI: [10.1016/j.nima.2020.163578](https://doi.org/10.1016/j.nima.2020.163578). URL: <https://www.sciencedirect.com/science/article/abs/pii/S0168900220301522> (cit. on pp. 52, 53).
- [46] Richard P. Feynman. “Very High-Energy Collisions of Hadrons”. In: *Physical Review Letters* 23.24 (Dec. 1969), pp. 1415–1417. ISSN: 0031-9007. DOI: [10.1103/PhysRevLett.23.1415](https://doi.org/10.1103/PhysRevLett.23.1415). URL: <https://journals.aps.org/prl/abstract/10.1103/PhysRevLett.23.1415%20https://authors.library.caltech.edu/3871/1/FEYprl69.pdf> (cit. on p. 27).
- [47] Linda E. Franken et al. “A Technical Introduction to Transmission Electron Microscopy for Soft-Matter: Imaging, Possibilities, Choices, and Technical Developments”. In: *Small* 16.14 (Apr. 2020), p. 1906198. ISSN: 1613-6810. DOI:

- [10.1002/smll.201906198](https://doi.org/10.1002/smll.201906198). URL: <https://onlinelibrary.wiley.com/doi/full/10.1002/smll.201906198> (cit. on p. 18).
- [48] E. Fuchey et al. “Exclusive neutral pion electroproduction in the deeply virtual regime”. In: *Physical Review C* 83.2 (Feb. 2011), p. 025201. ISSN: 0556-2813. DOI: [10.1103/PhysRevC.83.025201](https://doi.org/10.1103/PhysRevC.83.025201). URL: <https://journals.aps.org/prc/abstract/10.1103/PhysRevC.83.025201%20https://arxiv.org/pdf/1003.2938.pdf> (cit. on pp. 40, 41).
- [49] Hans Geiger and Ernest Marsden. “On a Diffuse Reflection of the alpha-Particles”. In: *Proceedings of the Royal Society of London Series A* 82.557 (1909), pp. 495–500 (cit. on p. 17).
- [50] M. Göckeler et al. “Transverse Spin Structure of the Nucleon from Lattice-QCD Simulations”. In: *Physical Review Letters* 98.22 (May 2007), p. 222001. ISSN: 0031-9007. DOI: [10.1103/PhysRevLett.98.222001](https://doi.org/10.1103/PhysRevLett.98.222001). URL: <https://arxiv.org/pdf/hep-lat/0612032.pdf%20https://journals.aps.org/prl/abstract/10.1103/PhysRevLett.98.222001> (cit. on p. 97).
- [51] Gary R Goldstein, J Osvaldo Gonzalez Hernandez, and Simonetta Liuti. “Easy as  $\pi$ 0: on the interpretation of recent electroproduction results”. In: *Journal of Physics G: Nuclear and Particle Physics* 39.11 (Nov. 2012), p. 115001. ISSN: 0954-3899. DOI: [10.1088/0954-3899/39/11/115001](https://doi.org/10.1088/0954-3899/39/11/115001). URL: <https://inspirehep.net/literature/1086573%20https://arxiv.org/pdf/1201.6088.pdf> (cit. on p. 95).
- [52] Gary R. Goldstein, J. Osvaldo Gonzalez Hernandez, and Simonetta Liuti. “Flexible parametrization of generalized parton distributions from deeply virtual Compton scattering observables”. In: *Physical Review D* 84.3 (Aug. 2011), p. 034007. ISSN: 1550-7998. DOI: [10.1103/PhysRevD.84.034007](https://doi.org/10.1103/PhysRevD.84.034007). URL: <https://arxiv.org/pdf/1105.5001.pdf>

//journals.aps.org/prd/abstract/10.1103/PhysRevD.84.034007%  
20https://arxiv.org/pdf/1012.3776.pdf (cit. on p. 95).

- [53] S. V. Goloskokov and P. Kroll. “An attempt to understand exclusive  $\pi$  + electroproduction”. In: *The European Physical Journal C* 65.1-2 (Jan. 2010), p. 137. ISSN: 1434-6044. DOI: 10.1140/epjc/s10052-009-1178-9. URL: <https://link.springer.com/content/pdf/10.1140/epjc/s10052-009-1178-9.pdf> (cit. on p. 88).
- [54] M. Hillery et al. “Distribution functions in physics: Fundamentals”. In: *Physics Reports* 106.3 (Apr. 1984), pp. 121–167. ISSN: 03701573. DOI: 10.1016/0370-1573(84)90160-1. URL: <http://ursula.chem.yale.edu/~batista/classes/v572/Scully.pdf> (cit. on p. 32).
- [55] Tomáš Husek, Evgueni Goudzovski, and Karol Kampf. “Precise Determination of the Branching Ratio of the Neutral-Pion Dalitz Decay”. In: *Physical Review Letters* 122.2 (Jan. 2019), p. 022003. ISSN: 0031-9007. DOI: 10.1103/PhysRevLett.122.022003. URL: <https://arxiv.org/pdf/1809.01153.pdf> (cit. on p. 43).
- [56] Jaume Navarro. *A History of the Electron: J.J. and G.P. Thomson*. Cambridge University Press, 1995. ISBN: 978-1-107-00522-8. (Cit. on p. 16).
- [57] Jefferson Lab. *About Jefferson Lab*. 2023. URL: <https://www.jlab.org/about> (cit. on p. 46).
- [58] Xiangdong Ji. “Gauge-Invariant Decomposition of Nucleon Spin”. In: *Physical Review Letters* 78.4 (Jan. 1997), pp. 610–613. ISSN: 0031-9007. DOI: 10.1103/PhysRevLett.78.610. URL: <https://journals.aps.org/prl/abstract/10.1103/PhysRevLett.78.610>.

- [1103/PhysRevLett.78.610%20https://arxiv.org/pdf/hep-ph/9603249.pdf](https://arxiv.org/pdf/hep-ph/9603249.pdf) (cit. on p. 34).
- [59] Xiangdong Ji. “GENERALIZED PARTON DISTRIBUTIONS”. In: *Annual Review of Nuclear and Particle Science* 54.1 (Dec. 2004), pp. 413–450. ISSN: 0163-8998. DOI: [10.1146/annurev.nucl.54.070103.181302](https://doi.org/10.1146/annurev.nucl.54.070103.181302). URL: <https://www.annualreviews.org/doi/10.1146/annurev.nucl.54.070103.181302> (cit. on pp. 32, 33).
- [60] Kyungseon Joo. *Electron Beam Polarization Measurements Using the Hall B Moller Polarimeter*. Tech. rep. Newport News: Jefferson Lab, Mar. 2002. URL: <https://casa.jlab.org/internal/publications/technotes/tn02009.pdf> (cit. on p. 50).
- [61] Max Klein. *Resolving the Inner Structure of Matter The H1 Experiment at HERA*. Tech. rep. Workshop at Podgorica - 25 years of the Science Faculty, 2005 (cit. on p. 30).
- [62] Valery Kubarovsky. “Deeply Virtual Exclusive Reactions with CLAS”. In: *Nuclear Physics B - Proceedings Supplements* 219-220 (Oct. 2011), pp. 118–125. ISSN: 09205632. DOI: [10.1016/j.nuclphysbps.2011.10.080](https://doi.org/10.1016/j.nuclphysbps.2011.10.080). URL: <https://www.sciencedirect.com/science/article/pii/S0920563211008218/pdf?md5=2efd6bc3a69acdce62fc3d0bfa1be5c5&pid=1-s2.0-S0920563211008218-main.pdf> (cit. on p. 35).
- [63] Sangbaek Lee. *Measurement of the Deeply Virtual Compton Scattering Cross Section from the Proton at 10.6 GeV using the CLAS12 Detector*. Tech. rep. 2022. URL: <https://dspace.mit.edu/handle/1721.1/150759> (cit. on pp. 36, 59).

- [64] Xuezhi Ma et al. “6 nm super-resolution optical transmission and scattering spectroscopic imaging of carbon nanotubes using a nanometer-scale white light source”. In: *Nature Communications* 12.1 (Nov. 2021), p. 6868. ISSN: 2041-1723. DOI: [10.1038/s41467-021-27216-5](https://doi.org/10.1038/s41467-021-27216-5) (cit. on p. 18).
- [65] R. W. McAllister and R. Hofstadter. “Elastic Scattering of 188-MeV Electrons from the Proton and the Alpha Particle”. In: *Physical Review* 102 (Mar. 1956), pp. 851–856 (cit. on p. 95).
- [66] B.A. Mecking et al. “The CEBAF large acceptance spectrometer (CLAS)”. In: *Nuclear Instruments and Methods in Physics Research Section A: Accelerators, Spectrometers, Detectors and Associated Equipment* 503.3 (May 2003), pp. 513–553. ISSN: 01689002. DOI: [10.1016/S0168-9002\(03\)01001-5](https://doi.org/10.1016/S0168-9002(03)01001-5). URL: <https://www.sciencedirect.com/science/article/abs/pii/S0168900203010015> (cit. on pp. 49, 51).
- [67] M.D. Mestayer et al. “The CLAS12 drift chamber system”. In: *Nuclear Instruments and Methods in Physics Research Section A: Accelerators, Spectrometers, Detectors and Associated Equipment* 959 (Apr. 2020), p. 163518. ISSN: 01689002. DOI: [10.1016/j.nima.2020.163518](https://doi.org/10.1016/j.nima.2020.163518). URL: <https://www.sciencedirect.com/science/article/abs/pii/S016890022030111X> (cit. on p. 52).
- [68] OSG. *OSG*. 2006. URL: <https://doi.org/10.21231/906P-4D78> (cit. on p. 63).
- [69] C. Patrignani and et al. (Particle Data Group). *Review of Particle Physics*. Tech. rep. lawrence berkeley national laboratory, 2018, pp. 441–455. DOI: [10.1088/1674-1137/40/10/100001](https://doi.org/10.1088/1674-1137/40/10/100001). URL: <https://pdg.lbl.gov/> (cit. on p. 97).

- [70] Ruth Pordes et al. “The open science grid”. In: *Journal of Physics: Conference Series* 78 (July 2007), p. 012057. ISSN: 1742-6588. DOI: [10.1088/1742-6596/78/1/012057](https://doi.org/10.1088/1742-6596/78/1/012057) (cit. on p. 63).
- [71] Jian-Wei Qiu and Zhite Yu. “Single diffractive hard exclusive processes for the study of generalized parton distributions”. In: *Physical Review D* 107.1 (Jan. 2023), p. 014007. ISSN: 2470-0010. DOI: [10.1103/PhysRevD.107.014007](https://doi.org/10.1103/PhysRevD.107.014007). URL: <https://journals.aps.org/prd/pdf/10.1103/PhysRevD.107.014007%20https://arxiv.org/pdf/2210.07995.pdf> (cit. on p. 97).
- [72] B. Raydo et al. “The CLAS12 Trigger System”. In: *Nuclear Instruments and Methods in Physics Research Section A: Accelerators, Spectrometers, Detectors and Associated Equipment* 960 (Apr. 2020), p. 163529. ISSN: 01689002. DOI: [10.1016/j.nima.2020.163529](https://doi.org/10.1016/j.nima.2020.163529). URL: <https://www.sciencedirect.com/science/article/abs/pii/S0168900220301182> (cit. on p. 56).
- [73] Ernest Rutherford. “Collision of alpha Particles with Light Atoms. IV. An Anomalous Effect in Nitrogen”. In: *Philosophical Magazine Series 6* 37 (1919), pp. 581–587. URL: [https://www.tandfonline.com/doi/abs/10.1080/14786431003659230](https://doi.org/10.1080/14786431003659230) (cit. on p. 17).
- [74] Ernest Rutherford. “The Scattering of Alpha and Beta Particles by Matter and the Structure of the Atom”. In: *Philosophical Magazine Series 6* 21 (1911), pp. 669–688 (cit. on p. 17).
- [75] E.P. Segarra et al. “The CLAS12 Backward Angle Neutron Detector (BAND)”. In: *Nuclear Instruments and Methods in Physics Research Section A: Accelerators, Spectrometers, Detectors and Associated Equipment* 978 (Oct. 2020), p. 164356. ISSN: 01689002. DOI: [10.1016/j.nima.2020.164356](https://doi.org/10.1016/j.nima.2020.164356). URL: <https://www.sciencedirect.com/science/article/abs/pii/S0168900220301182>

//www.sciencedirect.com/science/article/abs/pii/S0168900220307531

(cit. on p. 54).

- [76] Igor Sfiligoi et al. “The Pilot Way to Grid Resources Using glideinWMS”. In: *2009 WRI World Congress on Computer Science and Information Engineering*. IEEE, 2009, pp. 428–432. ISBN: 978-0-7695-3507-4. DOI: [10.1109/CSIE.2009.950](https://doi.org/10.1109/CSIE.2009.950) (cit. on p. 63).
- [77] P. E. Shanahan and W. Detmold. “Pressure Distribution and Shear Forces inside the Proton”. In: *Physical Review Letters* 122.7 (Feb. 2019), p. 072003. ISSN: 0031-9007. DOI: [10.1103/PhysRevLett.122.072003](https://doi.org/10.1103/PhysRevLett.122.072003). URL: <https://journals.aps.org/prl/abstract/10.1103/PhysRevLett.122.072003> (cit. on p. 36).
- [78] Y.G. Sharabian et al. “The CLAS12 high threshold Cherenkov counter”. In: *Nuclear Instruments and Methods in Physics Research Section A: Accelerators, Spectrometers, Detectors and Associated Equipment* 968 (July 2020), p. 163824. ISSN: 01689002. DOI: [10.1016/j.nima.2020.163824](https://doi.org/10.1016/j.nima.2020.163824). URL: <https://www.sciencedirect.com/science/article/abs/pii/S0168900220303466> (cit. on p. 52).
- [79] Thomas McEvilley. *THe Shape of Ancient Thought: Comparative Studies in Greek and Indian Philosophies*. New York: Allworth Press, 2002. ISBN: 978-0-8020-4390-0 (cit. on p. 15).
- [80] J.J. Thomson. “On Bodies Smaller than Atoms”. In: *The Poular Science Monthly* (1901), pp. 323–325. URL: <https://books.google.com/books?id=3CMDAAAAMBAJ&pg=PA323#v=onepage&q&f=false> (cit. on p. 15).

- [81] Mark Thomson. *Modern Particle Physics*. Cambridge University Press, Sept. 2013, pp. 160–204. ISBN: 9781107034266. DOI: [10.1017/CBO9781139525367](https://doi.org/10.1017/CBO9781139525367) (cit. on pp. 23, 27).
- [82] M. Ungaro et al. “The CLAS12 Low Threshold Cherenkov detector”. In: *Nuclear Instruments and Methods in Physics Research Section A: Accelerators, Spectrometers, Detectors and Associated Equipment* 957 (Mar. 2020), p. 163420. ISSN: 01689002. DOI: [10.1016/j.nima.2020.163420](https://doi.org/10.1016/j.nima.2020.163420). URL: <https://inspirehep.net/literature/1777565> (cit. on p. 52).
- [83] Yan Wang. *CEBAF Overview*. Tech. rep. Newport News: Jefferson Lab, June 2010. URL: <https://www.jlab.org/hugs/archive/Schedule2010/slides/Wang.pdf> (cit. on pp. 46–48).
- [84] E. Wigner. “On the Quantum Correction For Thermodynamic Equilibrium”. In: *Physical Review* 40.5 (June 1932), pp. 749–759. ISSN: 0031-899X. DOI: [10.1103/PhysRev.40.749](https://doi.org/10.1103/PhysRev.40.749). URL: [https://lab409.chem.ccu.edu.tw/~yach932/CH3\\_Reference/51.PhysRev.40.749.pdf](https://lab409.chem.ccu.edu.tw/~yach932/CH3_Reference/51.PhysRev.40.749.pdf) (cit. on p. 31).
- [85] David B. Williams and C. Barry Carter. *Transmission Electron Microscopy*. Boston, MA: Springer US, 2009. ISBN: 978-0-387-76500-6. DOI: [10.1007/978-0-387-76501-3](https://doi.org/10.1007/978-0-387-76501-3). URL: <https://link.springer.com/book/10.1007/978-0-387-76501-3> (cit. on pp. 18, 20).
- [86] Elliott Wolin et al. “EVIO &#x2014; A lightweight object-oriented I/O package”. In: *2007 IEEE Nuclear Science Symposium Conference Record*. IEEE, Oct. 2007, pp. 856–859. ISBN: 978-1-4244-0922-8. DOI: [10.1109/NSSMIC.2007.4436463](https://doi.org/10.1109/NSSMIC.2007.4436463). URL: <https://ieeexplore.ieee.org/abstract/document/4436463> (cit. on p. 56).

- [87] Yimei Zhu and Hermann Dürr. “The future of electron microscopy”. In: *Physics Today* 68.4 (Apr. 2015), pp. 32–38. ISSN: 0031-9228. DOI: [10.1063/PT.3.2747](https://doi.org/10.1063/PT.3.2747). URL: <https://physicstoday.scitation.org/doi/10.1063/PT.3.2747> (cit. on p. 97).
- [88] P A Zyla et al. “Review of Particle Physics”. In: *Progress of Theoretical and Experimental Physics* 2020.8 (Aug. 2020). ISSN: 2050-3911. DOI: [10.1093/ptep/ptaa104](https://doi.org/10.1093/ptep/ptaa104). URL: <https://pdg.lbl.gov/2020/reviews/rpp2020-structure-functions.pdf> (cit. on pp. 28, 29).



# **Appendix A**

## **Full Cross Section Data**

To be completed



# Appendix B

## BSA Cross Check

As an additional cross check, Bobby calculated a  $DV\pi^0P$  beam spin asymmetry and compared to Andrey Kim's results. This check will not comment on any acceptance, luminosity, or virtual photon flux factor calculations, but does validate exclusive event selection criteria. By examining figure B-1 we can see that agreement is reasonable, especially considering Bobby's calculation does not have sideband subtraction included.

Fig B-1 shows an overlay comparison of Andrey Kim's results (black datapoints, red fit line) and Bobby's results (red datapoints, orange fit line)

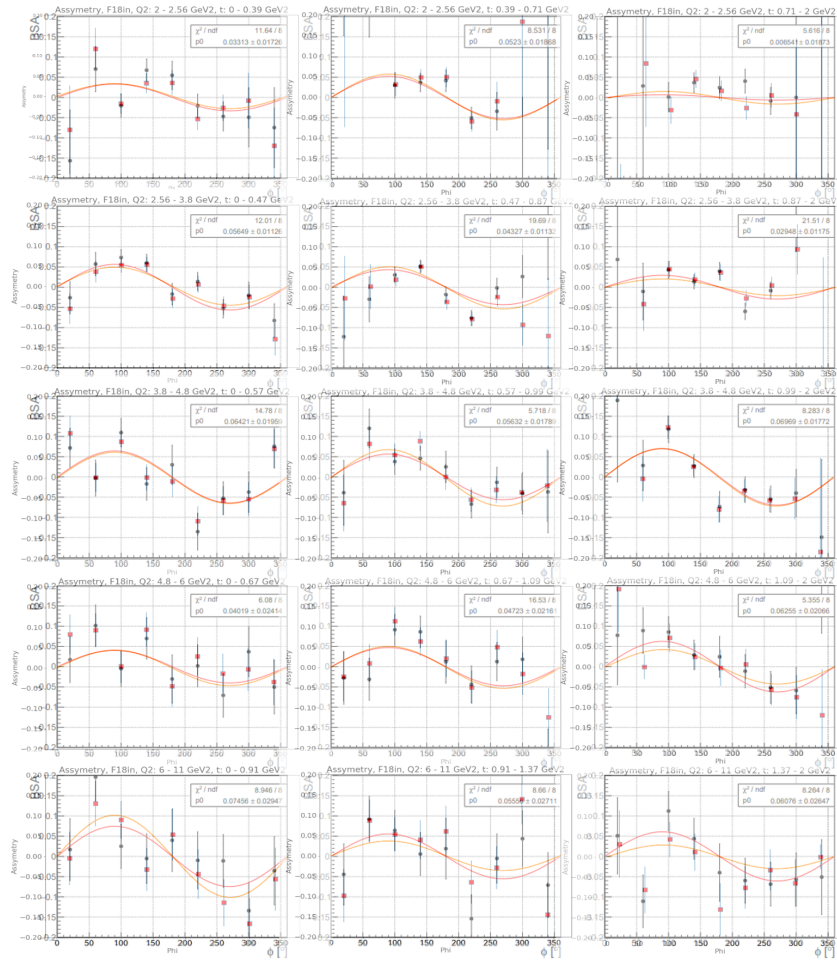


Figure B-1: BSA Cross Check Results

## Appendix C

### Derivation of phi math convention

Thus:  $\phi = \arccos( (\mathbf{v3l} \cdot \mathbf{v3h}) / (\text{mag } \mathbf{v3l} \text{ mag } \mathbf{v3h}) )$

$$\phi = \cos^{-1} \left( \frac{(\mathbf{p}_e \times \mathbf{p}_{e'}) \cdot (\mathbf{p}_{p'} \times \mathbf{p}_{\gamma^*})}{\|\mathbf{p}_e \times \mathbf{p}_{e'}\| \|\mathbf{p}_{p'} \times \mathbf{p}_{\gamma^*}\|} \right)$$

if  $\text{dot}(\mathbf{p}_e \times \mathbf{p}_{e'}, \mathbf{p}_{p'})$  is greater than 0, then do  $360 - \phi = \phi$ . If we expand the above out, we get:  $-\mathbf{p}_{p'} \cdot \mathbf{e}_z \mathbf{e}_y + \mathbf{p}_y \cdot \mathbf{e}_z \mathbf{e}_x$  is greater than zero which we can reduce to  $-\mathbf{p}_{p'} \cdot \mathbf{e}_y + \mathbf{p}_y \cdot \mathbf{e}_x$  is greater than zero [reference](#)

By inspecting table below, we can see what this really amounts to, is the trento convention saying that we take the angle by measuring counterclockwise from the proton vector to the electron vector.

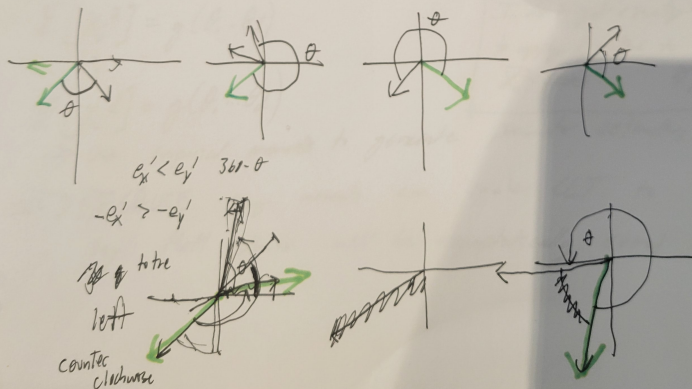
$360^\circ - \theta$  when

$$p_y'e'_x > p_xe'_y$$

$$p_y > p_x$$

$p_y$	$p_x$	(G)	(G)	L	R	$\theta$	$I_r$	$I_r'$
-	-	-	-	+	+		- -	- +
-	-	-	+	-	+	$< 180^\circ$	$> 180^\circ$	+ -
-	-	t	-	+	-			+ +
-	-	+	7	-	-			
-	+	-	-	+	-			
-	+	-	+	-	-			
-	+	+	-	+	+			
-	+	t	t	-	+			

$$-e'_x > -e'_y \quad e'_x < e'_y \quad \# |e'_x| > |e'_y| \text{ shows } m$$



## Appendix D

# Notes on Kinematic Relationships

Derivation of infinite momentum frame Bjorken x. Take quark to have momentum fraction  $\xi$  of proton's total momentum,i.e.  $p_q = \xi p_2$ :

Inf. Mom. frame - neglect proton mass so  $p_2 = E_2$ , neglect all transverse momenta:

Struck quark 4-momenta:  $p_q = \xi p_2 = (\xi E_2, \xi E_2, 0, 0)$

4-momenta of quark after interaction:  $(p_q + q) = (\xi p_2 + q)$

Square the 4-momenta  $(\xi p_2 + q)^2 = \xi^2 p_2^2 + q^2 + 2\xi p_2 \cdot q = m_q^2$

Continue, noting  $p_q = \xi p_2$  :  $m_q^2 = p_q^2 - Q^2 + 2\xi p_2 \cdot q$

Since  $p_q^2 = m_q^2$ , we have:  $m_q^2 = m_q^2 - Q^2 + 2\xi p_2 \cdot q$

So  $0 = -Q^2 + 2\xi p_2 \cdot q \longrightarrow \xi = \frac{Q^2}{2p_2 \cdot q} = x_B$

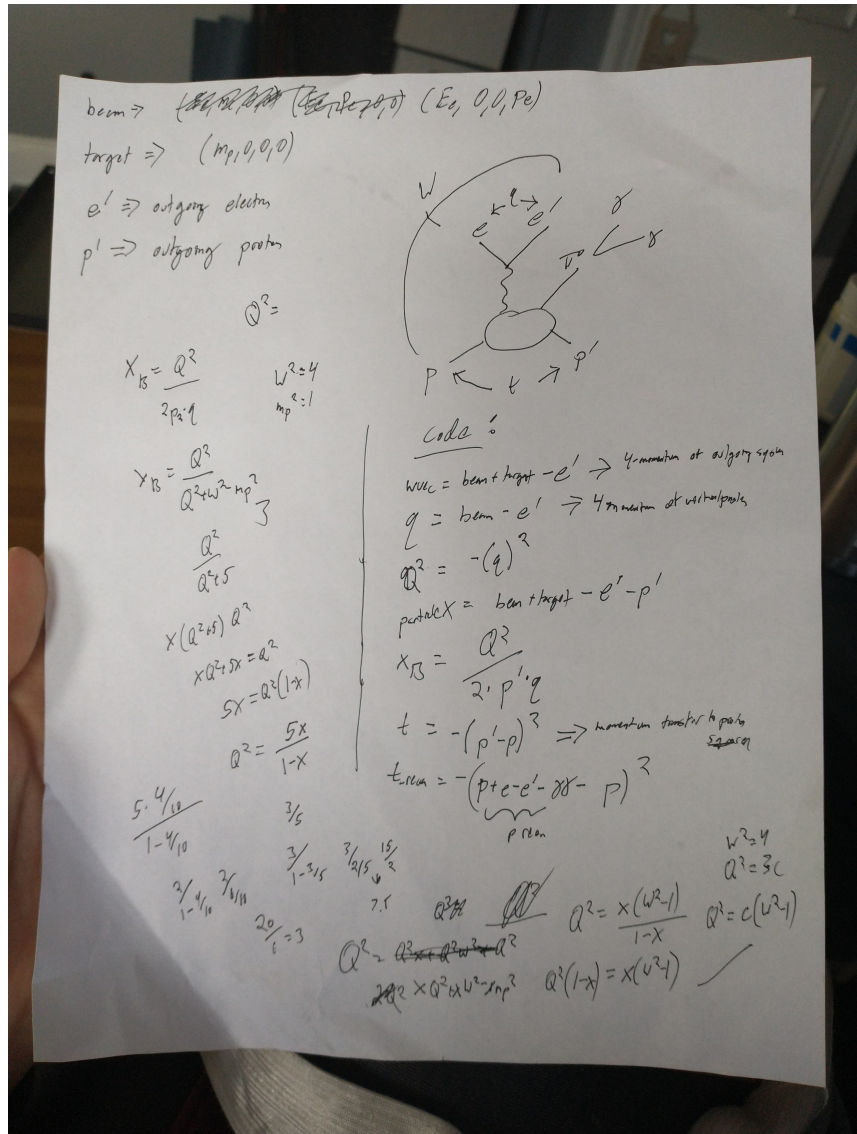


Figure D-1: Caption